Integrate-and-fire modeling of dorsal horn neurons and their functional states in pain pathways

Auteur : De Worm, Anaëlle
Promoteur(s) : Sacré, Pierre
Faculté : Faculté des Sciences appliquées
Diplôme : Master en ingénieur civil biomédical, à finalité spécialisée
Année académique : 2020-2021
URI/URL : http://hdl.handle.net/2268.2/12960

Integrate-and-fire modeling of dorsal horn neurons and their functional states in pain pathways

Master thesis realized with the aim of obtaining the degree of Master in Biomedical Engineering

De Worm Anaëlle

Supervisor:

P. Sacré

Jury members:

G. Drion

C. Phillips

V. Seutin

UNIVERSITY OF LIÈGE

FACULTY OF APPLIED SCIENCE

ACADEMIC YEAR 2020-2021

Abstract

Integrate-and-fire modeling of dorsal horn neurons and their functional states in pain pathways

Pain sensations are adaptive and aim to keep the body safe by triggering appropriate protective responses. However, pain can become maladaptive and create a disease state of the nervous system, associated with chronic pain. This disease state results in an acute and prolonged feeling of pain. To relieve patients suffering from chronic pain, there are two suboptimal treatments, both effective in less than 50% of cases: the prescription of opioids, at the risk of misuse or abuse that could cause overdosed-related deaths, or spinal cord stimulation, a new promising treatment strategy. Both of them are suboptimal due to the lack of knowledge about the mechanisms behind pain generation. A better understanding of these mechanisms would help to develop more efficient treatment strategies.

This thesis focuses on the modeling of the behavior of Dorsal Horn Neurons (DHNs), which are neurons in the spinal cord embedded in the network taking care of pain signal transmission to the brain. This group of neurons shows 4 types of firing patterns: tonic firing, accelerating firing, plateau potentials and bursting. Each firing pattern is assumed to correspond to a type of functional state in pain processing. Based on some of the rare attempts to model them, we developed an integrate-and-fire model of DHNs. Our objective is to understand the role of each timescale in the DHNs firing patterns generation and the type of feedback involved in the excitability of these neurons, which is either restorative or regenerative.

More specifically, this thesis follows an incremental procedure starting from a 2D integrate-and-fire model with a fast and a slow feedback. The impact of the slow feedback nature (restorative or regenerative) on the phase plane and the time responses is studied. The regenerative slow feedback involves specific properties shown in neurons that have calcium channels such as bistability, spike latency and afterdepolarization potential. The restorative slow feedback allows to always converge back to rest without perturbations. Together, these two feedbacks are able to simulate tonic firing.

Then, we created a 3D model with a fast, a slow regenerative and an ultra-slow restorative feedback. The analysis of this new model revealed that the additional ultra-slow feedback is involved in the generation of bursting. Indeed, the ultra-slow feedback offers a modulation of the total current applied in the equivalent 2D model. This allows the generation of trains of spikes and quiescent periods as the 2D model travels between the stable and the cyclic regimes during a period of oscillations of the 3D model response.

Following the incremental procedure, the final 4D model consists in a fast, a slow regenerative, a super-slow regenerative and an ultra-slow restorative feedbacks. The additional super-slow feedback offers a second direction for the modulation of the total current applied in the 2D equivalent model by shaping the increase in instantaneous frequency during the burst or before converging towards a limit cycle, in the case where the ultra-slow feedback is weak. The 4D model is able to represent all DHNs firing patterns stated provided that the strength of each feedback is well chosen. This result allows to better understand the functional mechanisms behind the change in excitability.

In further works, it would be interesting to verify that conductance-based models follow the mechanisms we highlighted. Also, a model of the pain processing network at the level of the spinal cord may reveal other directions of DHNs excitability modulation on which new designs of pharmacological or neurostimulation treatments could act on.

Acknowledgments

I would like to thank my supervisor, Prof. Pierre Sacré, for his advice, his time and his great support throughout the year. I really enjoyed to work on this interesting project and the discussions we had about it.

Also, I would like to thank my family for their support. In particular, many thanks to my dad who always helped me to put things in perspective and to my mom who supported me as much during these 5 years.

Finally, a special thank to my friends for being there for me. Especially, I would like to thank my boyfriend for his typical good mood and his help during the proofreading.

" Go as far as you can see; when you get there, you'll be able to see further "

<div style="text-align: right;">

———————————————

Thomas Carlyle

</div>

Contents

Chapter 1

Introduction

Pain is an adaptive sensation that usually aims to protect the body from being injured. The signals interpreted as painful by the brain can be modulated by relay neurons in the spinal cord to trigger the appropriate protective responses. In healthy individuals, adaptive pain signals are split into two types: acute pain signals that trigger withdrawal reflexes and prolonged pain signals assisting healing. However, pain signals can become maladaptive. Typically, this third type of pain can trigger hypersensitivity and continuous discomfort. This disease state of the nervous system is associated with chronic pain, a condition that affects approximately 20% of the grown-up population.

Nowadays, no treatment is effective enough to relieve patients suffering from chronic pain. These patients have two possibilities. First, they can be the subjects of pharmacological approaches. Typically, these approaches involve the prescription of opioids. However, they are not perfectly effective on every patient and they can be the cause of death if they are misused or abused. Second, they can be treated by new strategies such as spinal cord stimulation. However, this treatment is sub-optimal and does not relieve all patients treated. For such promising but not efficient enough treatment, there is a real need to understand the mechanisms involved at the level of the spinal cord, where the first relay neurons treat pain signals. With the keys of pain transmission, perfected and efficient treatments could be conceived to cure a larger majority of patients suffering from chronic pain.

In this work, we chose to study the excitability of the relay neurons located in the spinal cord. Indeed, this type of neurons shows different groups of firing patterns that may correspond to different functional states in pain signals processing. To do so, we built an integrate-and-fire model in order to understand the role of the restorative and regenerative feedbacks and their timescale in the generation of these neuron firing patterns. To be able to understand the separate effect of each feedback in the final model, we used an incremental procedure. This approach is based on some works in the rare literature associated with pain modeling that attempted to highlight key ion channels that would be involved in the kinetics of the considered relay neurons.

This report is organized as follows: first, chapter 2 aims to explain the basic concepts this work relies on by describing basic notions of electrophysiology and basic types of models used to capture a single neuron activity. Then, the physiology of pain is explained in chapter 3. This chapter aims to explain the definition of pain, how pain signals are transmitted to the brain by relay neurons and how they are modeled in some works found

in the literature. In chapter 4, we show that a fast and a slow feedback are sufficient to model simple patterns. The behavior of the model and its dynamics are detailed as it represents the basis of following chapter. To complexify the response of the model, a new model is created based on the one presented and studied in chapter 4 and on an additional ultra-slow negative feedback, much slower than the two first feedbacks considered. This new model is presented in chapter 5 and aims to model bursting, a specific firing pattern shown by relay neurons involved in pain generation. As these neurons are able to show an even more complex behavior, called plateau potentials, an additional super-slow positive feedback is added to the model presented in chapter 5. The timescale of this feedback is higher than the first two feedbacks used alone in chapter 4 and lower than the ultra-slow feedback added in chapter 5. The study of the new model created with the 4 types of feedback is the subject of chapter 6. Finally, the conclusion of this work and its prospects are presented in chapter 7.

The codes used to make the simulations described in this report have been developed in *Julia* and are available in this repository: https://github.com/anadew2/IF-modelfing-of-DHNs/tree/main/Codes.

Chapter 2

Electrophysiology and modelling of single cell neuronal activity

2.1 Electrophysiology of a neuron

This section aims to set the basis of this work by explaining what is a neuron. To do so, we follow the ideas of the first chapters in the reference book [Bear, 2007].

2.1.1 The neuron

Cells are the smallest units of life in all known organisms. Each cell is separated from the extracellular medium by a plasma membrane and count generally only one nucleus. A given cell can specialize to perform a specific process in order to form specialized tissues. Cells can be specialized for sensing a particular stimulus in their environment, for transporting specific molecules such as oxygen or even for producing a force. Tissues assemble to form organs. Several organs can work together to treat specific functions of the body. A group of organs working together is called a system.

In this work, we focus on the behavior of particular cells of the nervous system, called *neurons*. Indeed, neurons have the ability to sense their environment, communicate with each other through electrical and chemical signals, and modulate the body's response to a change in its environment. Therefore, neurons constitute a great majority of the basic building blocks of the human nervous system.

Biological structure

Neurons have a particular structure. Indeed, at the center of Figure 2.1.1, we can observe the cell body, called *soma*, that contains the cell nucleus. Neurons are characterized by thin tubes that radiate away from the soma. These thin tubes are called neurites and they are split into two categories: dendrites and axons. Usually, only one axon emanates from the soma. Axons have approximately a constant diameter and can be as large as the order of a meter. The axon sometimes branches, usually with a right angle. In contrast, dendrites rarely extend to more than 2mm from the soma. Also, their diameter is not constant: it increases in direction of the cell body. Usually, there are a large number of dendrites emanating from the soma.
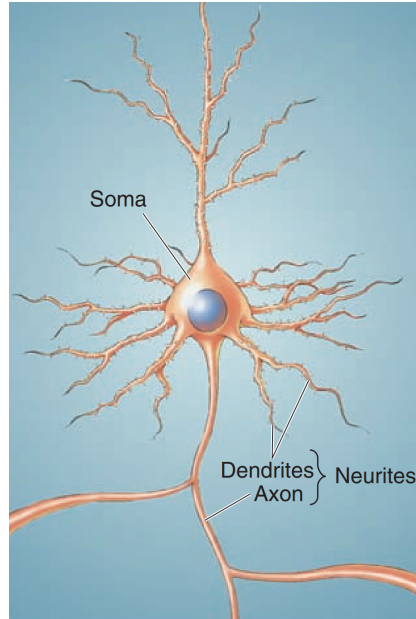
Figure 2.1.1: Structure of a neuron. The basic parts of a neuron are shown: the soma, the dendrites and the axon. [Bear, 2007]

The particular structure of neurons, separated from the extracellular environment by a plasma membrane, relies on a complex internal architecture. All cells are delimited by a plasma membrane but in the particular case of neurons, this membrane is also called neuronal membrane. The plasma membrane is a lipid bilayer where proteins are intercalated, making it semi-permeable. In its internal architecture, we consider the cell subunits that participate in the cell metabolism, called organelles.

Membrane potential

Organelles are to the cell what the organs are to the human body. A large majority of them are contained in the soma. These subunits are bathed in a solution which is the intracellular medium, called *cytosol*. This solution is composed of multiple ions: Na^+ (sodium), Cl^- (chloride), Ca^{2+} (calcium) and K^+ (potassium). The intracellular concentration of each of these ions can vary: these ions can flow in or out the neuron due to the semi-permeable membrane. More precisely, some proteins are specialized to manage selectively the flow of specific ions, they are called *ion channels*.

Ion channels, as their name indicates, are formed by a channel between the intracellular and the extracellular media and two gates: the activation and the inactivation gate. However, some channels do not bear an inactivation gate. If one of the gates of an ion channel is closed, no ion can flow in this channel. The gates opening of a given ion channel depends either on the voltage difference at the cell membrane or on a given ion concentration, such as Ca^{2+} (calcium) or K^+ (potassium). A majority of these ion channels are voltage-dependent. When the cell is at rest, intracellular ions concentrations are fixed. Therefore, the membrane potential at rest is fixed at a precise value and does not vary unless if an induced change in the membrane potential appears. This steady-state potential is negative and approaches $-65\,\mathrm{mV}$, measured as the voltage difference between the intracellular and the extracellular media.

The membrane potential at rest can be exactly calculated using the Goldman equation, where the relative permeability of the membrane to each ion is taken into account, so that the electrical potential difference balances each ionic concentration gradient. This equation is a more complete form of the Nernst equation that only considers the permeability of the membrane to only one ion, leading to the equilibrium potential related to this ion. This equilibrium potential is sometimes called reference potential too. This measurement is indeed helpful to understand the dynamics of ions flow when we consider only one type of ion channel. In fact, as all ion concentrations are different depending on the ion and the side of the membrane, reference potentials of distinct families of ion channels are also different. For a given state of the membrane potential, some ion channels families will thus be activated while others will not. Thus, distinct reference potentials allow to cover a large range of values of the membrane potential.
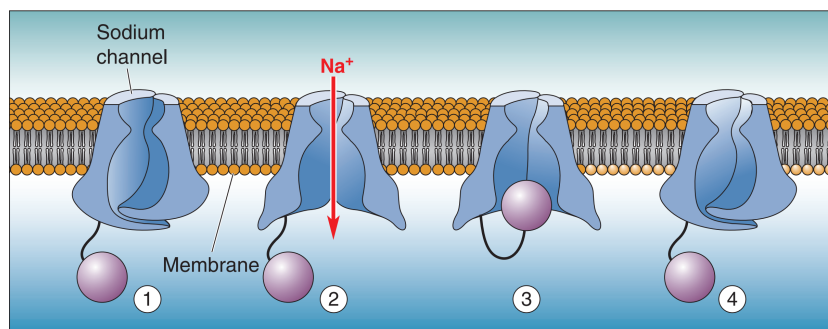
Figure 2.1.2: Evolution of the activation and inactivation gates of a sodium channel through time during an action potential. Only the state 2 lets the sodium ions flow through the channel. The activation gate is shown in blue at the bottom of the channel and the inactivation gate is in purple. [Bear, 2007]

In Figure 2.1.2, we can observe how the opening of a sodium (Na^+) channel and the position of the gates are modified with the cell potential. Globally, if the cell is excited for any reason, the ion channels gates can open in response to the voltage change. If this voltage variation induces the activation and the inactivation gates to open, the channel is thus said to be open. In response, the ions that can go through the considered family of ion channels diffuse and flow inward or outward the cell, according to their gradient. In practice, we know that different families of ion channels can be activated or inactivated at different voltages or ion concentrations. Therefore, different families of ion channels can be successively opened in response to an excitation from a stable state of the membrane potential. The corresponding succession of ions flows and membrane potential variations following a precise timing is referred to as *action potential* or spike.

The action potential is an electrical signal with a characteristic shape of spike. It can be decomposed into different phases according to Figure 2.1.3. This figure shows a recording of an action potential observed using an oscilloscope and its decomposition into different phases. Starting from the resting potential around $-65\,\text{mV}$, the first phase is the depolarization, also called *rising phase*. The voltage difference at the cell membrane increases during this phase. In fact, the cell potential increases due to a fast inward flow of positive ions Na^+ (sodium), governed by their electrochemical gradient. Indeed, at a cell potential
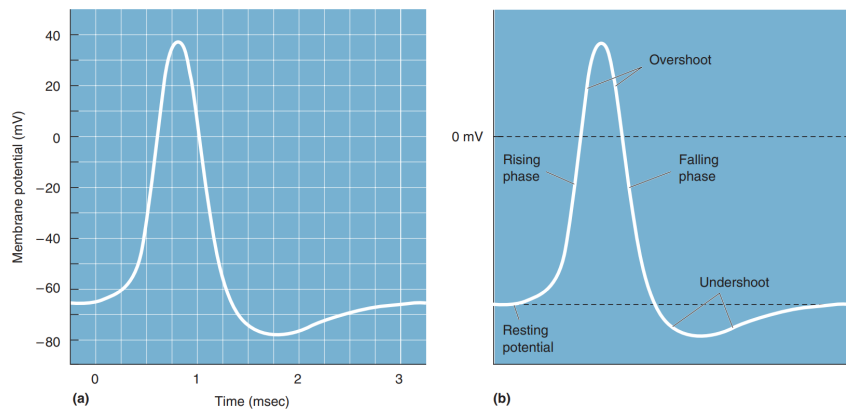
Figure 2.1.3: Action potential observed at the neuronal membrane, measured using an oscilloscope (a), and its characteristics (b). [Bear, 2007]

slightly higher than the steady-state value, the activation and inactivation gates are both open and let the sodium ions diffuse. At the end of the depolarization, the voltage difference at the plasma membrane approaches $40\,\mathrm{mV}$. The cell is thus positively charged. The voltage becomes too high for the inactivation of sodium channels to still be open. Therefore, the inward flow of positive charges almost disappears. For such a high value of cell potential, the voltage-gated potassium channels become open. The potassium ions (K^+) are then driven by their electrochemical gradient, which gives rise to the repolarization of the cell, also called *falling phase*. The membrane potential falls below the resting potential. At this point, the sodium channels are deinactivated but the activation gate closes and the flow of sodium channel is still null. As the membrane potential decreases due to the outward flow of K^+ ions, the potassium ion channels eventually close. As all channels are closed, the cell is then driven towards its resting state. Globally, the activation of voltage-dependent sodium channels is fast while their inactivation and the activation of voltage-dependent potassium channels are slow.

Communication between neurons

The action potential is one of the means of communication between two neurons. Let us take the example of a neuron specialized to sense a specific type of stimulus, such as the sensing of mechanical deformation realized by specific neurons of the skin called mechanoreceptors. When the neuron is deformed under a sufficient mechanical stimulus, it is subject to the generation of an action potential. This spike propagates through the axon from the soma to reach a synapse. From there, the electrical signal is converted into a chemical signal by the means of neurotransmitters and ions. This chemical signal eventually reaches the receptors of the next neuron dendrites and is transduced back into an action potential. Since the diameter of a dendrite increases in the direction of the soma, the electrical signals progress in the dendrites in direction of the cell body. The cycle is then repeated to communicate with other neurons, possibly to process information in series or in parallel.

However, neurons have other ways to communicate than simply send a spike. Indeed, spikes usually combine to form specific patterns. These patterns allow to code the information to transmit with the frequency and the number of spikes used. In this manner,

the electrical signal bears all the information needed by the human brain to understand its environment and make decisions in response to the input stimulation.

2.2   Computational modeling of a neuron

To fully understand the ionic exchanges involved in the generation and the propagation of an action potential, a comprehensive model is needed. As the shape and the generation of action potentials are complex, one can consider a complex and high-dimensional model. This type of model is very convenient to simulate the electrical behavior of a given neuron with appreciable accuracy. However, one can also consider low-dimensional models, much easier to compute and giving other clues about the key mechanisms behind the generation and the propagation of action potential. This section aims to present some examples of these two types of models.

2.2.1   Hodgkin–Huxley conductance-based general model for neurons

Motivation

In 1952, Hodgkin and Huxley proposed the first conductance-based model Hodgkin and Huxley [1952]. As its name induces, this model is based on an electrical model of the neuronal membrane. To develop their model, they referred to many in vitro experiments on an isolated squid giant axon. Using a conductance-based model, they achieved to demonstrate that relatively simple changes in the neuronal membrane permeability can be enough to capture the dynamics of action potentials generation and propagation. Thanks to this important breakthrough in the field of neuron modeling, they were awarded a Nobel Prize.

Framework

They first considered that the plasma membrane has a certain capacity C_m per unit of area. The total current flowing in the plasma membrane is decomposed into the current flowing in the capacitance and 3 other currents: the current of sodium ions (I_{Na}), the current of potassium ions (I_{K}) and a leak current (I_l). The leak current accounts for all other ion channels, whose dynamics are not explicitly taken into account in the model. The capacitance current is, by definition proportional to the time variation of the voltage. Figure 2.2.1 shows the present electrical model of the neuronal membrane. Based on Kirchhoff's theory, we can write an equality between the current inside and outside the membrane:

$$C_m \frac{dV}{dt} = I_{\mathrm{app}} - I_{\mathrm{Na}} - I_{\mathrm{K}} - I_{\mathrm{l}}, \tag{2.2.1}$$

where I_{app} is the current applied at the neuronal membrane, V the membrane potential referenced to the membrane potential at rest, t is the time and C_m the membrane capacity.

From there, it is assumed that each of these 3 currents is proportional to a certain voltage difference. The whole mechanism of spike generation is assumed to rely on dynamic and simple changes in conductance. Each of these conductances links one of the 3 ionic currents to the relative difference between the membrane potential and a reference potential. This reference potential is the Nernst potential. In other words, its value is the potential at which the electrical forces balance the diffusion forces on the considered ions. The conductances
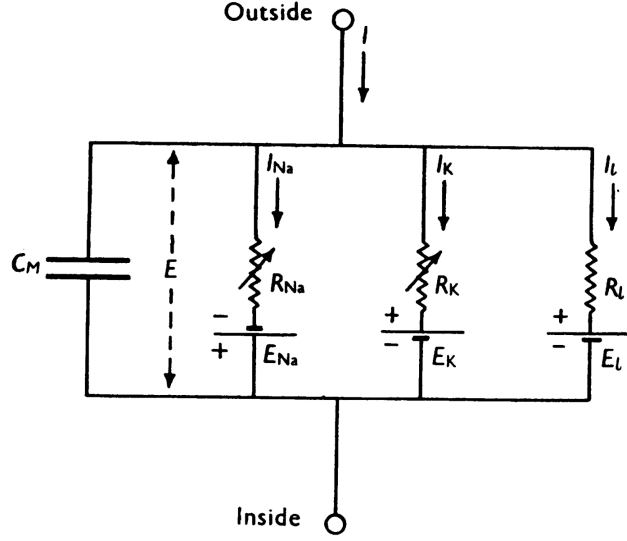
Figure 2.2.1: Electrical model of the neuronal membrane. [Hodgkin and Huxley, 1952]

are then fully defined by the following equations:

$$I_{\mathrm{Na}} = g_{\mathrm{Na}}(V - V_{\mathrm{Na}}),$$
$$I_{\mathrm{K}} = g_{\mathrm{K}}(V - V_{\mathrm{K}}),$$
$$I_{\mathrm{l}} = \bar{g}_{\mathrm{l}}(V - V_{\mathrm{l}}).$$

The conductance associated to the leak current $\bar{g}_{\mathrm{l}}$ is fixed. The other conductances g_{Na} and g_{K} are the dynamic conductances associated to the current I_{Na} and I_{K} respectively. These conductances are assumed to be a function of time. In fact, they are modeled based on a maximum value of the same conductance and one or two time-dependent functions. The latter are the activation and the inactivation of the ion channel. In fact, the activation function is always necessary to model the conductance of the ion channel, but not always the inactivation. These functions make the link with the kinetics of the considered ion channels, which are known to be subject to activation (and sometimes inactivation) across time.

The potassium ion channels are well represented by only an activation function. The conductance of potassium ion channels depends on the fourth power of the activation function n. This power is chosen to best fit the time evolution of the potassium ion channels conductance and corresponds to the number of activation gates in the channel. Similarly, the sodium ion channels conductance is proportional to the third power of the corresponding activation function m. These ion channels are also proportional to an inactivation function h, having only one inactivation gate. The activation n can also be seen as the probability for the ion channels considered to be activated. This assertion is also valid for the other activation m and the inactivation h. The equations linking the two dynamic conductances with their activation and inactivation functions are:

$$g_{\mathrm{K}} = \bar{g_{\mathrm{K}}} n^{4}$$
$$g_{\mathrm{Na}} = \bar{g_{\mathrm{Na}}} m^{3} h$$

8

Each activation/inactivation function can be modeled by a simple first-order ordinary differential equation. The update of each activation/inactivation depends on its steady-state and a time constant, both defined with respect to a given voltage. Each activation/inactivation steady-state and time constant are shown in Figure 2.2.2 as functions of the membrane potential. For example, the steady-state of the potassium channel activation at voltages near rest is close to 0, meaning that a majority of these channels are closed. When the voltage is at the maximum of an action potential, the steady-state of the activation n of the potassium channels is close to 1, meaning that a majority of them is activated. Therefore, a sigmoid is suited to represent the voltage dependency. The same reasoning is applied for the other activation m and the inactivation h, taking into account the kinetics of the considered channels. The time constant is a unimodal function of the membrane potential and usually stays in the same range. This allows to classify the ion channels in terms of their speed. Considering only the sodium and potassium channels, the model is characterized by two timescales : a fast activation of the sodium channels, a slow inactivation of the sodium channels and a slow activation of the potassium channels. The update of the activation and inactivation functions are thus defined by:

$$\frac{dn}{dt} = \frac{n_\infty(V) - n}{\tau_n(V)},$$
$$\frac{dm}{dt} = \frac{m_\infty(V) - m}{\tau_m(V)} \text{ and}$$
$$\frac{dh}{dt} = \frac{h_\infty(V) - h}{\tau_h(V)}.$$
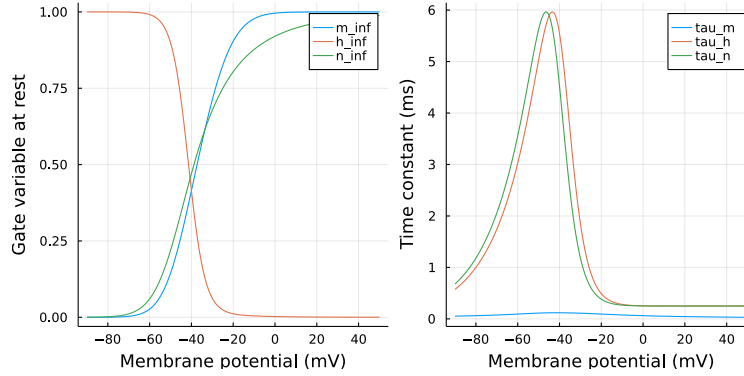
Figure 2.2.2: Steady-states and time constants of the activation and inactivation of the sodium and potassium ion channels as function of the membrane potential, simulated based on the equations of [Hodgkin and Huxley, 1952]

Finally, the model can be summarized by the 4 following equations :

$$\begin{cases} C_m \dfrac{dV}{dt} &= I_{\text{app}} - \bar{g}_{\text{Na}} m^3 h (V - V_{\text{Na}}) - \bar{g}_{\text{K}} n^4 (V - V_{\text{K}}) - \bar{g}_{\text{l}} (V - V_{\text{l}}) \\ \dfrac{dn}{dt} &= \dfrac{n_\infty(V) - n}{\tau_n} \\ \dfrac{dm}{dt} &= \dfrac{m_\infty(V) - m}{\tau_m} \\ \dfrac{dh}{dt} &= \dfrac{h_\infty(V) - h}{\tau_h} \end{cases} \qquad (2.2.2)$$

As it can be seen in Figure 2.2.3, the results of this model are very good and allow to capture the kinetics of the action potential generation. Another strength of this model is that it can be adapted to model any neuron, provided that we consider the ion channels impacting the electrical behavior of the membrane. Their conductance is therefore modeled based on the same reasoning applied to model the conductances g_{Na} and g_{K}.
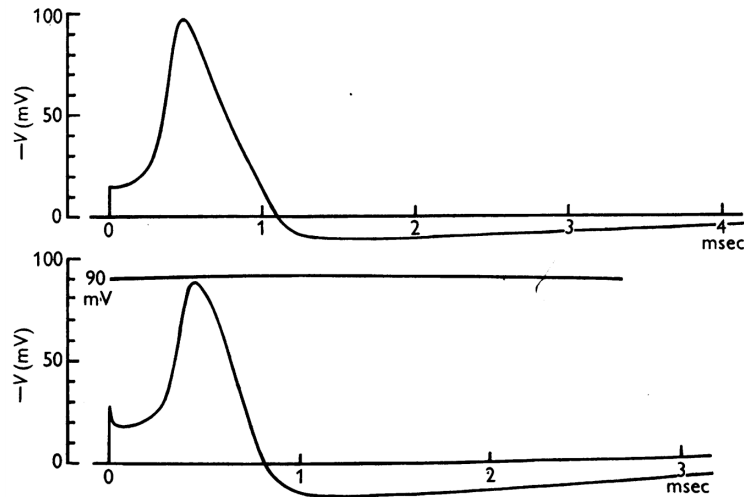
Figure 2.2.3: Action potential simulated with the Hodgkin-Huxley model (up) and recorded in the squid giant axon (down). [Hodgkin and Huxley, 1952]

2.2.2 From conductance-based models to hybrid models

Motivation

Conductance-based models can lead to accurate modeling of the electrophysiology of neurons, at the cost of their complexity. Indeed, they usually take many parameters into account and their fitting is usually tedious. The problem with this approach is that it can become difficult and very costly to capture the key dynamics behind a complex electrical pattern with conductance-based models. Therefore, we need a simple model that would capture the neurocomputational features of the considered neurons.

Two types of models with less parameters can be used : continuous reduced models and hybrid reduced models. Reduced models are based on conductance models and use a certain number of assumptions, notably using timescale separation in the ion channels kinetics, to obtain a model that approaches the behavior of the conductance-based model. The difficulty of getting these reduced models lies in the reduction method. Indeed, the reduced model needs to keep the same properties as the original model. Hybrid reduced models can be associated to continuous reduced models with a further simplification. Typically, they combine continuous spike-generation mechanisms (as continuous reduced models do) and the economy of a discontinuous after-spike reset of state variables. The main advantage of hybrid models is that they match neurons dynamics instead of their electrophysiology.

10

Leaky Integrate-and-fire model

More specifically, we focus on a family of hybrid models that is popular to simulate spiking neurons, called integrate-and-fire models [Izhikevich, 2010a,b]. The simplest model of this family is the leaky integrate-and-fire model. This model is not a spiking model as it lacks an intrinsic spike generation mechanism. In fact, this type of model is more of a threshold model. It is indeed defined by a linear differential equation characterizing the subthreshold dynamic and by a reset rule, which is simply a threshold above which the state variables are reset.

$$C\dot{V} = -g_{\text{leak}}(V - E_{\text{leak}}) + I_{\text{app}}(t), \qquad \text{if } V \geq V_{threshold}, \text{ then } V \leftarrow c.$$

The subthreshold dynamic of this model only considers a fixed ohmic leak conductance g_{leak} to account for all ion channels. This leak conductance is also associated with the Nernst potential E_{leak}. Provided a sufficient applied current $I_{\text{app}}(t)$, the membrane potential V increases until a threshold $V_{threshold}$ and is then reset to the state c and the potential increases again until the reset.

This simple model shows a certain number of neurocomputational properties needed to study the electrical behavior of a population of neurons. First, the shape of spikes created under a sufficient applied current is not simulated but dictated by the reset. Therefore, the leaky integrate-and-fire model has "all-or-none" spikes as they have all the same shape and duration. Second, the hypothetical neuron fires as soon as the membrane potential is above the value $V_{threshold}$, which sets its excitability threshold. In the same manner, we observed a relative refractory period where the membrane potential returns to rest at the end of an action potential, we see that the hypothetical neuron is less excitable immediately after the reset when the reset state c is lower than E_{leak}. Moreover, we observe that the hypothetical neuron can be excited if the current is positive or inhibited if the current is negative, which is similar to the distinction between inhibition and excitation in real neurons. Finally, the hypothetical neuron is able to fire with a frequency that depends on the strength of the applied stimulation.

Being so simple, the leaky integrate-and-fire model has some flaws. The bifurcation of the model from rest to repetitive spiking (or inversely) is different than what is observed in conductance-based models and it has an impact on the electrical pattern of the hypothetical neuron. Moreover, this model cannot show spike latency as the neuron directly spikes when the threshold is exceeded.

Quadratic Integrate and Fire model

The quadratic integrate-and-fire model is an early example of a successful combination of the economy of integrate-and-fire model with physiological interpretability. The Izhikevich model is a quadratic integrate-and-fire model that is used for neuromodulation [Izhikevich, 2010a,b].

$$C\dot{V} = k(V - V_{rest})(V - V_{thresh}) - V_s + I_{\text{app}} \qquad \text{if } V \geq V_{peak}, \text{ then}$$
$$\dot{V}_s = a(b(V - V_{rest}) - V_s) \qquad\qquad V \leftarrow c, \text{ and } V_s \leftarrow V_s + d.$$

This model shows several differences from the leaky integrate-and-fire model. First, they consider here two types of variables: a fast one, the membrane potential V, and a slow one V_s. The latter allows to account for the refractoriness of excitability induced notably by the potassium ion channel opening. Secondly, the time derivative of V grows as kV^2 provided that the membrane potential is high enough. This is a source of negative conductance that is necessary to model an action potential generation with physiological sense. To contrast with the leaky integrate-and-fire model, the threshold potential V_{thresh} is not involved in the reset rule. In fact, the reset is here applied to limit the escape to infinity involved by the gradient. Therefore, the potential V_{peak} is chosen high enough to represent the spike maximum. Once this value is reached, the potential is set back to a lower value c. It corresponds to a shortcut in the action potential shape. The quadratic integrate-and-fire model is thus a spiking model and not a threshold model. Being slower, the variable V_s is not set to a precise value but rather increased by a value d. The parameters a and b must be chosen to verify that the update equation of the membrane potential has a smaller timescale than V_s.

Mathematically, the bifurcation shown by the QIF (quadratic integrate-and-fire) model is closer to what is observed for conductance-based models. Indeed, the QIF model is subject to a saddle-node bifurcation. This type of bifurcation induces here a soft and dynamic threshold that enables spikes to be generated with certain latencies for a given stimulation. The physiological meaning of this model is thus better overall than the leaky integrate-and-fire model. In Figure 2.2.4, We compare the time simulation of the leaky integrate-and-fire (LIF) model with the results of the Izhikevich model for the same pattern of applied current. This comparison allows to visualize the differences between these two models and the improvements in the spikes shape and physiological meaning provided by the quadratic integrate-and-fire model.
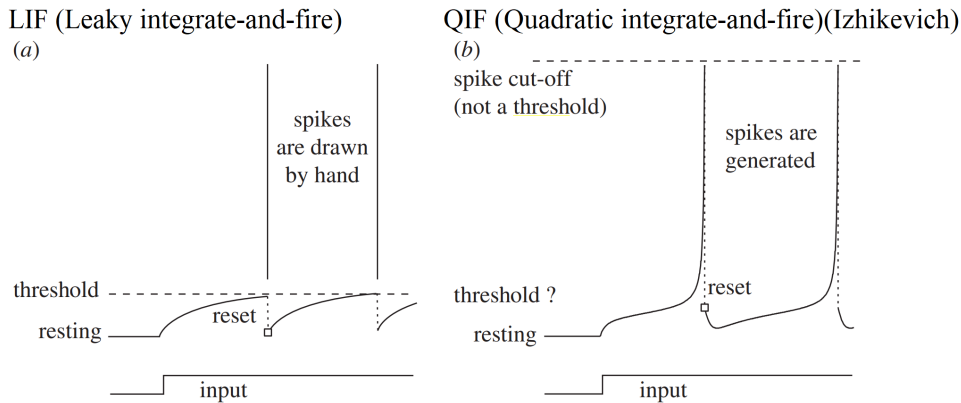
Figure 2.2.4: Response to a step of applied current of the leaky integrate-and-fire model (a) and the Izhikevich model (b). [Izhikevich,2010]

The Hodgkin-Huxley model can be reduced to two ordinary differential equations and compared to the Izhikevich model [Pottelbergh et al., 2018]. A famous reduction of this conductance-based model is the FitzHugh-Nagumo model. This reduction is obtained by exploiting the timescale separation between the fast sodium channels activation, their slow inactivation and the slow activation of potassium channels. In fact, the fast activation is supposed to be at steady-state while the slow activation and inactivation are joined and

expressed by a slow state variable. From there, the first ODE corresponds to the evolution of the membrane potential while the second explains how the slow variable moves with time. By equaling each equation to 0, one can obtain the mathematical expression of the model nullclines. A nullcline is a function of the state variables where the variation of the corresponding state variable is null. A nullcline is represented in a phase plane, which corresponds to the space of the state variables of the considered model. For example, the V_s nullcline is a function of V where $\dot{V}_s$ is 0 according to the definition of the QIF model. This nullcline is represented as a straight line in the phase plane, here the space $(V; V_s)$ where V_s is the slow state variable and V the membrane potential.

The phase plane associated to the FitzHugh-Nagumo model is shown in the left part of Figure 2.2.5. The V nullcline is the black solid line cubic function while the V_s nullcline of this model associated to the slow variable is the black dashed line. The intersection of two different nullclines is a fixed point since the gradient of the state variables is null. The study of the vector field defined by the gradient $(\dot{V}; \dot{V}_s)$ can help to determine the fixed point stability. Its stability can also be determined analytically. If we realize a time simulation of the FitzHugh-Nagumo model for a given time interval, we can compute the traces $V(t)$ and $V_s(t)$ at each time t. Thus, at each time t of the interval, we have a new point $(V; V_s)$ in the phase plane. The curve that is defined by all couples $(V; V_s)$ across time is called a trajectory.

The blue solid line in the left part of Figure 2.2.5 corresponds to the trajectory of the 2D model in the phase plane, simulated with no applied current and with an initial excited state. In our case, an initial excited state corresponds to a membrane potential that is already high such that the action potential is directly generated. Any spike generated by the model described more or less the same loop in the phase plane. For a low applied current, the steady-state found at the intersection of the nullclines is a stable node and the trajectory is attracted towards it. The zoom on this stable node is shown in the right part of Figure 2.2.5. In the latter, we can see the interest of using a reset rule: if we use a short cut in the phase plane, the computation of the model is more efficient. The nullcline of the membrane potential can then be approximated by a quadratic function. This is the reason that motivates the Izhikevich model.
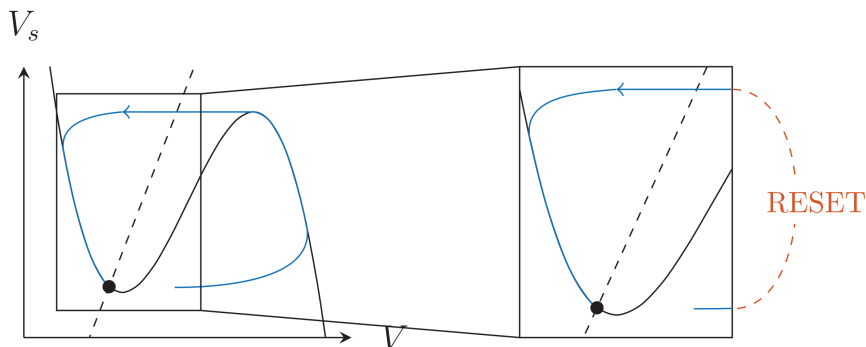

Figure 2.2.5: Phase portrait of the FitzHugh-Nagumo model (left) with a zoom on the fixed point (right). The zoom aims to show the interest of using a quadratic integrate-and-fire model. [Pottelbergh et al., 2018]

Multiple Quadratic Integrate and Fire (MQIF) model

The MQIF is a quadratic-quadratic description of the fast and slow currents with respect to the cell potential. This model aims to account for the non-monotonicity of the slow current, which was not considered by the Izhikevich model [Pottelbergh et al., 2018, 2021]. This model is a reduced model of a more complex model that is able to represent calcium kinetics [Drion et al., 2012; Franci et al., 2012, 2013].

$$C\dot{V} = \bar{g}_f(V - V^0)^2 - \bar{g}_s(V_s - V_s^0)^2 + I_{\text{app}} \qquad \text{if } V \geq V_{\text{max}}, \text{ then}$$

$$\tau_s\dot{V}_s = V - V_s \qquad\qquad\qquad\qquad V \leftarrow V_r \text{ and } V_s \leftarrow V_{s,r}$$

Except for the slow current, this model is similar to the Izhikevich model. The membrane potential is denoted V. The slow current is proportional to the slow potential V_s. The latter is obtained by filtering the membrane potential with a slow time constant τ_s. The conductances $\bar{g}_f$ and $\bar{g}_s$ denote the conductances of the fast and slow ion channels respectively. The potentials V^0 and V_s^0 are the reference potentials of the fast and slow ion channels respectively. As before, the potentials V_{max} and V_r are the potentials needed to set the reset condition and the reset state of the membrane potential. The slow voltage V_s is reset at the fixed value of $V_{s,r}$ whenever necessary. Finally, C and I_{app} denote, as before, the capacity of the neuronal membrane and the applied current at the neuronal membrane.

In 2012, Drion et al. have shown that the present non-monotonicity is suited to model several slow ion channels having the ability to shape the corresponding slow current with a source of negative conductance [Drion et al., 2012]. These ion channels encompass many calcium channels and some fast potassium channels. Due to their ability to give rise to source of a negative conductance, they are qualified as **regenerative**. The ion channels that are not able to generate a source of negative conductance are called **restorative**. Therefore, restorative ion channels are source of negative feedback while regenerative ion channels are source of positive feedback.

If we draw the nullclines of this model in the phase plane $(V; V_s)$, we can see that the quadratic-quadratic description of the current strongly affects the V nullcline, compared to the Izhikevich model. Indeed, this nullcline is cross-shaped around the point $(V^0; V_s^0)$ for a zero applied current. When the current increases, this nullcline looks like two quadratic functions near the point $(V^0; V_s^0)$. When the applied current is negative, this nullcline seems to be turned of 90 degrees in the phase plane. The V nullcline is represented in the phase plane for 3 values of I_{app} in Figure 2.2.6. The computation of this nullcline equation and a more in-depth analysis of the phase plane is realized in section 4.2.

The values chosen for the reference potentials V^0 and V_s^0 have an impact on the behavior of the model. Indeed, for a given value of V^0, the value chosen for V_s^0 will determine if the fixed points are located on the upper branch or on the lower branch, leading to two different types of excitability. In fact, if V_s^0 is lower than V^0, the model is slow restorative. In the reverse case, the model is slow regenerative. Therefore, the reference potential sets the nature of the slow feedback and the behavior of the model.

Slow regenerativity governs important phenomena shaping the electrical activity of the membrane such as spike latency, afterdepolarization potential and bursting. Spike latency
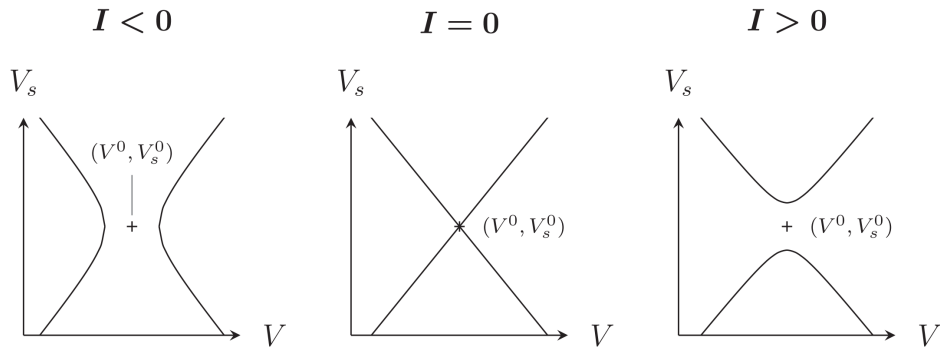
Figure 2.2.6: Nullcline associated to the membrane potential in the MQIF model represented in the phase plane for 3 values of applied current I. [Pottelbergh et al., 2018]

and the afterdepolarization potential can be observed in Figure 2.2.7. This figure shows the evolution of the membrane potential obtained with the MQIF model for a given pattern of I_{app} with 4 pulses of different durations and strengths. The spike latency is the delay between the time at which the applied current changes from 0 to a positive value and the first spike in the membrane potential. This delay depends on the strength of the applied current: the stronger the current is, the lower the spike latency is. The afterdepolarization potential (ADP) is the distinctive small depolarization observed after one or several spikes, when the membrane potential returns to its steady-state. Bursting is a specific pattern described by the membrane potential for a constant positive value of applied current. It is composed of several trains of spikes called bursts with a decreasing instantaneous frequency (called intraburst frequency) separated by quiescent periods. The interburst frequency is constant when the equilibrium is reached. Bursting will be studied in chapter 5.
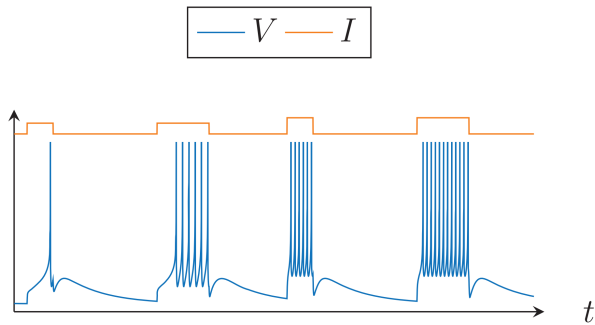
Figure 2.2.7: Simulation of the MQIF model (blue) for a given pattern of applied current I_{app} (orange). [Pottelbergh et al., 2018]

Chapter 3

Physiology of pain

3.1   What is pain ?

To introduce what pain is, we need to set the scene by introducing the part of the nervous system that creates and processes pain: the somatic sensory system. This system is specified to enable our body to feel and to ache by using messages called somatic sensations. This term is used to refer to all the sensations arising from the skin, such as touch, pressure or temperature. When the somatic sensation is so intense that it could lead to a damage in any body part, it is called pain. [Bear, 2007]

"Pain" is used to refer to three quite different things, summarized in the three parts of Figure 3.1.1.[Woolf, 2010] There is the *nociceptive pain* that is the pain being an early-warning physiological protective system. This type of pain is associated to a noxious stimulus such as heat, cold, a intense mechanical force or chemical irritants. The nociceptive pain is a high-threshold and protective electrical signal interpreted by the brain. In other words, if someone accidentally cuts his/her finger, the acute feeling of discomfort instantly felt after the cut results from nociceptive pain signals. Usually, one of the first decisions taken by the brain is to activate the withdrawal reflexes of the individual in order to stop the noxious stimuli. Nociceptive pain is actually essential for maintaining bodily integrity. Indeed, patients that are insensitive to pain loose in fact an early protective warning which aims to keep the body safe. As a consequence, they are often subject to self-mutilation, bone fracture or joint deformities that can lead to early death.

Equally important, another type of pain is the *inflammatory pain* which assists healing of an injured body part by creating an hypersensitivity to pain. Typically, if we take back the example of a finger cut, the inflammatory pain is the ache felt hours and days after the cut, which keeps away the damaged tissue of being touched. This type of pain also appears in response to the inflammation of a body part. In fact, it is activated by the immune system and it is thus favored by inflammation factors. Inflammatory pain is low-threshold and more extended in time form of pain. This type of pain aims to protect an injury too, particularly during healing in this case.

Finally, some of us show abnormal pain signals called *pathological pain*. This last type of pain is associated to a disease state of the nervous system. Pathological pain can be divided into 2 sub-types: the neuropathic pain and the dysfunctional pain, both being low-threshold and maladaptive. In the case of neuropathic pain, the disease state appears in response to a neural lesion of the nervous system. To contrast, dysfunctional pain signals are produced
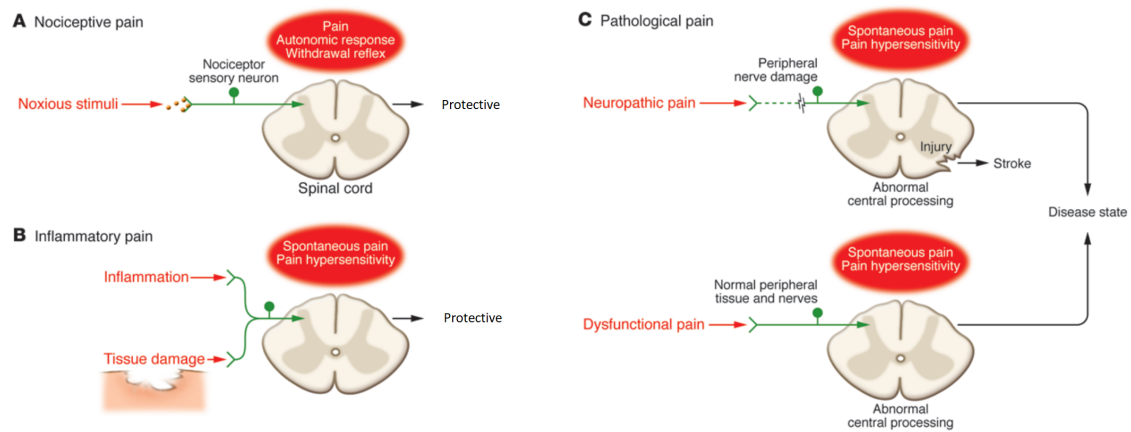
Figure 3.1.1: Pain classification. The three types of pain and their triggers (if existing) are represented. Nociceptors are represented in green: each green dot is a cell body while the straight green lines are Aδ or C nerve fibers. Adapted from [Woolf, 2010].

even if there is no such damage or inflammation to the nervous system. In fact, the dysfunctional pain appears in patients having conditions such has fibromyalgia, irritable bowel syndrome, tension type headache, temporomandibular joint disease or interstitial cystisis. All of these diseases have the same common point: no noxious stimulus is needed to trigger the substantial pain patients feel (as in nociceptive pain generation) and no (or minimal) peripheral inflammatory pathology is at the origin of these signals.

3.2 Pain neural circuits

The feeling called "pain" is usually triggered from peripheral stimuli, sensed by sensory neurons specialized for nociception, called nociceptors. They are free nerve ending: the terminal branches spread in the skin of the individual [Bear, 2007]. The membrane of nociceptors contains ion channels that are able to react to intense thermal, mechanical or chemical stimuli. Therefore, an intense stretch of the skin not only activates the mechanical ion channels of nociceptors but may also damage cells that would release substances that favor the opening of other ions channels in the surrounding nociceptors membrane. Some nociceptors respond to each of these three types of stimuli and others are specialized to respond to only one. The noxious stimuli are then converted into action potentials.

Nociceptive signals in the form of an electrical signal are conveyed through two types of nerve fibers called Aδ fibers and C fibers [Bear, 2007]. The name attributed to these nerves is based on the composition of the corresponding nociceptors axon. The Aδ fibers are thinly myelinated and wide, while the C fibers are unmyelinated and more narrow. Nociceptive signals are thus transmitted at two different speeds to the spinal cord. The Aδ fibers being wider, the conduction velocity is between 5 and 30 m/s while the maximum conduction velocity of C fibers is 2 m/s. As summarized in Figure 3.2.1, the pain intensity in response to a punctual noxious stimulus across time is thus a special pattern. Having a higher conduction velocity, Aδ fibers are associated to a first and sharp spike of pain intensity called *first pain*, while C fibers activation induce *second pain*, a long-lasting but lower in intensity pain sensation.

17
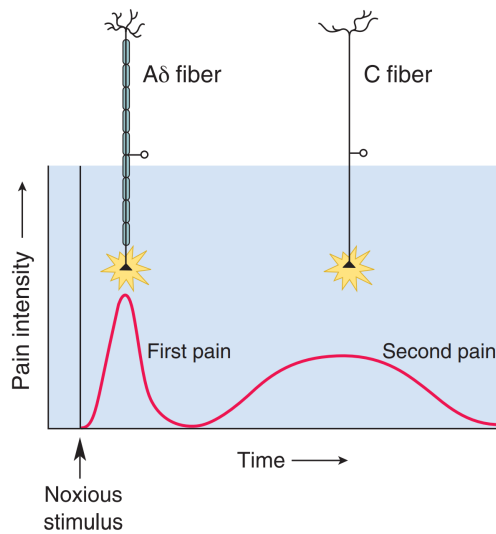
Figure 3.2.1: First and second pain. The first peak is mediated by Aδ inputs while the second long-lasting signal is triggered by C fibers inputs. The circle represented at the middle of each fiber is the nociceptor cell body. [Bear, 2007]

The nerve influx travels in direction of the soma of nociceptors, located in the dorsal root ganglia. To communicate with the brain, the nerve fibers enter the dorsal horn of the spinal cord through the zone of Lissauer. [Bear, 2007] The dorsal horn is a part of the spinal gray matter. In fact, the synapses of nociceptors modulate the activity of dorsal horn neurons (DHNs) located in the substantia gelatinosa. Figure 3.2.2 shows the cell body (purple dot in the dorsal ganglia) of a C fiber nociceptor that communicates with DHNs, located in the green area where the substantia gelatinosa is. The signals produced by the DHNs are processed next by the thalamus, as the nerve fibers of the DHNs project up to the spinal cord through the medulla pons and midbrain. This path is the spinothalamic pathway. In addition, the trigeminal pathway is the path taken by nociceptive signals that come from the face. Similarly, nociceptive signals are also relayed by other neurons having the same role as DHNs before being processed by the thalamus. The output signals of the thalamus nuclei are then interpreted by the primary somatosensory cortex.
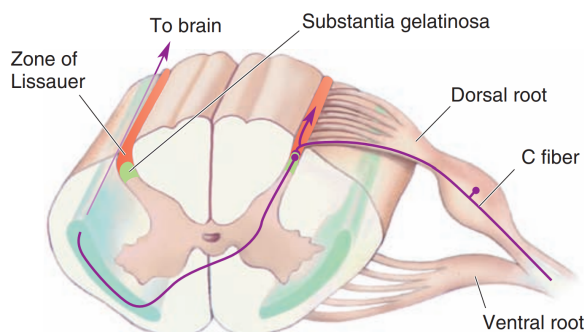
Figure 3.2.2: Spinal connections of nociceptive axons. The cell body of the purple C fiber nociceptor is located in the dorsal root ganglia. Nociceptive signals are conveyed by C fibers and enter the dorsal horn by the dorsal roots. The relay DHNs are located in the green area, called substantia gelatinosa. [Bear, 2007]

18

Pain can be either diminished or exaggerated depending on mood, cognitive functions or memories. Such a high-level control of the brain is part of a descending regulation from the brain. The periaqueductal gray matter (PAG) is a zone of neurons in the midbrain that has the ability to inhibit nociception. The axons of PAG allow to communicate with regions of the medulla such as the raphe nuclei, second to last relay for the descending regulation. The inhibition controlled by the brain acts finally on the DHNs. Thus, the electrical stimulation of the PAG can almost entirely suppress pain sensation.

3.3 Electrophysiology of dorsal horns neurons

3.3.1 Physiology

Dorsal horn neurons (DHNs) are the first relays for nociceptive information. Indeed, DHNs are the first neurons to receive the action potentials generated by the nociceptors. In parallel, they also receive other sensory signals such as touch sensations or proprioception signals from non-nociceptive mechanoreceptors.[Bear, 2007] The role of DHNs in nociception is to integrate and modulate input nociceptive signals. To do so, they are embedded into a small network in the dorsal horn where their activity is controlled by other neurons, as the gate-control theory of pain postulates.

In Figure 3.3.1, we can observe a schematic view of the substantia gelatinosa, a part of dorsal horns, realized based on the gate-control theory of pain.[Bear, 2007] The red track represents the nerve fibers that convey nociceptive signals. The blue track shows the path taken by the non-nociceptive sensory information, which is separated from the path taken by pain signals but still impacts pain signals transmission. In this figure, only two neurons are represented: a projection neuron and an interneuron. The projection neuron aims to send the information to the thalamus through the medulla. The output signal produced by the projection neuron is therefore sent on the spinothalamic path. The nociceptive signals sent to the brain are also modulated by the activity of an interneuron that also depends on both nociceptive signals and non-nociceptive sensory signals, from mechanoreceptors for example.

The actual network behind pain processing is much more complex and not well understood. Every week or month, there is a new paper about this particular network, each with new assumptions. Among them, a network will be presented later in section 3.4 for a clarity purpose with a proposed electrical treatment for pathological pain.

3.3.2 Functional states

Dorsal horn neurons (DHNs) have the ability to change their firing pattern, which in term modifies the information sent to the brain.[Derjean et al., 2003; Marder, 2003] The first firing pattern observed was the *tonic firing*. For a pulse of current delivered in the nociceptive fibers afferent to a given DHN, tonic firing is observed when action potentials are produced with a constant frequency, as shown in the left part of Figure 3.3.2. When delivering several shorter pulses to tonic DHNs, the output signal follows the global characteristics of the input signal but usually with a lower frequency. For the same input pattern made of short pulses, DHNs sometimes responded with a higher frequency and an accelerating spike train. This type of response is associated to the second DHN firing pattern called *plateau potentials*. Whether the input signal is composed of a wide pulse or of several short pulses, this pattern is always characterized by an afterdischarge where
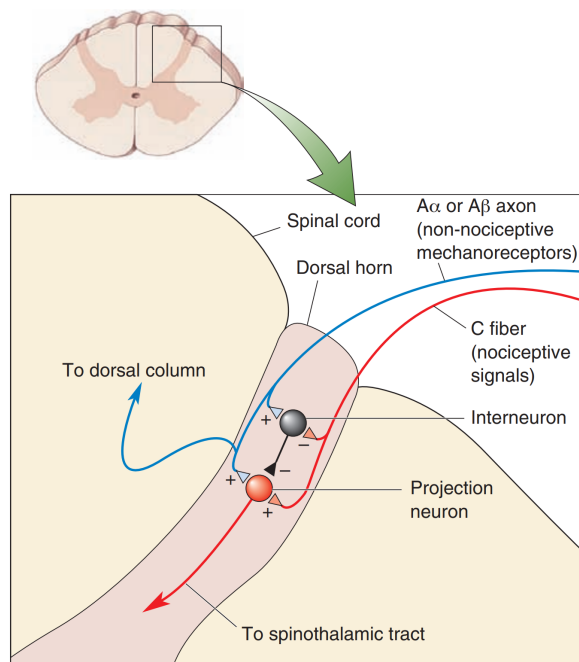
Figure 3.3.1: The gate theory of pain. Pain signals transmission to the brain realized by a projection neuron is modulated by the activity of an interneuron. Both neurons activity is function of non-nociceptive and nociceptive sensory signals. [Bear, 2007]

endogenous spikes are generated after the end of the last pulse of the input signal (Figure 3.3.2, middle part). Finally, the third possible firing pattern of DHNs is the *rhythmic bursting*, represented in the right part of Figure 3.3.2. This pattern is not triggered by the input signal: rhythmic bursting can be observed even with a "silent" input signal. Bursting is characterized by quiescent periods separated with a train of action potentials called burst with a decreasing instantaneous intraburst frequency. The interburst frequency, being the frequency at which a burst appears, is constant.
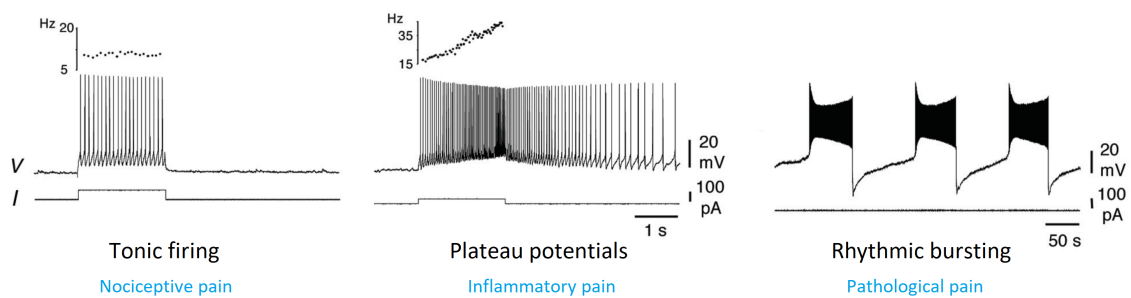
Figure 3.3.2: The three modes of firing of DHNs: tonic firing, plateau potentials and rhythmic bursting. Each firing pattern is associated to one type of pain, added in blue. Adapted from [Derjean et al., 2003].

For Derjean et al., each DHNs firing pattern is assumed to be linked to one type of pain stated in section 3.1. Indeed, each of these output signals shows different properties of pain signal transmission to the brain. Tonic firing is associated with nociceptive pain

signals. Indeed, this firing pattern is relatively good at encoding the intensity and duration of afferent signals from Aδ and C fibers. Inflammatory pain would be associated with the plateau potentials sent by the dorsal horn neurons. As the generation of action potentials outlasts significantly the duration of afferent nociceptive signals, plateau DHNs amplify the input signal in situations of central sensitization to pain. This firing pattern is indeed the more efficient to transfer input signals. Finally, DHNs showing rhythmic bursting are associated to the generation of pathological pain. Indeed, during the quiescent periods of bursting, a large majority of the input nociceptive signals from Aδ and C afferent fibers is filtered out by this relay. Similarly, during burst, input nociceptive signals leave the firing pattern almost unchanged. Therefore, rhythmic bursting is analogous to a loss in DHNs coding abilities.

DHNs firing pattern would be determined by a dynamic balance of metabotropic controls on inwardly rectifying potassium (Kir) channels of DHNs dendrites according to [Derjean et al., 2003]. One possible explanation is that the Kir channels in the grip of this regulation are activated as a result of a number of metabolic steps that are used for stimuli transduction. Two substances act as neurotransmitters on Kir channels activation: glutamate and GABA. Glutamate has an impact similar to an excitatory neurotransmitter while GABA is more of an inhibitory neurotransmitter. Therefore, the balance between the activation and inactivation of the Kir channel is at the source of change in DHNs firing patterns. However, the Kir channels may not be the only control mechanisms for DHNs firing patterns.

An interesting property also shown by DHNs firing patterns is wind-up.[Aguiar et al., 2010] This phenomenon is a frequency-dependent adaptation of the nervous system consisting in an increase of generated action potentials with an increasing frequency of stimuli from nociceptive C fibers. Wind-up is thus a frequency-dependent facilitation process expressed by DHNs which typically exhibit plateau potentials. Indeed, wind-up leads to many of the characteristics that describe central sensitization.

3.4   Spinal cord stimulation

Being an early-warning signal, nociceptive pain is usually not a clinical problem [Woolf, 2010]. However, when surgery or any other clinical procedure involving a noxious stimuli is needed, nociceptive pain should be muted temporary. To do so, clinicians deliver high-dose opioids or local and general anesthetics. In the context of pathological pain, there is no universal solution to relieve patients with chronic pain, representing about 20% of the adult population. The first treatment strategy tested is derived from the clinical strategy to suppress nociceptive pain: a pharmacological therapy using opioids. Unfortunately, this treatment is effective in less than 50% of patients.

As the interest for the electrical properties of the nervous system has grown, clinicians were inspired to develop a new treatment strategy. In fact, they tried to electrically stimulate the nerve fibers involved in pain transmission in order to suppress it, according to the gate-control theory of pain presented in Figure 3.3.1. Several techniques have been developed since but one of the most promising is the Spinal Cord Stimulation (SCS). [Guan, 2012]

Clinically, spinal cord stimulation (SCS) is realized by delivering mild to moderate electrical pulses at various frequencies to the spinal cord in order to ellicit paresthesia (a tingling sensation) in the painful region. This process is realized using an electrode positioned in the epidural space above the spinal segment affected by pathological pain. The electrical stimulation intensity is tuned so that this stimulation stays slighlty below the motor threshold, for obvious pratical reasons, and below the pain threshold, to avoid a painful paresthesia. For animal studies, the antidromic sciatic compound action potential can be monitored in order to ensure the treatment acts below the pain threshold.

The development of SCS was motivated by the gate-control pain theory. Indeed, this theory postulates that DHNs, necessary for pain transmission, can be inhibited by excitatory inputs from motor fibers. The stimulation is therefore applied to the dorsal column that contains motor $A\beta$ nerve fibers acting on the same DHNs which create pathological pain signals. Locally, the inhibition created on the nociceptive afferent fibers results from release of GABA inhibitors. Potentially, SCS can also favor a descending inhibition by releasing the corresponding neurotransmittors. In Figure 3.4.1, we can see an updated version of the gate-control pain theory with the location of the stimulation. In this update, more neurons are taken into account for the pain transmission network: I is the population of spinal inhibitory interneurons, E accounts for the set of excitatory interneurons, T represents the transmission cells population and N is the population of nociceptive-specific projection neurons.

For patients who responded well to this treatment, the pain inhibition often exceeded the duration of the stimulation. This technique is therefore very useful to treat some patients and to relieve them from pathological pain. Moreover, due to the possible enhanced descending inhibition of pain processing, SCS could also help to prevent the later development of pain hypersensitivity. However, detailed knowledge about how SCS inhibits pain is lacking. Indeed, the stimulation parameters (intensity and frequency) are not well defined. The frequency usually used is between 50 and 60 Hz. SCS is shown to work better with lower frequencies because it induces both a local spinal inhibition and a descending inhibition. A deeper understanding of the network SCS acts on could be really beneficial to improve this technique's efficacy on patients.

3.5 Conductance-based models of dorsal horn neuron at the cellular level

In the very scarce literature linked to this topic, some groups of researchers produced conductance-based models to explain the generation of particular firing patterns. [Aguiar et al., 2010; Franc and Masson, 2010; Zhang et al., 2014] To do so, they took many ion channels into account and produced results that had the same properties than the firing patterns considered. Aguiar's and Le Franc's research teams worked on modeling particular characteristics of DHNs. Using these models is very helpful to determine the time scales induced in the DHNs models. Also, these models highlight which ion channels are involved in these firing patterns generation.

3.5.1 Aguiar's model

Aguiar's research team conceived a model to determine the key mechanisms behind windup generation.[Aguiar et al., 2010] The model they developed is a type of compartmental
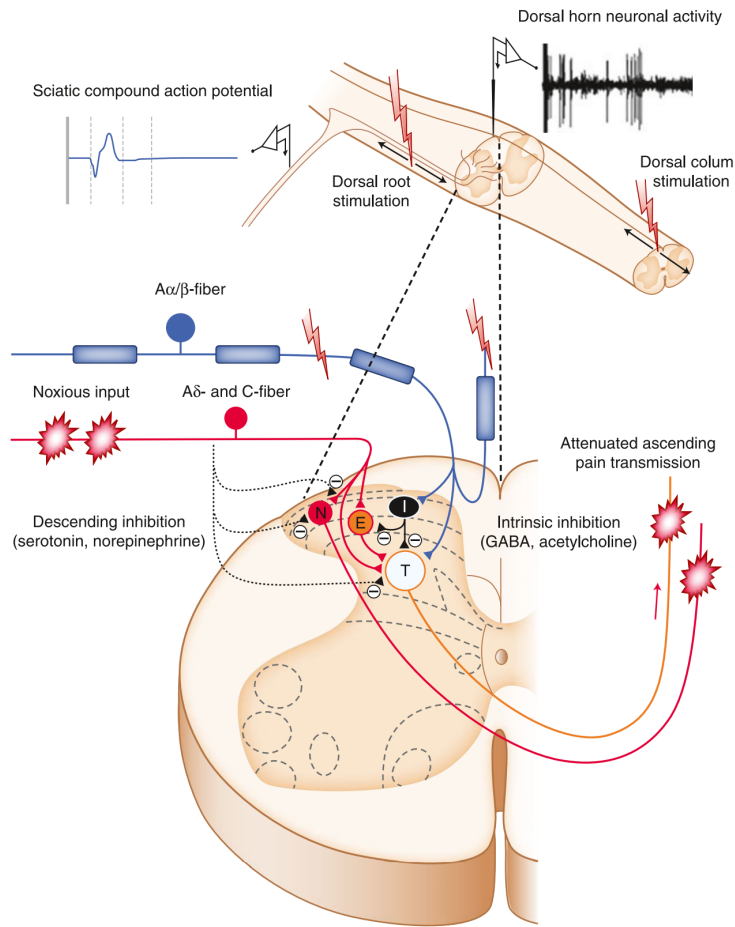
Figure 3.4.1: Schematic diagram representing potential spinal segmental mechanisms underlying pain inhibition induced by SCS. Aα and Aβ myelinated nerve fibers of motor neurons are stimulated below the motor threshold and below the pain threshold to inhibit nociceptive signals transmission to the thalamus. The activity of the tramsmission DHNs "T" is recorded to observe the impact of SCS. "N", "E" and "I" are the neurons embedded in the network assumed to manage pain tranmission. [Guan, 2012]

model, a more complex version of a conductance model. Indeed, conductance models are usually associated with a single punctual neuron. To contrast, compartmental model take into account local biophysical properties at several locations of a given neuron (soma, dendrites, axons, etc). As DHNs behavior depends on interaction between several neurons in an upstream network, Aguiar et al. wanted to take into account both membrane mechanisms and synaptic mechanisms. Thus, they created a small network, made of 2 single cells, based on compartmental models. To keep the DHNs model simple enough, they took into account only one type of interneurons, as it can be seen in Figure 3.5.1. The input of the nociceptive Aδ fibers is delivered directly to the transmission neuron. As the transmission neurons are able to change their firing pattern and give long-range responses, they are called wide dynamic range (WDR) neurons. The authors assumed that the nociceptive signals from C fibers are sent to interneurons that are connected to the transmission (WDR) neurons by a set of synapses. The WDR neuron model is composed of several cylindrical connected compartments representing its dendrites, soma, axon initial segment and axon.

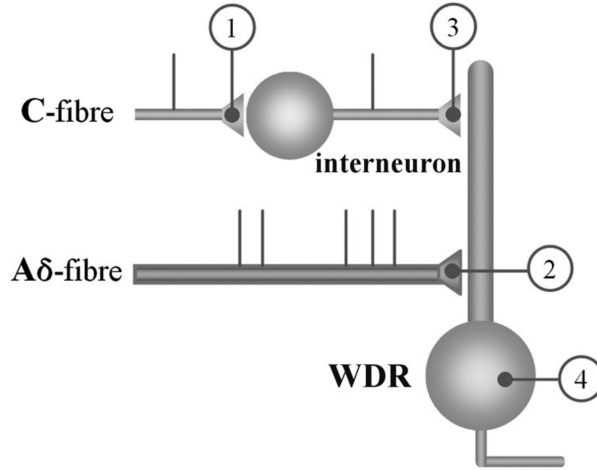Figure 3.5.1: Schematic diagram of the compartmental model used by Aguiar et al. The locations where wind-up possibly takes place are numerated. Wind-up is actually mainly generated at the membrane of WDR neurons (location 4). [Aguiar et al., 2010]

To model the synaptic mechanisms, several synaptic receptors are considered and simulated as conductance changes. Among them, the NMDA and NK1 synaptic receptors are shown to contribute to wind-up in DHNs. Once activated, two types of currents passed through them: a cationic non-specific (CAN) current i_{CAN} and a long-lasting high-threshold calcium current $i_{Ca,L}$. Beside these two currents, the membrane mechanisms integrate the dynamics of the Hodgkin-Huxley currents (a transient sodium current i_{Na} and a delayed potassium current i_K), a calcium-dependent potassium current $i_{K,Ca}$, a persistent sodium current $i_{Na,p}$ and, as usual, a leak current i_{leak}.

Based on experimental measurements of spikes generated with wind-up, Aguiar et al. noticed that a single exponential process is suited to model wind-up time profiles. From there, they could estimate the time constants of the key mechanisms involved in the generation of wind-up, averaged to 5 seconds. This reference helped to determine that the key mechanisms giving rise to wind-up are the time-summation of long-lasting postsynaptic responses produced by NMDA receptors and the cumulative depolarization supported by the cationic non-specific (CAN) current and the long-lasting high-threshold calcium current.

3.5.2 Le Franc's model

Le Franc's model is an attempt to understand the mechanisms involved in the switch in DHNs firing patterns.[Franc and Masson, 2010] As for the Aguiar model, they used a compartmental model. However, they only considered a single cell with two compartments in this version: dendrite and soma. The reason for this simplification is that the authors wanted to focus on DHNs plateau potentials generation.

For each compartment, they considered specific types of ion channels to model the corresponding compartment membrane potential. The currents taken into account to model the soma conductances are the following: the classical fast/slow i_{Na}/i_K Hodgkin-Huxley currents, the fast L-type calcium channels modeled by the current i_{fCaL}, the calcium-dependent potassium channels (i_{SK}), the Kir channels that were associated with the switch of firing pattern i_{Kir} and finally a leak current i_{leak}. There are only 4 currents taken into

account for the dendrite: a slow calcium currents from L-type calcium channels i_{sCaL}, a calcium-dependent cationic non-specific (CAN) conductance i_{CAN} and, as for the soma, a calcium-dependent potassium current i_{SK} and a leak current i_{leak}. A schematic representation of this model is shown in Figure 3.5.2.
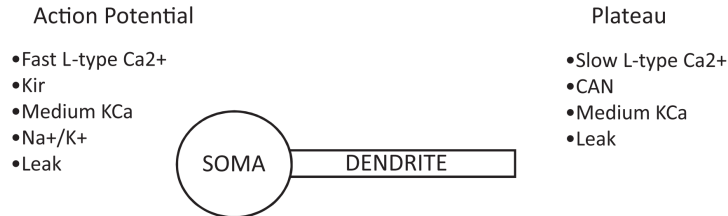

Figure 3.5.2: Schematic representation of the compartmental model used by LeFranc et al. For each compartment, the ion channels considered are listed, on left for the soma and on the right for the dendrite. [Franc and Masson, 2010]

The study of this model allowed to discover a new type of firing pattern at the edge between tonic firing and plateau potentials: the accelerating behavior. This behavior is characterized by an increasing instantaneous frequency during a current pulse and an afterdepolarization potential (ADP) at the pulse end. The analysis of the correlation and contribution between the accelerating mode and the input signal from Aδ fibers highlighted that this firing mode may be an optimal nociceptive signal transmission.

Plateau potentials are the optimal firing pattern for accurate nociceptive transmission due to the signal amplification it creates. This model helped to clarify two mechanisms involved in plateau potentials generation: a voltage-dependent one and a calcium-dependent one. The first mechanism is especially due to the the kinetics of L-type calcium channels, that are voltage dependent. The second mechanism relies on interactions between the L-type calcium channels and the calcium-dependent potassium channels. It was shown that if the latter potassium channels are blocked, plateau potentials cannot be observed anymore. The CAN current is the ion current that has the major impact on the afterdischarge generation in plateau potentials.

In fact, Le Franc et al. show that it is the balance between Kir conductances and L-type calcium conductances of soma and dendrites that defines the electrical behavior of DHNs. The existence of different firing patterns is assumed to be due to the variation of calcium conductances while the Kir conductance defines the switch as it increases the amount of current needed to trigger the DHNs regenerative properties. Figure 3.5.3 shows that the 4 firing patterns of DHNs can be obtained for a large range of conductance values.

To account for the large set of modulatory pathways involved in DHNs firing patterns generation acting on many different targets, the authors considered a mapping of the parameter space that separates the effect of depolarizing (excitatory) conductances from the effect of hyperpolarizing conductances.[Franc and Masson, 2010] Based on this mapping, Le Franc et al. showed that the balance between these two groups of conductances sets DHNs firing patterns. Focusing on the currents involved in plateau potentials generation mentionned above, L-type calcium and CAN conductances are grouped as depolarizing conductances while the Kir and calcium dependent potassium (SK) conductances are grouped

25
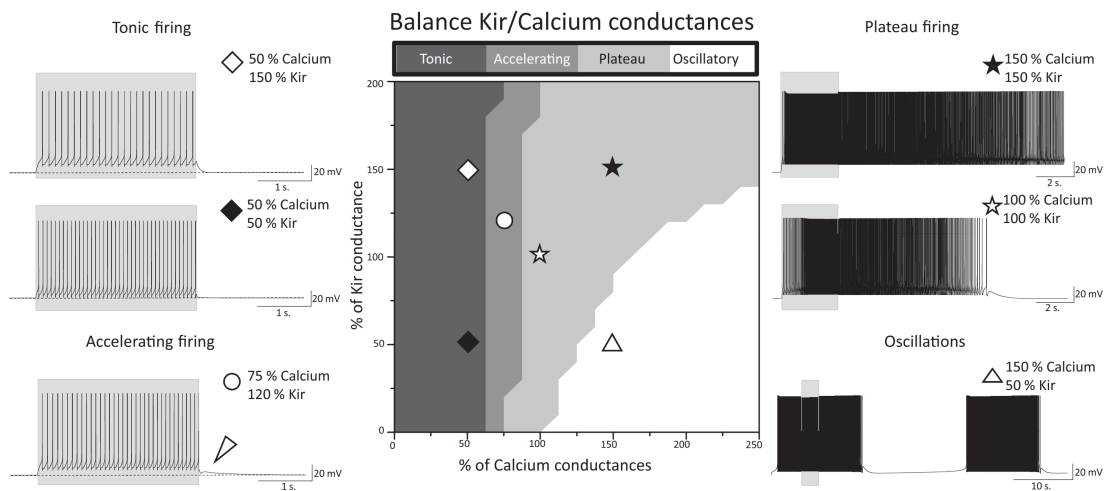
Figure 3.5.3: Firing state observed in the DHN model depending on the balance of Kir and L-type calcium channels conductances. The 4 firing modes (tonic, accelerating, plateau potentials and oscillations) described by Le Franc et al. are represented. [Franc and Masson, 2010]

as hyperpolarizing conductances. Consistently, the balance between these two groups determines if we can observe plateau potentials or not according to Figure 3.5.4. Controlling this balance means that we are able to control pain transmission properties through many possible mechanisms such as intrinsic plasticity, neuromodulation and network activity.
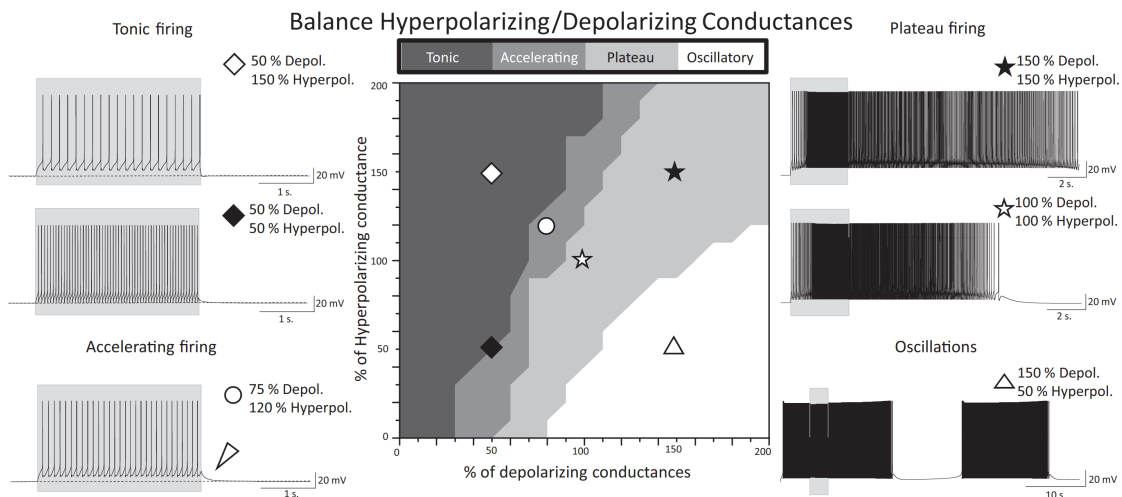

Figure 3.5.4: Firing state observed in the DHN model depending on the balance of hyperpolarizing and depolarizing conductances. The 4 firing modes (tonic, accelerating, plateau potentials and oscillations) described by Le Franc et al. are represented. [Franc and Masson, 2010]

3.5.3 Timescales and feedbacks involved in deep dorsal horn neuron functional states generation

A closer look to the activation and inactivation functions of the ion channels taken into account in Aguiar's and Le Franc's models may help to determine the timescales involved in DHNs firing properties. The Aguiar model considers a total of 6 ion currents. They are defined by 6 activation functions meaning that we must consider 6 steady-states of the activation gates and 6 time constants that are functions of either the membrane potential or the intracellular calcium potential. Beside the activation, the sodium channels modeled by Hodgkin-Huxley and the sodium channels associated to the persistent sodium are subjected to inactivation. These 2 inactivation functions add two steady-states and two time constants function of the membrane potential to look at. In Figures 3.5.5 and 3.5.6, the steady-states of the activation and inactivation gates and their time constants are respectively represented as function of their modulator (the membrane potential or the calcium concentration, depending on the channels properties).

Figure 3.5.5: Evolution of the Aguiar's model ion currents activation/inactivation variables at rest according to the membrane potential (left) or the intracellular calcium concentration (right).

The evolution of the time constant is a good start to determine the timescale of each channel kinetic and thus to group the currents of the channels considered. In the Aguiar model, considering that the different mechanisms act on 3 distinct timescales seems to be a fair enough estimation. These timescales are: fast, slow and super-slow.

It is clear that the currents considered do not impact the membrane potential in the same manner. The nature of the feedback induced by the opening of a given ion channel can be determined by the steady-state of each gate variable and the direction of the current. For example, we can consider the activation of sodium channels modeled by Hodgkin and Huxley. The sodium current flowing in these channels when they are open is inward, meaning that the sodium ions flow from the extracellular medium to the inside of the plasma membrane, which induces a depolarization. Moreover, for an increase in the
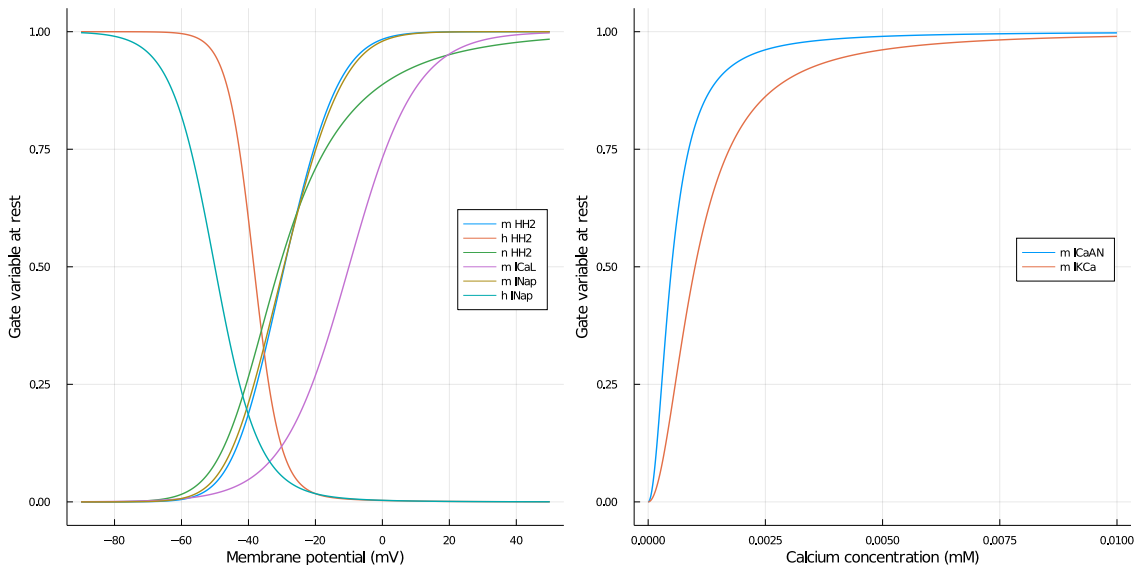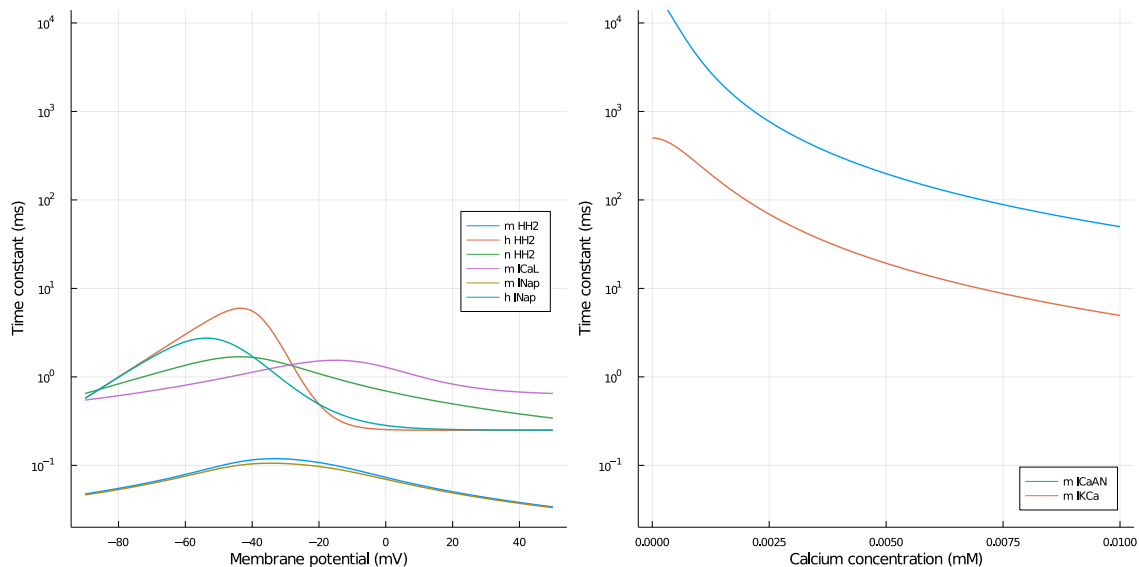
Figure 3.5.6: Evolution of time constants of the Aguiar's model ion currents activation/inactivation variables according to the membrane potential (left) or the intracellular calcium concentration (right).

membrane potential, we can see in Figure 3.5.5 that more channels tend to open. The activation of these sodium channels is thus regenerative, meaning that it creates positive feedback. Mathematically, the sign of the feedback is fixed by the sign of the resistance in the equation :

$$R = \frac{\Delta V}{\Delta I}$$

where ΔI is taken positively when outward by convention. The same reasoning can be applied to all other gates of the ion channels considered. The results of this approach for the Aguiar model are summarized in Table 3.1.

Current	Gate	Time constant order	ΔI	Δg	R	Feedback
I_{Na}	activation	10^{-1}ms	inward	+	-	Fast regenerative
	inactivation	10^0ms		-	+	Slow restorative
I_{KDR}	activation	10^0ms	outward	+	+	Slow restorative
I_{CaL}	activation	10^0ms	inward	+	-	Slow regenerative
I_{Na_p}	activation	10^{-1}ms	inward	+	-	Fast regenerative
	inactivation	10^0ms		-	+	Slow restorative
I_{CAN}	activation	10^2ms	inward	+	-	Super-slow regenerative
$I_{K,Ca}$	activation	10^1ms	outward	+	+	Slow restorative

Table 3.1: Summary of the timescale and the type of feedback involved in each ion channel activation or inactivation defined in Aguiar's model. A regenerative feedback is synonym of positive feedback while a restorative feedback induces a negative feedback. This classification is based on the order of magnitude of each time constant, on the sign of the current ΔI flowing through each type of ion channels considered and on the sign of the variation of conductance Δg with a depolarization of the cell.

Le Franc's model helps to understand the switch in the DHNs pain transmission properties. As this switch depends on a balance between hyperpolarizing and depolarizing conductances, it would be interesting to verify the feedback types of the ion channels considered in these two groups and their timescales. Compared to Aguiar's model, the model of Le Franc does not consider the persistent sodium current but uses a Kir current and a more elaborated description of the L-type calcium channels currents, segragated into slow and fast channels, with each an activation and an inactivation gate.

Figures 3.5.7 and 3.5.8 show respectively the steady-state of each gate and the associated time constants of the 7 currents considered in the model of Le Franc as functions of either the membrane potential or the calcium concentration. Following the same reasoning realized for the model of Aguiar, we classified each gate of each current depending on its timescale and the corresponding feedback produced. This classification is found in Table 3.2.

Figure 3.5.7: Evolution of the Le Franc's model ion currents activation/inactivation variables at rest according to the membrane potential (left) or the intracellular calcium concentration (right).

The activation and inactivation processes in DHNs modeled by Le Franc et al. seem to act on 4 different timescales: fast, slow, super-slow and ultra-slow. It is also worth noticing that each activation of the ion channels grouped in the depolarizing conductances in the analysis of Le Franc creates positive feedback. Similarly, the activation of the ion channels classified as depolarizing are restorative, meaning that they induce negative feedback, which is consistent.

3.5.4 Summary

The two modeling approaches presented aim to better understand the switch in the electrical behavior of DHNs. Based on activation and inactivation of the ion channels they consider, we found out that the mechanisms involved in DHNs firing pattern generation act on 4 different timescales. This time separation can be used to create a hybrid model
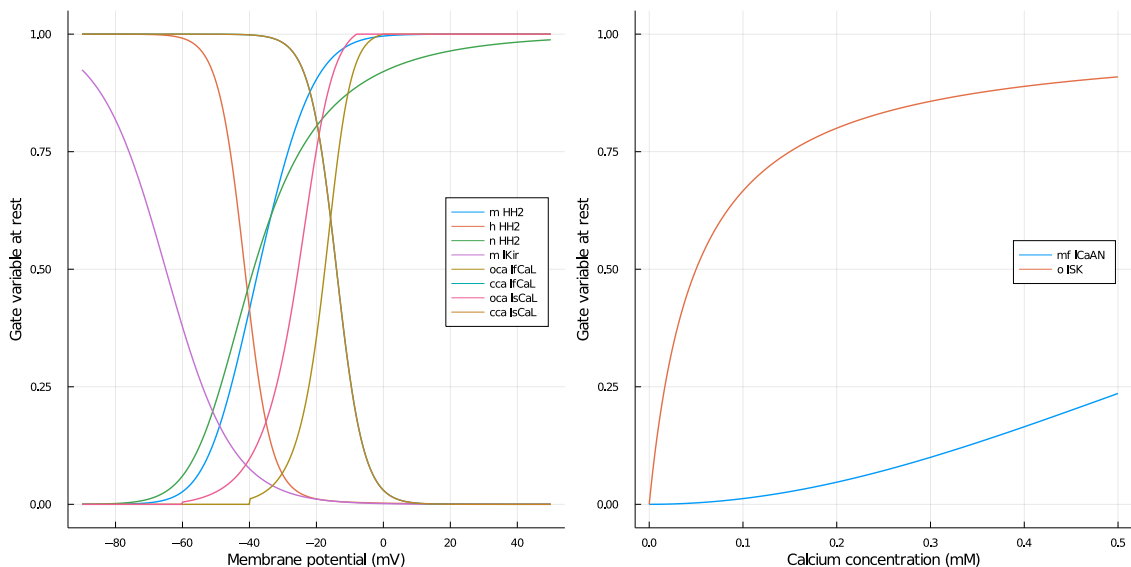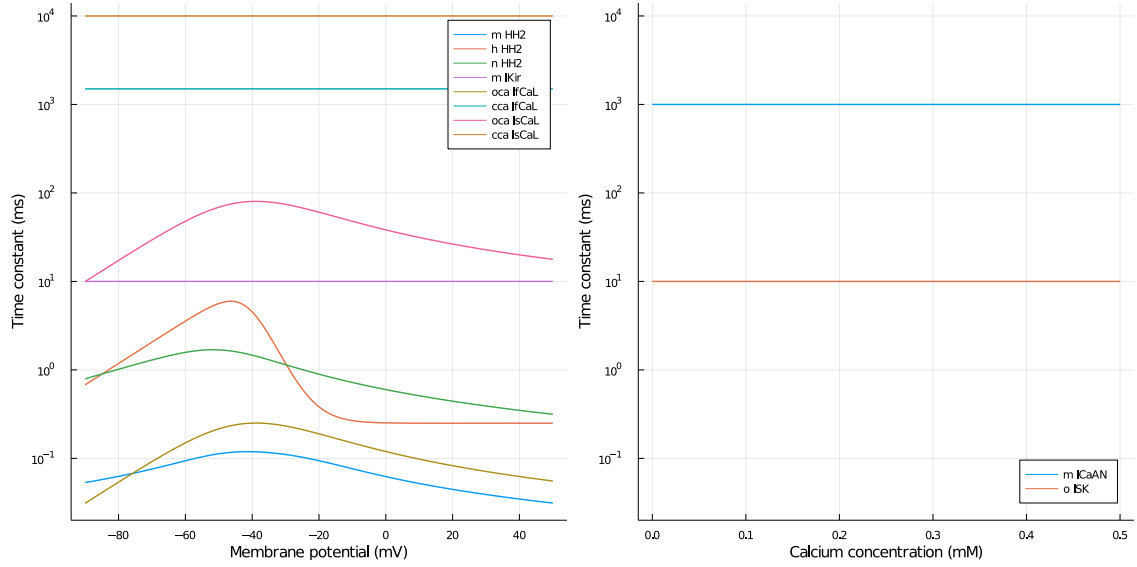
Figure 3.5.8: Evolution of time constants of the Le Franc's model ion currents activation/inactivation variables according to the membrane potential (left) or the intracellular calcium concentration (right).

Current	Gate	Time constant order	ΔI	Δg	R	Feedback
I_{Na}	activation	10^{-1}ms	inward	+	-	Fast regenerative
	inactivation	10^{0}ms		-	+	Slow restorative
I_{KDR}	activation	10^{0}ms	outward	+	+	Slow restorative
I_{Kir}	activation	10^{1}ms	inward	-	+	Slow restorative
I_{SK}	activation	10^{1}ms	outward	+	+	Slow restorative
I_{fCaL}	activation	10^{-1}ms	inward	+	-	Fast regenerative
	inactivation	10^{3}ms		-	+	Super-slow restorative
I_{CAN}	activation	10^{3}ms	inward	+	-	Super-slow regenerative
I_{sCaL}	activation	10^{2}ms	inward	+	-	Super-slow regenerative
	inactivation	10^{4}ms		-	+	Ultra-slow restorative

Table 3.2: Summary of the timescale and the type of feedback involved in each ion channel activation or inactivation defined in Le Franc's model. A regenerative feedback is synonym of positive feedback while a restorative feedback induces a negative feedback. This classification is based on the order of magnitude of each time constant, on the sign of the current ΔI flowing through each type of ion channels considered and on the sign of the variation of conductance Δg with a depolarization of the cell.

that would model DHNs. More specifically, this work focuses on a MQIF model with 4 different timescales, following an incremental procedure. The goal of using such a model is to define an input/output relation that would help us to understand how a change in conductance at a given timescale impacts the DHNs pain transmission properties.

Chapter 4

Tonic spiking generation with fast and slow timescales

In this chapter, our goal is to study the behaviour and the characteristics of the two dimensional Multiple Quadratic Integrate and Fire (MQIF) model introduced in section 2.2.2.

Contributions   Our goal is to show that the MQIF model is suited to model tonic firing. In Van Pottelbergh et al., several patterns of applied current were used to show specific properties such as afterdepolarization potential, spike latency, or bistability. However, there is no comparison between the behaviors of models with a slow restorative or a slow regenerative feedback realized with the same inputs, nor a study of the impact of the parameters. Such comparisons are realized in this work for several patterns of current. To understand how the responses associated to slow restorative or regenerative feedbacks differ, we also investigate the impact of the type of slow feedback on the phase plane. As the nullclines expression can be found based on the model equations, we compute them and their derivatives to understand their shape and the influence of each parameter on it. The impact of the applied current on these nullclines is investigated with a bifurcation diagram. Finally, the impact of the slow parameters on the convergence of the model is analyzed, leading to different types of excitability.

4.1   Model

The MQIF model is made of two timescales: a fast one and a slow one. The system of ordinary differential equations that is used in this section is the following:

$$C\dot{V} = \bar{g}_f(V - V^0)^2 - \bar{g}_s(V_s - V_s^0)^2 + I_{\text{app}} \qquad \text{if } V \geq V_{\text{max}}, \text{ then}$$
$$\tau_s \dot{V}_s = V - V_s \qquad\qquad\qquad\qquad V \leftarrow V_r, \qquad\qquad (4.1.1)$$
$$V_s \leftarrow V_{s,r}.$$

In equations (4.1.1), V and V_s are the cell potential and the slow potential respectively. The slow voltage is characterized by the time constant τ_s, which is equal to $10\,\text{ms}$ throughout this work. This value is chosen based on the appendix of the article this model is extracted from.[Pottelbergh et al., 2018] It is noticeable that this time constant is consistent with the order of magnitude of the slow feedbacks defined in section 3.5.3. For a fast-slow timescale separation, it is assumed that the membrane capacity is much lower than τ_s. The fast inward current is characterized by the fast conductance $\bar{g}_f$ and by the

equilibrium potential V^0. The slow outward current is characterized by the slow conductance $\bar{g}_s$ and by the equilibrium potential V_s^0. To keep the necessary physical meaning of the results we have with this model, it is stated that the reset position $(V_r, V_{s,r})$ should be located somewhere above the nullcline of the variable V. Once the reset applied, the system evolves according to the computation of each gradient.

It is worth noticing that the system gradient $(\frac{\delta V}{\delta t}; \frac{\delta V_s}{\delta t})$ is composed of gradients of different magnitudes. Indeed, as the time constant τ_s makes the variable V_s slow with respect to V, the direction of the system gradient is mostly set by the $\frac{\delta V}{\delta t}$ except in the near vicinity of the V nullcline.

4.2 Fixed points and nullclines

From the system provided in (4.1.1), we can get the nullclines equation. Indeed, each nullcline corresponds to a null gradient of the corresponding state variable. Here, these two variables are V and V_s. The nullclines equations are obtained by setting separately each gradient to 0:

$$
\begin{aligned}
V \text{ nullcline:} \quad & 0 = \bar{g}_f(V - V^0)^2 - \bar{g}_s(V_s - V_s^0)^2 + I_{\text{app}}, \\
V_s \text{ nullcline:} \quad & 0 = V - V_s.
\end{aligned}
\tag{4.2.1}
$$

We can rewrite the nullclines equations to plot them in the space $(V; V_s)$. The V_s nullcline is simply a straight line where V_s equals V. The V nullcline has a more complex shape. The expression of this nullcline depends on the sign of the current I_{app}. Indeed, the V nullcline can be rewritten as:

$$
V_s = V_s^0 \pm \sqrt{\frac{\bar{g}_f(V - V^0)^2 + I_{\text{app}}}{\bar{g}_s}}, \qquad \text{if } I_{\text{app}} \geq 0,
$$

$$
V = V^0 \pm \sqrt{\frac{\bar{g}_s(V_s - V_s^0)^2 - I_{\text{app}}}{\bar{g}_f}}, \qquad \text{if } I_{\text{app}} \leq 0.
$$

For each current value, the V nullcline expression leaves us with two possible solutions: either adding the square root term or subtracting it. When the current equals 0, these two expressions are similar. Indeed, the V nullcline is cross-shaped, made of two straight lines with opposite slopes and crossing in $(V; V_s) = (V^0; V_s^0)$ when I_{app} is null. Some clues about the V nullcline shape for a non-zero current can be obtained by computing the first and the second derivatives of these functions with respect to the variable they are functions of in the space $(V; V_s)$ or $(V_s; V)$:

$$
\frac{\delta V_s}{\delta V} = \pm \sqrt{\frac{\bar{g}_f}{\bar{g}_s}} \frac{V - V^0}{\sqrt{(V - V^0)^2 + \frac{I_{\text{app}}}{\bar{g}_f}}} \qquad \text{if } I_{\text{app}} \geq 0,
$$

$$
\frac{\delta V}{\delta V_s} = \pm \sqrt{\frac{\bar{g}_s}{\bar{g}_f}} \frac{V_s - V_s^0}{\sqrt{(V_s - V_s^0)^2 - \frac{I_{\text{app}}}{\bar{g}_s}}} \qquad \text{if } I_{\text{app}} \leq 0.
$$

In the first derivative expressions, we see that if the current is non-zero, the nullcline has 2 extrema. When the current is positive, the extrema in the space $(V; V_s)$ take place at the locations $(V^0; V_s^0 \pm \sqrt{\frac{I_{\text{app}}}{\bar{g}_s}})$. When the current is negative, the extrema in the space $(V; V_s)$ take place on the axis $V_s = V_s^0$. Consistently, we see that the derivative does not exist in $(V^0; V_s^0)$ when I_{app} is 0.

If we take a look at the second derivative expressions, being:

$$\frac{\delta^2 V_s}{\delta V^2} = \pm \left[\sqrt{\frac{\bar{g}_f}{\bar{g}_s}} \left(\frac{\frac{I_{\text{app}}}{\bar{g}_f}}{\left(\sqrt{(V - V^0)^2 + \frac{I_{\text{app}}}{\bar{g}_f}} \right)^3} \right) \right], \qquad \text{if } I_{\text{app}} \geq 0,$$

$$\frac{\delta^2 V}{\delta V_s^2} = \pm \left[\sqrt{\frac{\bar{g}_s}{\bar{g}_f}} \left(\frac{-\frac{I_{\text{app}}}{\bar{g}_s}}{\left(\sqrt{(V_s - V_s^0)^2 - \frac{I_{\text{app}}}{\bar{g}_s}} \right)^3} \right) \right], \qquad \text{if } I_{\text{app}} \leq 0,$$

we can see that for a non-zero current, the second derivative is either always positive or always negative. Therefore, the extrema we have on the axis $V = V^0$ or $V_s = V_s^0$ are a minimum and a maximum. Moreover, the V nullcline expression for $I_{\text{app}} < 0$ has the same shape as the expression we have when $I_{\text{app}} > 0$. Based on these considerations, we argue that the V nullcline is composed of two arms in the space $(V; V_s)$ that look like quadratic functions when the current is positive. For $I_{\text{app}} > 0$, the upper arm is convex and above the line $V_s = V_s^0$ and the lower one is concave and below $V_s = V_s^0$. When the current is negative, we have still two arms with the same shape in the space $(V_s; V)$. But if we analyze the phase plane in the space $(V; V_s)$, one arm of the V nullcline is on the left of the axis $V = V^0$ and the other one is on the right of $V = V^0$, with the extrema on the line $V_s = V_s^0$. The plot of the V and V_s nullclines is represented after the computation of the fixed points in the next subsection.

From the nullclines equations (4.2.1), we can compute the fixed points coordinates. Fixed points are defined as points where the gradient is null and are thus located at the intersections of the nullclines. The V_s nullcline implies that the fixed points coordinates have the same value for V and V_s. The fixed points coordinates, being identical due to the expression of the V_s nullcline, will be noted $\bar{V}$. By substitution, we find the following second order equation in $\bar{V}$:

$$(\bar{g}_f - \bar{g}_s)\bar{V}^2 - 2(\bar{g}_f V^0 - \bar{g}_s V_s^0)\bar{V} + \bar{g}_f \left(V^0 \right)^2 - \bar{g}_s \left(V_s^0 \right)^2 + I = 0.$$

Using the discriminant method, we find that there are at most two fixed points with the coordinates $(\bar{V}_1; \bar{V}_{s1})$ and $(\bar{V}_2; \bar{V}_{s2})$. These fixed points existence is determined by the value of the discriminant Δ:

$$\bar{V}_{s1,2} = \bar{V}_{1,2} = \frac{\bar{g}_f V^0 - \bar{g}_s V_s^0 \pm \sqrt{\Delta}}{\bar{g}_f - \bar{g}_s} \quad \text{with} \quad \Delta = \bar{g}_f \bar{g}_s (V^0 - V_s^0)^2 - (\bar{g}_f - \bar{g}_s)I. \quad (4.2.2)$$

The sign of Δ, which is function of the conductances $\bar{g}_f$ and $\bar{g}_s$, the equilibrium potentials V^0 and V_s^0 and the current I_{app}, has an impact on the system stability. The existence of fixed points based on the value taken by Δ is studied in section 4.4.

With the two fixed points coordinates, we can compute the Jacobian matrix of the system to determine the stability of each fixed point. As a reminder, the Jacobian matrix is obtained by deriving each time derivative of the system with respect to one of the two variables. In our case, these two variables are either V or V_s and this matrix is written as:

$$J = \begin{pmatrix} \frac{\delta}{\delta V} \left(\dot{V} \right) & \frac{\delta}{\delta V_s} \left(\dot{V} \right) \\ \frac{\delta}{\delta V} \left(\dot{V}_s \right) & \frac{\delta}{\delta V_s} \left(\dot{V}_s \right) \end{pmatrix}.$$

From there, we can calculate the analytical expression of the Jacobian matrix:

$$J = \begin{pmatrix} \dfrac{2}{C}\bar{g}_f(V - V^0) & -\dfrac{2}{C}\bar{g}_s(V_s - V_s^0) \\ 1 & -1 \end{pmatrix}.$$

To compute the fixed points stability, we should substitute each fixed point coordinates into the Jacobian matrix. Then, the considered fixed point stability is determined by the sign of the eigenvalues of the corresponding Jacobian matrix.

4.3 Phase plane, reference simulations and slow feedback nature

Through phase planes, phase portraits and simulations, this section aims to distinguish the properties induced by slow restorative and slow regenerative feedbacks. The same parameters are kept all along this subsection except the parameter V_s^0, which takes values of -45 or -35 to simulate respectively a restorative or a regenerative slow feedback (with V^0 being -40). However, the parameter I_{app} is modified to observe the nullclines motion in the phase plane and to perturb the system and observe its response.

4.3.1 Phase plane description

In consistency with the nullclines analytical expressions written in (4.2.1), we can see in Figure 4.3.1 the phase plane of the MQIF for 3 values of current I_{app} and 2 values of the equilibrium potential V_s^0. Each phase plane is indeed composed of a straight line and 2 quadratic-like functions (or two straight lines depending on the absolute value of the current), as discussed in section 4.2. The conductances $\bar{g}_f$ and $\bar{g}_s$ used to draw these phase planes are respectively set to 1 and 0.5. According to equations (4.2.1), these conductances have an impact on the V nullcline only. The values chosen for these constants are based on [Pottelbergh et al., 2018]. These conductances allow to scale the impact of the slow feedback on the neuron electrical response with respect to the impact of the fast feedback.

In each of these phase planes, a marker is positioned at the intersection of the 2 straight lines associated to the V nullcline for a zero current i.e. in $(V^0; V_s^0)$. It is to be noted that when the absolute value of the current increases, the nullcline extrema tend to move away from this marker. This is consistent with the conclusions we draw from the analytical expression of the V nullcline and its first and second derivatives. This marker will also be used to understand the effect of V_s^0 on the phase plane and the system firing properties in the next subsections.

For the particular values of current chosen for Figure 4.3.1, we see that we have each time two fixed points, two being the maximum number of fixed points the system can have as discussed in section 4.2. In these cases, the fixed points are always a stable node and a saddle node. By definition, a saddle node is neither stable or unstable, it is characterized by an attractive direction and a repulsive one. Typically, a system evolving near a saddle node tends to be attracted and then repelled towards another possible attractor such as a stable node or a limit cycle. Therefore, saddle nodes are often considered to separate the basin of attraction of distinct attractors and are very useful to understand spike generation.
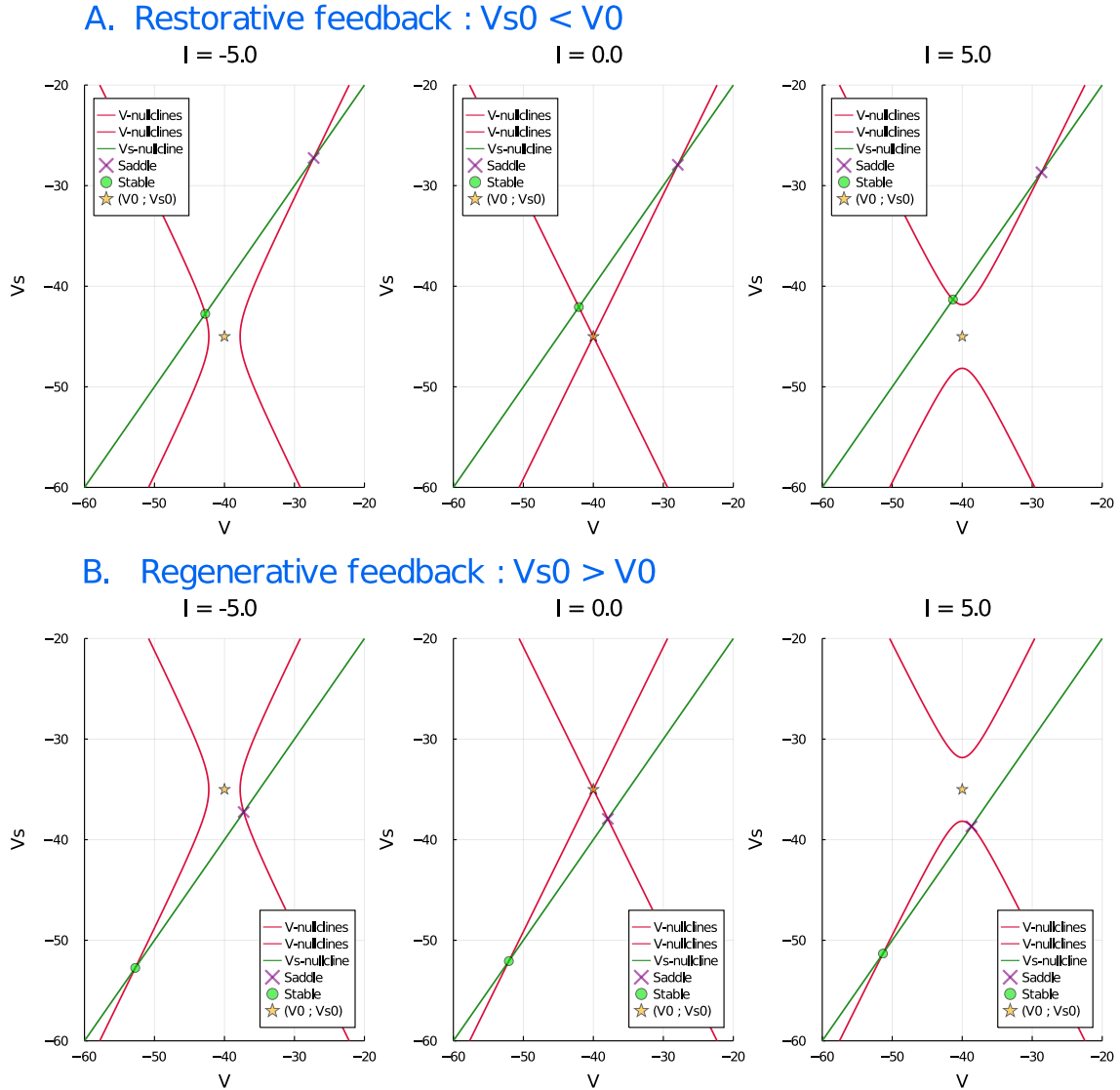
Figure 4.3.1: Phase planes of the MQIF for different sets of parameters. The V nullcline is red and the V_s nullcline is green. The yellow marker highlights the point $(V^0; V_s^0)$. A. The reference potential of the slow feedback is lower than the fast reference potential (restorative feedback). B. The reference potential of the slow feedback is greater than the fast reference potential (regenerative feedback). For A. and B., three values of current are tested to observe the movement of the V nullcline with and increasing current.

A last consideration should be realized on the sign of the gradient of each variable near the nullclines. Indeed, this is a manner to get clues about the time evolution of the system for any initial conditions. The sign of the V_s gradient is positive when the system is located anywhere below the V_s nullcline and negative when the system is above it. Therefore, the V_s nullcline is considered as attractive. In the same manner, the gradient of V is negative when, for a given V_s, the system is located between two parts of the upper arm or the two parts of the lower arm of the V nullcline. Conversely, the gradient of V is positive when the system has only one or no neighboring part of the V nullcline on the horizontal axis where the system is. Therefore the left part(s) of the V nullcline is(are) attractive and the right part(s) of the V nullcline is(are) repulsive. Due to the reset rule, the system is still

35

able to converge even if it is initialized to the right of the V nullcline as the reset value $(V_r, V_{s,r})$ is above the V nullcline. Furthermore, these observations allow us to understand that the system is not excitable if the current is negative. Indeed, the system is attracted to the left part of the V nullcline and therefore to the stable node on it.

4.3.2 Slow feedback nature impact on phase plane

The relative position of the marker of $(V^0; V_s^0)$ with respect to the straight line associated to the V_s nullcline has an impact on the system stability. Indeed, if the marker is below the V_s nullcline ($V^0 > V_s^0$), the fixed points appear on the top part of the V nullcline. Conversely, the fixed points appear on the bottom part of the V nullcline if the marker is above the V_s nullcline ($V^0 < V_s^0$). This distinction impacts the system convergence. To discuss the convergence based on the fixed points position on the nullclines, we added trajectories with a total of three sets of initial conditions to the phase planes obtained with a positive current from Figure 4.3.1. In Figure 4.3.2, we show the phase plane obtained for a positive current and $V_s^0 < V^0$ with the corresponding time evolution of the system. In Figure 4.3.3 we show two phase planes obtained for a positive current and $V_s^0 > V^0$, each with a different set of initial conditions and the corresponding system time evolution.
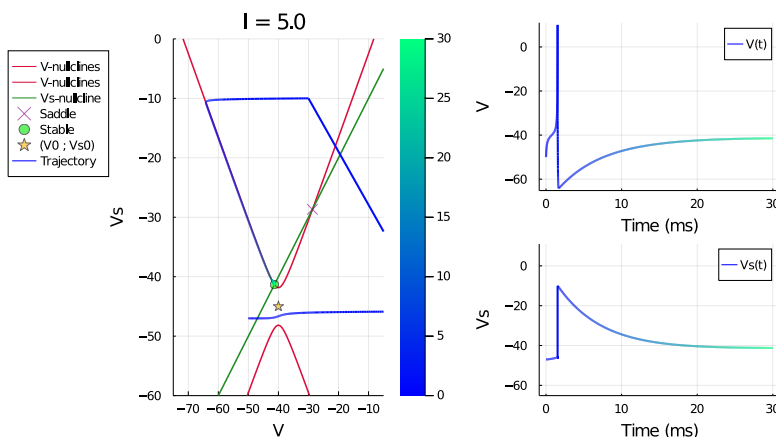

Figure 4.3.2: Trajectory in the phase portrait (left) and the associated time evolution of V and V_s (right) of a restorative system for a positive applied current ($V^0 > V_s^0$).

As we said, the difference in the V nullcline position, which is defined by the position of the corresponding marker, and the number of fixed points impact the system convergence. Indeed, when two fixed points are on the upper part of the V nullcline (i.e. $V_s^0 < V^0$) and when the system is excited (i.e. $I_{app} > 0$), the system is drawn to the upper left part of the V nullcline from any initial conditions and converges towards the stable node. Accordingly, the time evolution of the system highlights that the system converges towards a steady-state. It means that if the system is initially excited, a low positive current is not sufficient for the neuron to show tonic spiking. There is a restorative feedback and it is associated to a positive conductance in the neuronal model.

When the fixed points are on the lower part of the V nullcline (i.e. $V_s^0 > V^0$) and when the system is excited (i.e. $I_{app} > 0$), the system is bistable. In this case, the saddle node separates two basins of attraction: the basin of the stable node and the basin of a possible limit cycle. Thus, the system can converge towards one of these two attractors. Indeed,
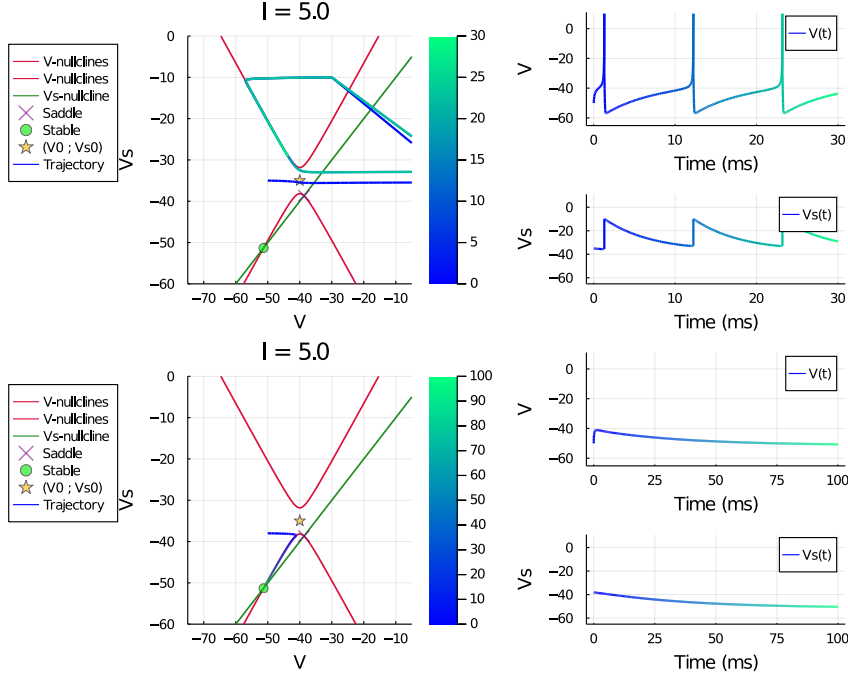
Figure 4.3.3: Trajectories in the phase portrait (left) and the associated time evolutions of V and V_s (right) for two distinct sets of initial conditions of a regenerative system with a positive applied current ($V^0 < V_s^0$).

when the current is sufficient, the gradient is high in the bottleneck bounded by the V nullcline extrema. Therefore, the system cannot reach the attractive lower left part of the V nullcline when initialized outside the basin of attraction of the stable node (see Figure 4.3.3, top). Consequently, the system gradient is governed mostly by the $\frac{\delta V}{\delta t}$ component and pulls the system to the reset point. Thus, the system always stays outside the basin of attraction of the stable node and describes a limit cycle. However, for a low positive current and a set of initial conditions located in the basin of attraction of the stable node, the system converges towards the stable node (see Figure 4.3.3, bottom). In other words, the system is able to evolve towards a resting state or to show tonic spiking. There is a regenerative feedback and it is associated to a negative conductance in the neuronal model.

Provided that the equilibrium potential of the fast timescale V^0 is fixed and that the V_s nullcline is a straight line where $V_s = V$, the relative value of V_s^0 with respect to V^0 will define if the fixed points are either in the top part or in the bottom part of the V nullcline. Therefore, the equilibrium potential V_s^0 has the physiological interpretation of the balance between slow restorative and slow regenerative ion channels.

4.3.3   Response to stimulation patterns and firing properties

As we said, the balance between slow restorative and slow regenerative ion channels offered by the parameter V_s^0 impacts the stability. Therefore, this balance has also an impact on the excitability properties of the system. To illustrate these properties, we simulated various patterns of the current I_{app} through time. We have then studied the excitability properties illustrated by the system response to these simulations. Unlike in the phase planes shown in Figure 4.3.1, we used a high value of the current I_{app} to excite

the system. According to section 4.2, the reader should bare in mind that increasing the absolute value of the current will move the V nullcline extrema away from its straight lines intersection in $(V^0; V_s^0)$ when the current is null. Therefore, for a high positive current value, the V nullclines extrema are relatively away from the V_s nullcline and there are no more fixed points in the system. This assumption is true for both values of V_s^0 used to simulate respectively a slow restorative and a slow regenerative feedback. The parameters of these two models are chosen to be each equal. However, the parameter V_s^0 is, as before, set to -45 or -35 in order to simulate each model respectively with a restorative or a regenerative slow feedback, with a V^0 of -40.
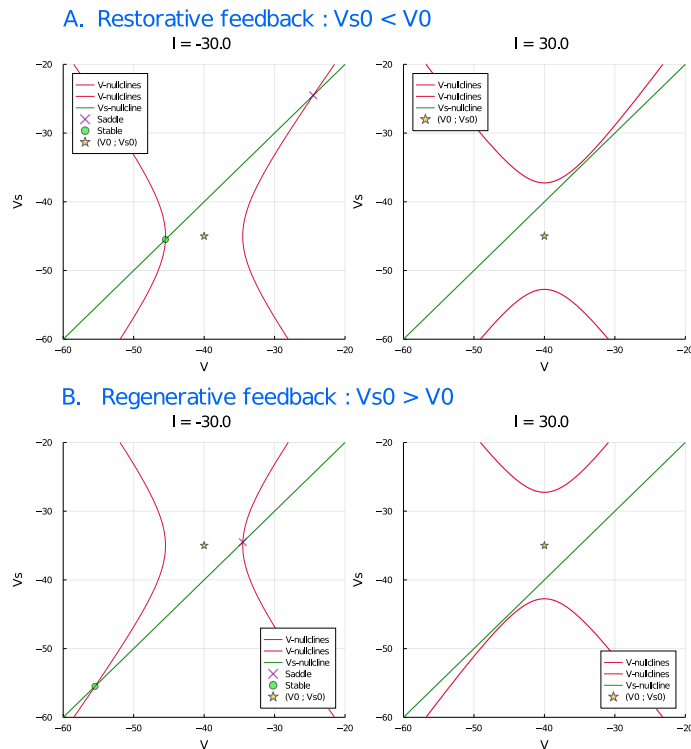

Figure 4.3.4: Phase planes of a restorative slow system (A.) and of a regenerative slow system (B.) for a large negative (left) and positive (right) value of the applied current.

Long-time pulse Studying a step of current as input of the system can help to understand the properties involved in tonic spiking. To do so, we simulated a 0 current with initial conditions near the resting state of the two systems obtained respectively for a restorative slow feedback and a regenerative slow feedback. The results of these two simulations are shown in Figure 4.3.5. After 150 ms, we suddenly increased the current to 30. This value is chosen so that there is no fixed point anymore and the only attractors in these systems are stable limit cycles. This current is maintained during 200 ms. Finally, the current is set back to its initial value.

The time responses of the systems having a slow restorative feedback or a slow regenerative feedback are different. The system built with a slow restorative feedback reaches its stable equilibrium when the current is low. When the current is very high, the system spikes directly with a constant frequency and describes a stable limit cycle. To contrast, the system built with a slow regenerative feedback shows particular excitability properties
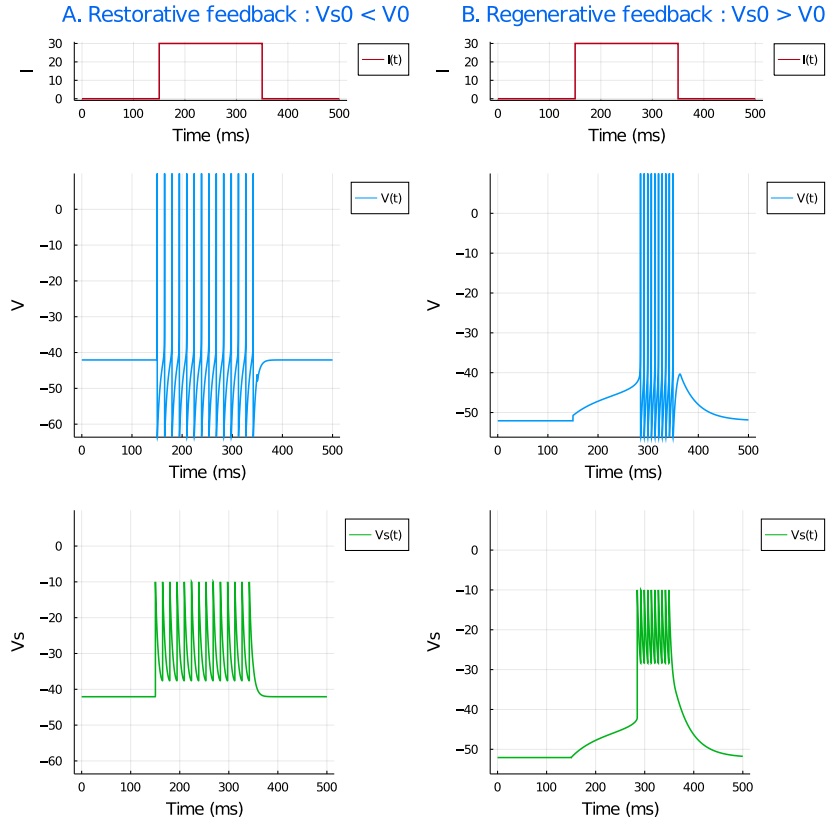
Figure 4.3.5: Time responses of the restorative slow system (A.) and the regenerative slow system (B.) for the same pulse of current. The red lines are the simulations of the applied current. The blue lines are the cell potentials for each system. The green lines are the slow potential for each system.

such as spike latency and the presence of afterdepolarization potential. Spike latency is the variable latency preceding the first action potential produced in response to a current stimulus. Indeed here, the highest value of the step of current is high and there is no stable equilibrium in the system for the chosen parameters. Therefore, the only explanation for the fact that the system does not spike as soon as the current is increased is that the system needs more time to produce the first action potential and to reach the stable limit cycle. The afterdepolarization potential is the distinct depolarization immediately following a spike (or a train of spikes) with a low amplitude. As for the restorative system, the regenerative system converges towards a limit cycle too when the current is high provided that the pulse duration is long enough.

The last difference that can be seen in Figure 4.3.5 is related to the stable limit cycle of the two systems. We can see that the cycle frequency seems lower when the slow feedback is restorative. Moreover, we see that the limit cycle minima are different for these two systems. Indeed, as the V nullcline position depends on the equilibrium potential V_s^0 (which defines the slow feedback type), the V nuclline minimum is not at the same place in the phase plane for these two models. From the position of the reset state in the phase plane, the system is attracted to the upper left part of the V nullcline and slides down on it until it reaches its minimum, where the system is actually between the attractive part and the repulsive part of the nullcline. Then, the system spikes again. For the regenerative

system, the minimum of the upper arm of the V nullcline is higher than the V nullcline minimum of the restorative system. Therefore, the regenerative system reaches the V nullcline minimum sooner. This explains why the frequency of the tonic spiking produced by the regenerative slow feedback is higher. When the cell potential is higher that V_{max}, the reset rule is applied. The two limit cycles shown in Figure 4.3.5 have thus the same maxima.
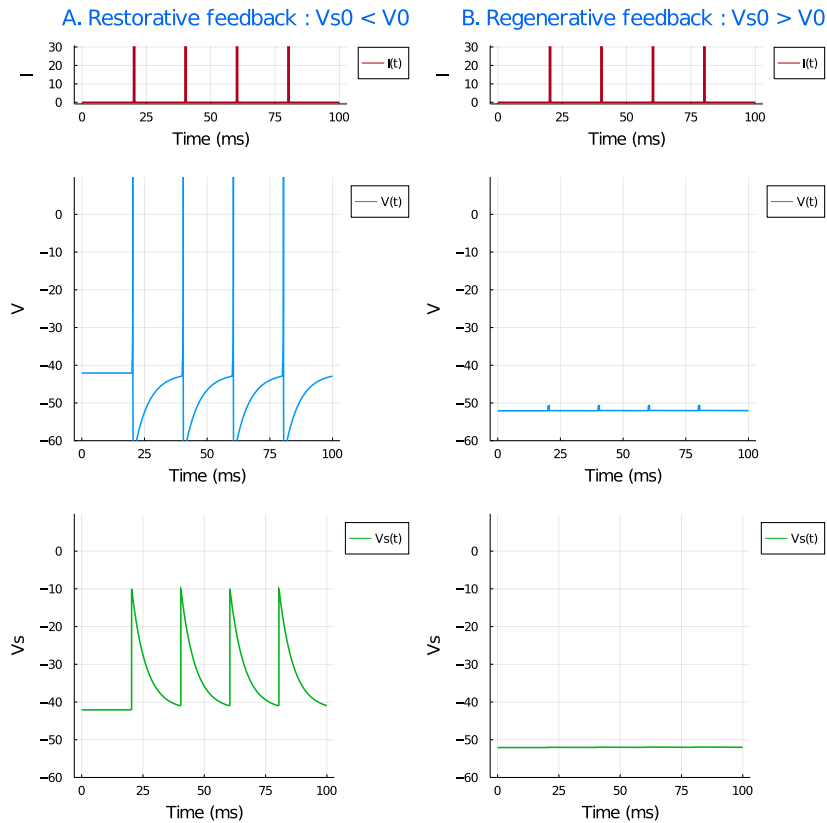

Figure 4.3.6: Time responses of the restorative slow system (A.) and the regenerative slow system (B.) for short pulses of current. The red lines are the simulations of the applied current. The blue lines are the cell potentials for each system. The green lines are the slow potentials for each system.

Short-time pulses   In figure 4.3.6, we study the responses to short-time pulses of current of the same two systems respectively made of a slow restorative and a slow regenerative feedback. As for the previous simulation, the current takes two possible values: 0 or 30. Consistently with the responses obtained for a long-time pulse shown in Figure 4.3.5 and the observations we made here above, we see that the behavior of these two systems is very different for this type of simulation. Indeed, the system built with a slow restorative feedback delivers an action potential as soon as the current changes. Once the pulse disappears, the only attractor left in the phase plane is a stable node. Therefore, the model with a restorative slow feedback slowly reaches rest until the next stimulation. To contrast, exciting the regenerative system in a punctual way is not sufficient to get the system out of the basin of attraction of the stable resting state. This observation is directly linked to the spike latency property that is clearly shown in Figure 4.3.5. Indeed, the range of time in which the current is high is too small here. Thus, the convergence of the system is set

by the value of the baseline of the current applied when there is no pulse, which is equal to 0 in this case. Therefore, the system converges towards a stable equilibrium when the feedback is regenerative.
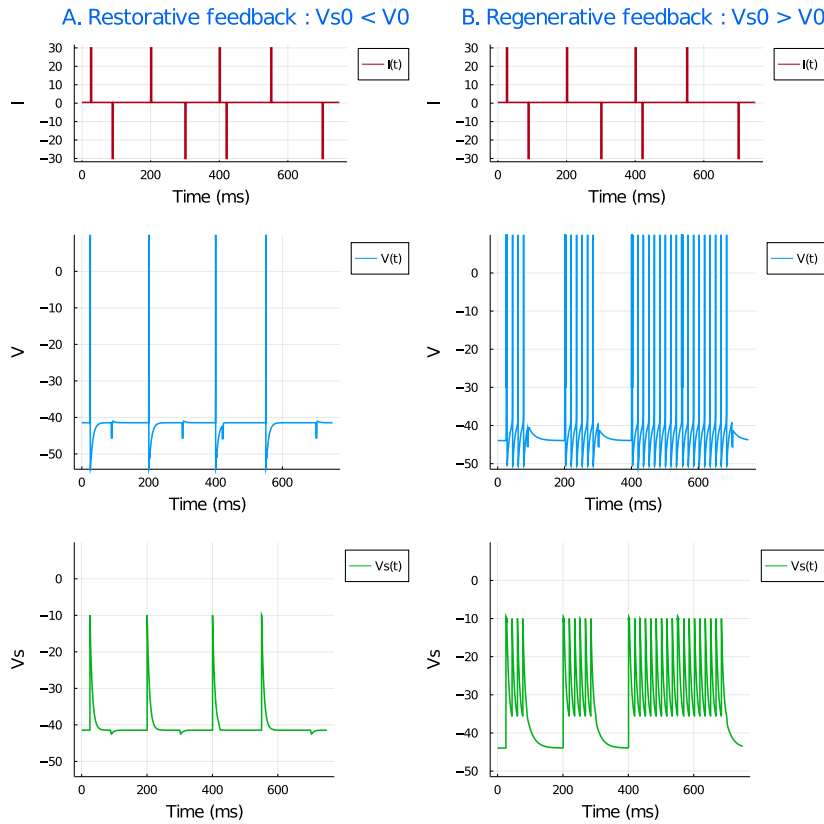

Figure 4.3.7: Time responses of the restorative slow system (A.) and the regenerative slow system (B.) for the same pattern of current. This pattern of current contains each time a positive pulse followed later by a negative one. The red lines are the simulations of the applied current. The blue lines are the cell potentials for each system. The green lines are the slow potentials for each system.

Up and down short-time pulses An interesting pattern of current to enhance the contrast between restorative and regenerative feedbacks consists in simulating a high(up) short-time pulse followed by a negative(down) short-time pulse with the same absolute value. The baseline of the current is here a little bit higher than 0. Indeed, if the value of the current is 0 or very close to it, the gradient of V between the extrema is too close to 0 and the system cannot reach the maximum value V_{max} to produce a spike and enable the reset rule. The value of the current baseline is therefore chosen to enable this spiking behavior. The highest value and the lowest value of the current are respectively 30 and -30.

If the baseline of the current is 0, no cyclic behavior is possible. As explained earlier, for a positive applied current under the threshold of approximately 0.36, the gradient of V is not sufficient for the trajectory to go between the two extrema. Thus, the cell potential cannot show a limit cycle for very low currents. In the simulation of short-time pulses in Figure 4.3.6, the slow regenerative model converged towards a stable equilibrium as the baseline is 0. Here, the current baseline is above 0 and both a cyclic behavior and a stable

41

equilibrium can be obtained. Indeed, the response of the slow regenerative model shows time frames with different lengths where the system converges towards rest and others where it converges towards a stable limit cycle. The regenerative model is thus bistable. To contrast, the model built with a slow restorative feedback always converges towards rest even if it is perturbed by up or down current pulses. Therefore, the model with restorative feedback is not bistable.

Bistability is easily observed in a phase portrait. At the beginning, the initial conditions are in the basin of attraction of the stable node, making the system converge towards the stable equilibrium. After the first positive pulse, the system is brought outside the basin of attraction of the stable equilibrium. In fact, the V nullcline extrema are brought further from the point $(V^0; V_s^0)$ and thus the V nullcline maximum is significantly lowered when the current switches from a low positive to a high value of current. While the system was on the V nullcline near the equilibrium point before the increase of current, the system finds itself between the two parts of the V nullcline during the positive pulse. The system is then drawn by its gradient to the reset and converges towards a stable limit cycle. Once a negative pulse is applied at a particular time, the system is able to return towards its stable equilibrium. Indeed, the phase plane of the model with a negative current shows a stable node on the lower left part of the V nullcline. Therefore, the system is attracted towards this stable node during the short-time negative pulse.

The sequence of a stable equilibrium followed by a stable limit cycle, itself followed by a convergence towards rest, is well observed in the right part of Figure 4.3.7, from 0 to 400 ms, for a regenerative slow feedback. From 400 to 800 ms, we simulated twice a positive pulse followed by a negative pulse after a varying time. In the model response, we see that the system does not stop spiking between the first negative pulse and the second positive one, contrasting with what we have between 0 and 400 ms. This is to highlight that the negative pulse does not always force the system to converge back towards the stable equilibrium. In fact, a certain timing is important to observe this phenomenon. Indeed, delivering a negative pulse to the system for a short-time will make the trajectory to follow the left part of V nullcline when the current is negative. As the pulse is applied during a very short amount of time, the system position in the phase portrait is essential to be able to return to the basin of attraction of the stable node.

4.4   Bifurcations study

Throughout this subsection, we study how the system stability changes with the considered parameters. Each of the considered parameters produces a bifurcation that helps to understand the model excitability properties. First, studying the bifurcation of the current helps to understand the convergence of the system. Second, studying how the equilibrium potential of the slow feedback (V_s^0) changes the system stability highlights the contrast between restorative and regenerative slow feedback. Third, studying the impact of the conductances on the system stability will help to finally characterize the different types of excitability that can be modeled.

4.4.1   Bifurcation and limit cycle frequency evolution with current

In section 4.2, we deduced analytically that modifying the current resulted in moving the V nullcline extrema and observed this phenomenon in Figures 4.3.1 and 4.3.4 from

the previous subsection. As the V_s nullcline is not influenced by any of the parameters, it is considered as fixed. Intuitively, the V_s nullcline, being a straight line, can intersect at most two times the V nullcline to create two fixed points, can be tangent to one part of the V nullcline, or may not intersect it at all. Therefore, there are always 0, 1, or 2 fixed points in the phase plane. Analytically, the number of fixed points is set by the sign of Δ, defined in equation (4.2.2). We define the bifurcation current as the current for which we have the transition from 0 to 2 fixed points, at which we have only one fixed point so. If we set Δ to 0, which analytically corresponds to only one fixed point, we can express the bifurcation current in terms of the other parameters using equation (4.2.2):

$$ I_{\text{bif}} = \frac{\bar{g}_f \bar{g}_s (V^0 - V_s^0)^2}{\bar{g}_f - \bar{g}_s} $$

Consistently with the phase planes shown in Figures 4.3.1 and 4.3.4, Δ is positive(resp. negative) when the current is lower(resp. higher) than the bifurcation current and there are therefore 2(resp. 0) fixed points in the system. This type of bifurcation is called a saddle-node bifurcation. A saddle-node bifurcation is created by two fixed points, typically a saddle and a stable/unstable node, that get closer and closer with an increase of the bifurcation parameter until they collide into one fixed point at the bifurcation point. The fixed point obtained at the bifurcation has the stability of the two fixed points that collided: in the case of a stable node that collides with a saddle, the resulting fixed point is attractive on one side and partly repulsive on the other. If the bifurcation parameter is further increased, there is no fixed point in the system anymore.

In figure 4.4.1, we show the bifurcation diagram obtained for a varying current in two models: the first is built with a restorative slow feedback and the second is built with a regenerative slow feedback. Each bifurcation diagram contains two parts: the evolution of the V coordinate with the current on the left and the evolution of the V_s coordinate on the right. The shape of the bifurcation diagram for each slow feedback type highlights that the fixed points are found respectively on the left and on the right part of the V nullcline. As the current increases, they get closer and closer to each other until they merge into one point before disappearing. The shape of this bifurcation diagram is therefore consistent with the intuition on the V nullcline movement with I_{app} and the analytical developments associated to the computation of the fixed points in section 4.2. For the parameters we chose, the bifurcation current is 25 for both models because the difference between each equilibrium potential of the slow feedback (V_s^0) and V^0 is ± 5.

If we compare the bifurcation diagrams obtained for a slow restorative and a slow regenerative feedback, we can highlight other properties of their excitability. The model built with a regenerative slow feedback shows bistability in the associated bifurcation diagram. As a matter of fact, between a value close to 0 and the bifurcation current, we find the coordinates of the stable equilibrium and the minimum and maximum values of the stable limit cycle, defined for each current in this range. The smallest current at which a stable limit cycle can be observed is not 0 but around 0.36 for the set of parameters chosen. Actually, the gradient needs to be sufficient in the bottleneck between the V nullcline extrema for the model to be able to repeatedly pull the trajectory towards the reset. It is also to be noted that the bifurcation diagram with I_{app} of V_s for the slow regenerative model clearly shows that the saddle node separates the basin of attraction of the stable node and the one of the stable limit cycle.
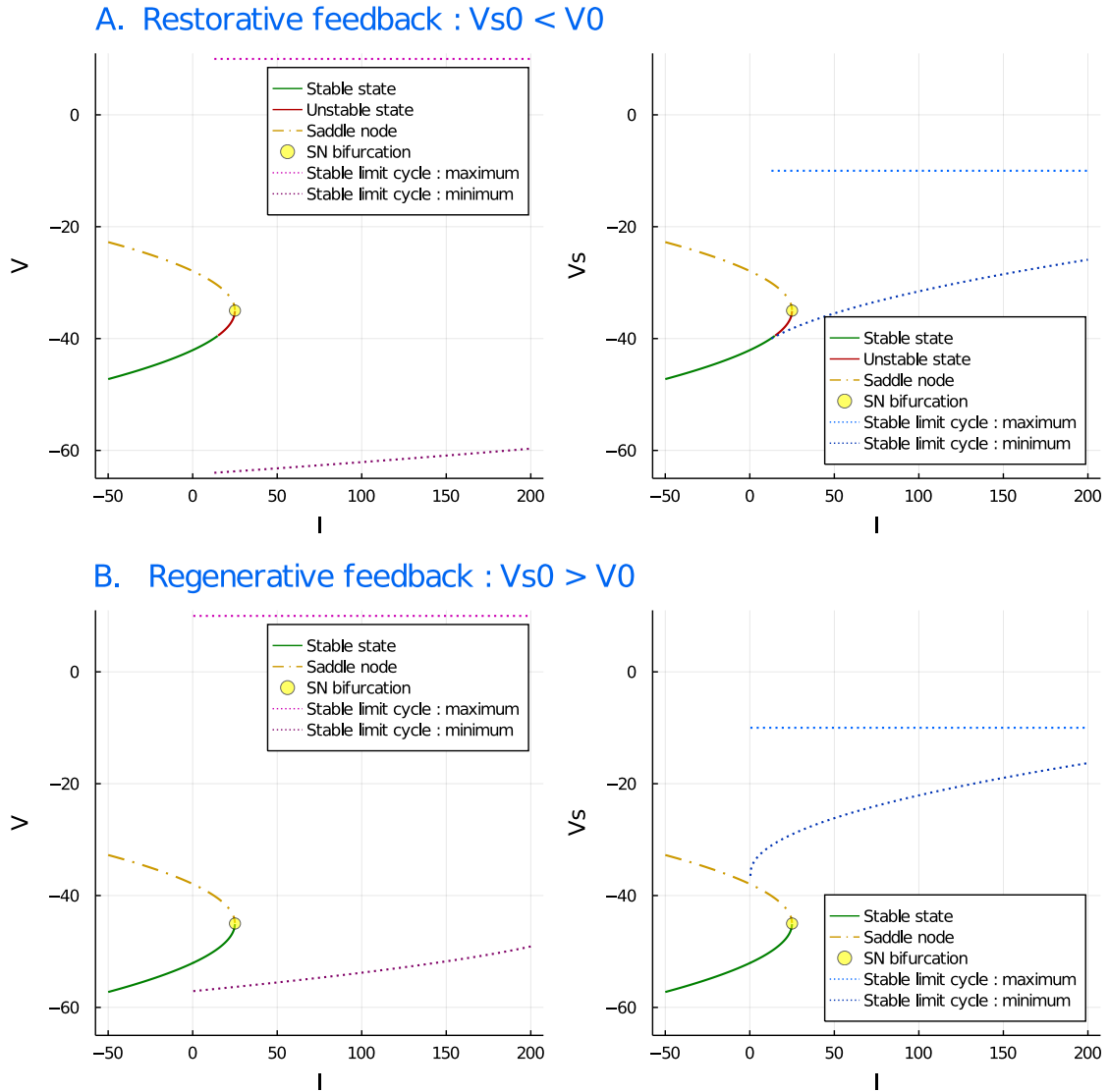
Figure 4.4.1: Bifurcation diagrams with the applied current of the system with restorative feedback (A.) and the system with regenerative feedback (B.). The V coordinate of the fixed points and the maximum and minimum of V during the limit cycle are represented on the left. The V_s coordinate of the fixed points and the maximum and minimum of V_s during the limit cycle are represented on the right.

To contrast, the model built with slow restorativity does not explicitly show bistability as there is no possible current at which we observe a cycle and a steady-state. Indeed, the cyclic behavior arises from the presence of an unstable node in the phase plane, making the system reach the reset and describe a stable limit cycle. Nevertheless, there is a very small range of current in which the stable limit cycle is reached even though a stable node exists in the system. However, bistability is very fragile in this range of values and we maintain that we cannot observe explicitly two distinct behaviors as shown in the simulation in section 4.3. Moreover, the saddle node does not properly separate the basin of attraction of the stable node and the stable cycle which makes the bistability even more fragile. In fact, the range of values where a limit cycle exists near a stable node is really close to the point where the stable node becomes unstable through a bifurcation called subcritial Hopf

bifurcation. In the restorative model, this bifurcation happens when the stable fixed point is located right where the minimum of the V nullcline takes place. At this moment, the fixed point is between the attractive (i.e. left) part and the repulsive (i.e. right) part of the V nullcline.

Finally, we see that the stable limit cycle described by the two models are different, as noticed during the analysis of Figure 4.3.5. The stable limit cycles can also be characterized by their frequency. Previously, we noticed that the limit cycle shown by the slow restorative feedback model seemed to have a lower frequency than the system with slow regenerativity for the same current. In figure 4.4.2, we draw the evolution of the limit cycle frequency with the current. Consistently, the lowest current of these two curves is not the same. Indeed, for the restorative model, the stable limit cycle exists only when the stable node looses its stability, which happens at a current higher than 0. Also, the limit cycle frequency of the slow regenerative model is significantly higher than the model with slow restorativity. Intuitively, this difference is partly explained by the difference between the maximum and minimum of the limit cycle shown in Figure 4.4.1: this difference is larger for the model with slow restorativity, meaning that the system covers a broader area of the phase plane in more or less the same time, which may decrease the stable cycle frequency. The shape of these two curves defining the evolution of the frequency is also different, probably due to second order effects.
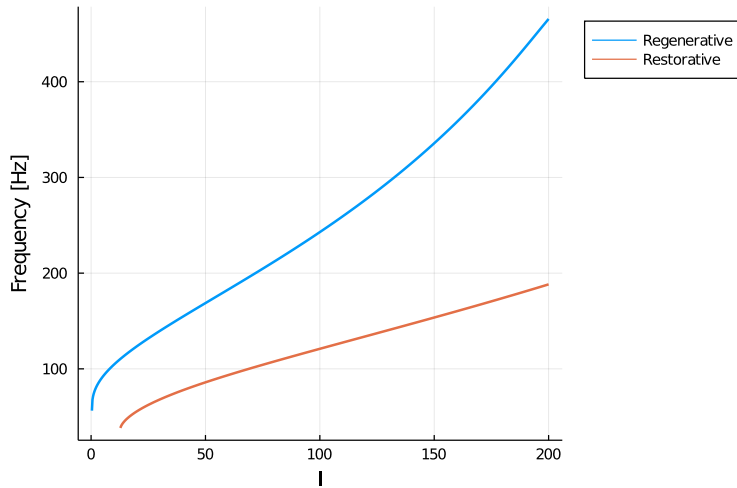

Figure 4.4.2: Evolution of the limit cycle frequency with the applied current for a regenerative and a restorative system.

4.4.2 Bifurcation with the type of slow feedback

To put into perspective the effect of the equilibrium voltage on the system stability, we can study the evolution of the fixed point coordinates and the corresponding eigenvalues of the Jacobian matrix. Once again, we will compute a bifurcation diagram, with V_s^0 as the bifurcation parameter this time. As we just showed, the current also has an impact on the system stability. To keep only one bifurcation parameter at the time, we keep only V_s^0 in a first instance and show the corresponding bifurcation diagram associated to three different values of current. These bifurcation diagrams can be found in Figures 4.4.3, 4.4.4, and 4.4.5. For each bifurcation diagram, we added 3 phase planes to have a better idea of

the impact of V_s^0 on the nullclines intersection and the corresponding fixed point stability.
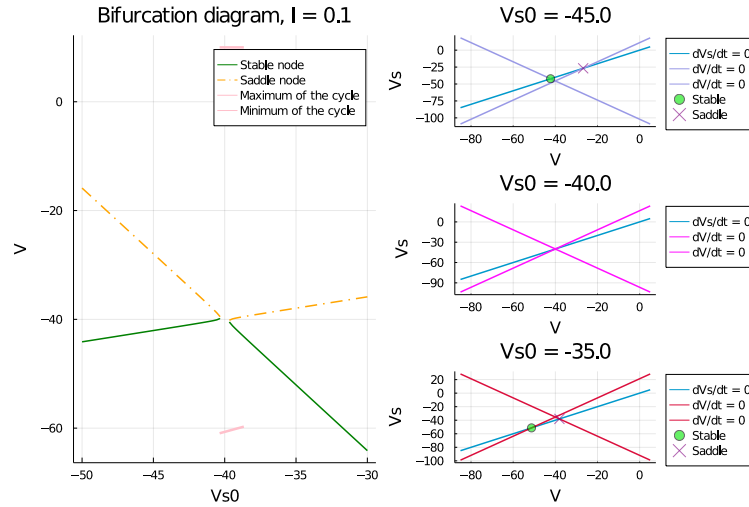

Figure 4.4.3: Bifurcation diagram with V_s^0 (left) and phase planes associated to different values of V_s^0 (right) for a low value of current.
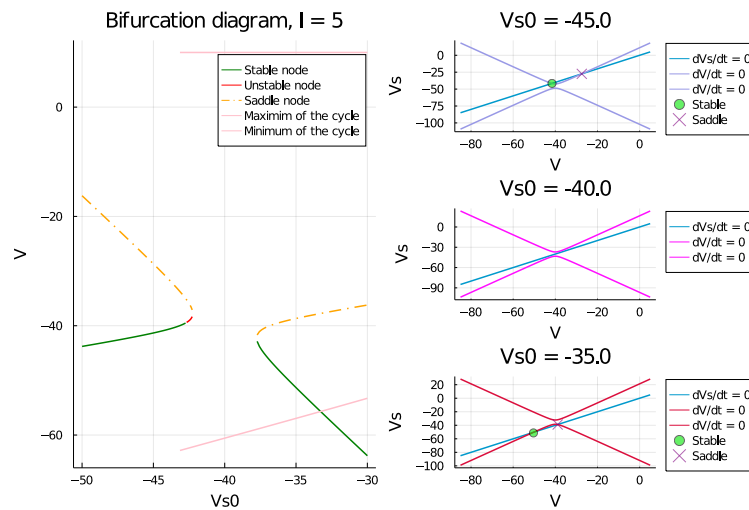

Figure 4.4.4: Bifurcation diagram with V_s^0 (left) and phase planes associated to different values of V_s^0 (right) for a middle value of current.

For a low positive applied current, the restorative and regenerative models respectively used for the previous analysis have the same number of fixed points. Indeed, as seen in Figure 4.4.3(left, upper right and lower right), the phase plane of these two models counts a saddle node and a stable node. However, if the slow reference potential V_s^0 is very close to V^0, which is equal to -40 in this section, the resulting model does not have any fixed point (Figure 4.4.3 left and middle right). In this case, the system converges towards a limit cycle. It is also to be noted that for the conductances chosen, the saddle node always appears on the right of the stable node, as the saddle coordinates are always higher.
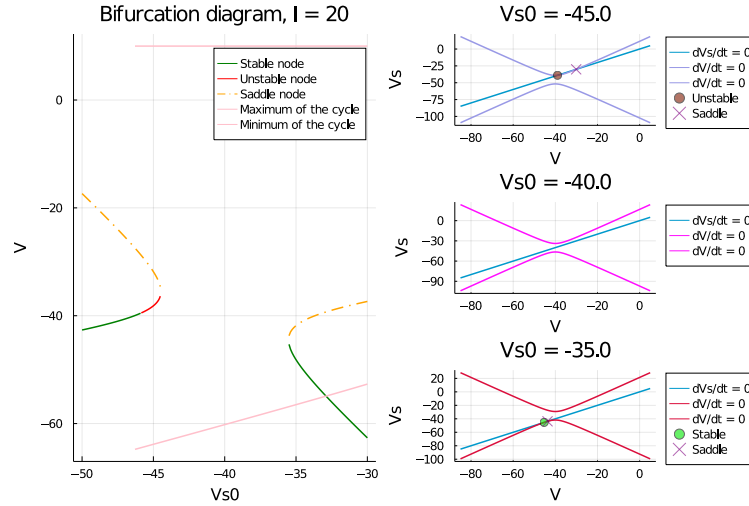
Figure 4.4.5: Bifurcation diagram with V_s^0 (left) and phase planes associated to different values of V_s^0 (right) for a high value of current.

Switching from Figure 4.4.3 to Figure 4.4.4 highlights the impact of an increase in applied current. As the impact of the current on the phase plane was already explained earlier, we can only consider the fixed points position as a function of V_s^0 in the left part of these figures. The area where there are no fixed points and in which we observe only a limit cycle is much wider when the current is increased. This phenomenon is explained by the movement of the V nullcline induced by an increase in applied current. As the distance between its extrema increases with an increasing current, the range of values for V_s^0 so that the vertical translation produced makes one of the two parts of the V nullcline touch the V_s nullcline is larger. Moreover, it can be seen that the area where a stable node coexists with a stable limit cycle is larger when the current is higher. Consistently, bistability is observed only for regenerative models. For restorative systems, the limit cycle exists thank to an unstable node, located on the repulsive arm of the V nullcline. Indeed, the extrema of the V nullcline are located on the axis $V = V^0$ and the unstable node coordinates are larger than this threshold.

A further increase in the applied current allows to switch from Figure 4.4.4 to Figure 4.4.5. If we compare the right part of these figures, we can clearly see that the distance between the V nullcline extrema is larger for a higher current and that the fixed points are closer to each other. For $V_s^0 = -45$, we can observe that the stable node becomes an unstable node for the increase in current considered. The same conclusions drawn on the comparison between Figure 4.4.3 to Figure 4.4.4 apply here. Indeed, the area in the bifurcation diagram where only a cycle is observed is also larger. Moreover, the position of the two saddle-node bifurcations are modified with the current. Only the lower left and the upper right parts of the V nullcline are candidate to be tangent to the V_s nullcline. As we explained, when the current increases, the extrema of the V nullclines are smoother and brought further from $(V^0; V_s^0)$. Therefore, the positions where the fixed points are merged into a double fixed point also tend to be brought further from $(V^0; V_s^0)$. As the location where the stable node becomes unstable for the system with slow restorative feedback is fixed, the area where an unstable node gives rise to a limit cycle is also larger.

4.4.3 Impact of the conductances

The final effect on the V nullcline is produced by a change in the conductances of the fast and slow currents. To understand their impact, it is interesting to consider that the cell voltage is far from its reference potential V^0. In this manner, the V nullcline can be approximated as:

$$V_s \approx V_s^0 \pm \sqrt{\frac{\bar{g}_f (V - V^0)^2}{\bar{g}_s}},$$

such that the effect of the applied current is negligible. Using this simplification, we can see that when the difference between the cell potential and its reference potential is large, the nullcline is globally made of two straight lines. This situation was already observed without any simplification for a zero current.

Thus, the conductances $\bar{g}_f$ and $\bar{g}_s$ scale the slope of these two straight lines. As the V_s nullcline is also a straight line with a slope of one, we can already fix three types of cases: either $\bar{g}_f$ is greater than $\bar{g}_s$, $\bar{g}_f$ is equal to $\bar{g}_s$ or $\bar{g}_f$ is lower than $\bar{g}_s$. Until now, we always considered that $\bar{g}_f$ is 1 and $\bar{g}_s$ is 0.5, which corresponds to the first case of the three. To understand how the behavior of the system, being either restorative or regenerative, is impacted by the choice of conductances, we can analyze how the saddle-node bifurcation behaves for these three cases. To do so, we take back the equation of Δ (equation 4.2.2) and equal it to 0 to obtain a double fixed point. This equation can be rewritten as the two reciprocal functions:

$$SN \equiv V^0 = V_s^0 \pm \sqrt{\frac{(\bar{g}_f - \bar{g}_s)}{\bar{g}_f \bar{g}_s} I} \quad \text{or} \quad \bar{g}_s = \frac{\bar{g}_f I}{I + \bar{g}_f (V^0 - V_s^0)^2}.$$

This function can be plot in the space $(\bar{g}_s; V^0)$ to locate the position of the saddle-node bifurcation. At first, it is helpful to consider that V_s^0 is equal to the previous value chosen for V^0, being -40. To be able to plot the function, we chose a value of the applied current slightly over 0. Figure 4.4.6 shows the horizontal position of the saddle-node bifurcation for a varying conductance $\bar{g}_s$ and a fixed conductance $\bar{g}_f$ of 1.

When the slow conductance is lower than the fast one, there are two saddle-node bifurcations possible: this bifurcation is located either on the lower left part of the V nullcline or on the upper right part. If the parameter V^0 is between these two limits, there are no fixed points in the phase plane. The same reasoning can be realized with a fixed V^0 and a moving V_s^0. When the conductances have the same value, the two saddle-node bifurcations collide into one point, being a degenerated bifurcation. If the slow conductance is further increased, there are two fixed points in the system. The position of the saddle-node bifurcation has a shape of a peak that is larger when the current is higher.

4.4.4 Types of excitability

Taking into account that the system can be either restorative or regenerative and that there are three possible cases for the choice of conductances, we can draw 9 phase planes (taking into account the limit case where the system is neither restorative or regenerative when $V^0 = V_s^0$) and consider the position of the fixed points. Indeed, the fixed points
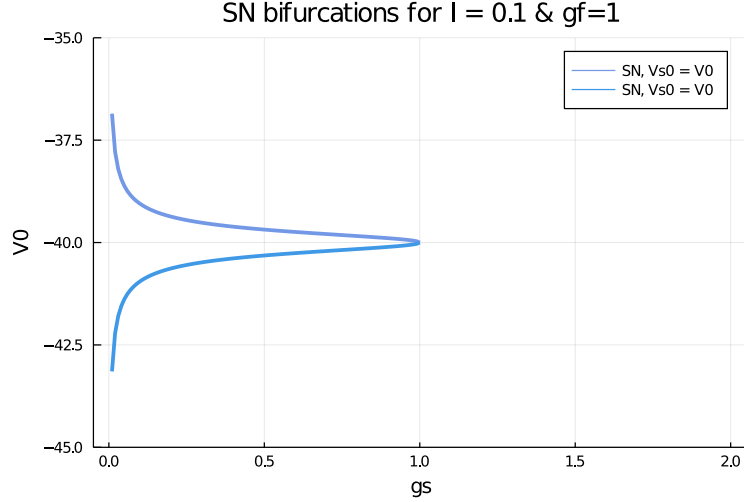
Figure 4.4.6: saddle-node bifurcation position with a varying $\bar{g}_s$. V_s^0 is fixed to be equal to -40. The current is chosen to be close to 0 but non zero so that we see the impact of $\bar{g}_s$. When the current is even closer to 0, the peak becomes sharper.

position can give clues about the system excitability. These 9 phase planes are represented in Figure 4.4.7 for a 0 current.

Let us first consider the Figure 4.4.7A, where, as before, the slow conductance is lower than the fast conductance. When the system is neither restorative or regenerative (when $V^0 = V_s^0$), the degenerated bifurcation appears, where the two couples of fixed points collide at the same point.

In Figure 4.4.7C, the slow conductance is higher than the fast conductance. There is a major impact on the fixed points position: when two fixed points are found, they are either on the attractive or on the repulsive part of the V nullcline. Moreover, the saddle node is always located on the lower part of the V nullcline. If the initial conditions of the system are lower than the saddle coordinates, the system does not converge. In fact, the system will be attracted to the lower left part of the V nullcline and try to reach the V_s nullcline. This will never happen as the V nullcline asymptotes have a slope lower (in absolute value) than the slope of the V_s nullcline. For regenerative systems, bistability cannot be observed as well. However, it is still possible to observe a cycle for the regenerative system and a stable equilibrium for the restorative system.

Choosing the same value for the fast and slow conductances, or even for the same reference potentials, is not a good choice for this work. Indeed, choosing $V^0 = V_s^0$ induces degenerated bifurcations as shown in the middle parts of Figures 4.4.7A and C. In the left and right part of Figure 4.4.7B, we consider respectively the impact of choosing the same conductances for a restorative and a regenerative system. Only one fixed point can be obtained: either on the upper left part of the V nullcline or on the lower right. The other fixed point is rejected to infinity. Unfortunately, this will prevent the system from converging for several sets of initial conditions. The worst choice combines $\bar{g}_f = \bar{g}_s$ and $V^0 = V_s^0$ as the nullclines overlap.
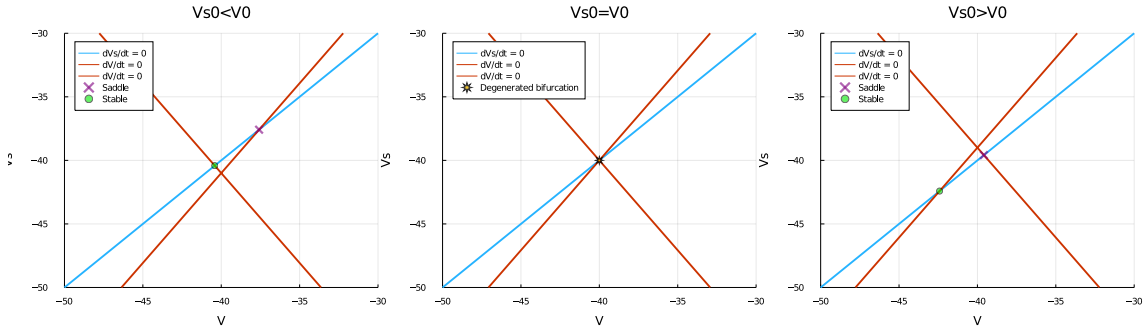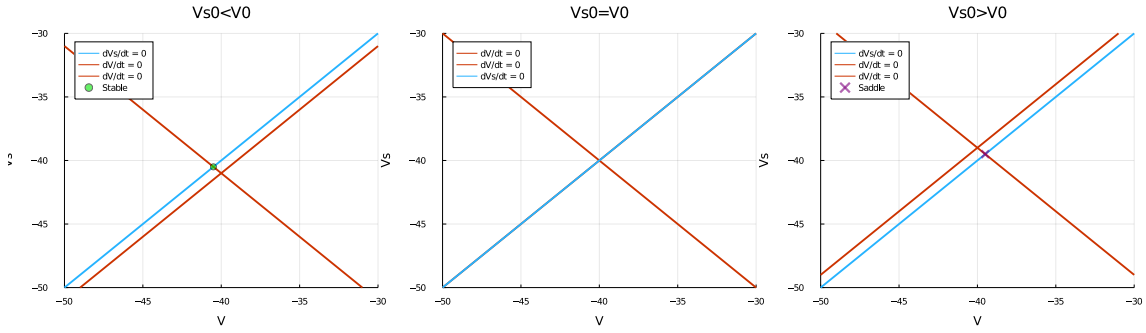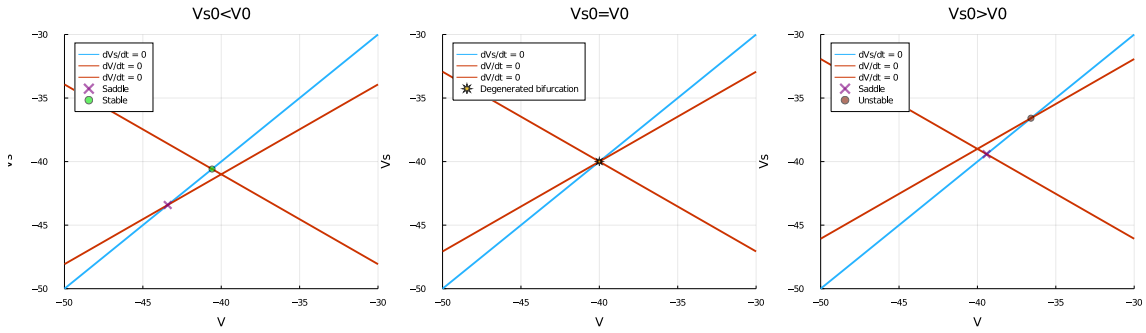
Figure 4.4.7: Fixed points stability and their position evolution in the phase plane with varying parameters V_s^0 and $\bar{g}_s$.

In Figure 4.4.8, we emphasize that the choice of the conductances values is important for the system to converge for any set of initial conditions. Indeed, for a regenerative feedback (Figure 4.4.8, left) and $\bar{g}_f < \bar{g}_s$, only a stable limit cycle can be observed if the system converges. If the choice of conductances is good, meaning that we choose $\bar{g}_f > \bar{g}_s$, bistability can be observed as before. When the current applied increases, the area where a bistable behavior leaves room to the limit cycle only is increased. For a restorative feedback (Figure 4.4.8, right), the switch between steady-state and limit cycle is due to a change in the position of the fixed point. In this part of Figure 4.4.8, the limit between these behaviors seems staircase because a mesh $(\bar{g}_f; \bar{g}_s)$ is used to determine the convergence of the excited system. As for the regenerative system, the restorative system may not converge if $\bar{g}_f < \bar{g}_s$.
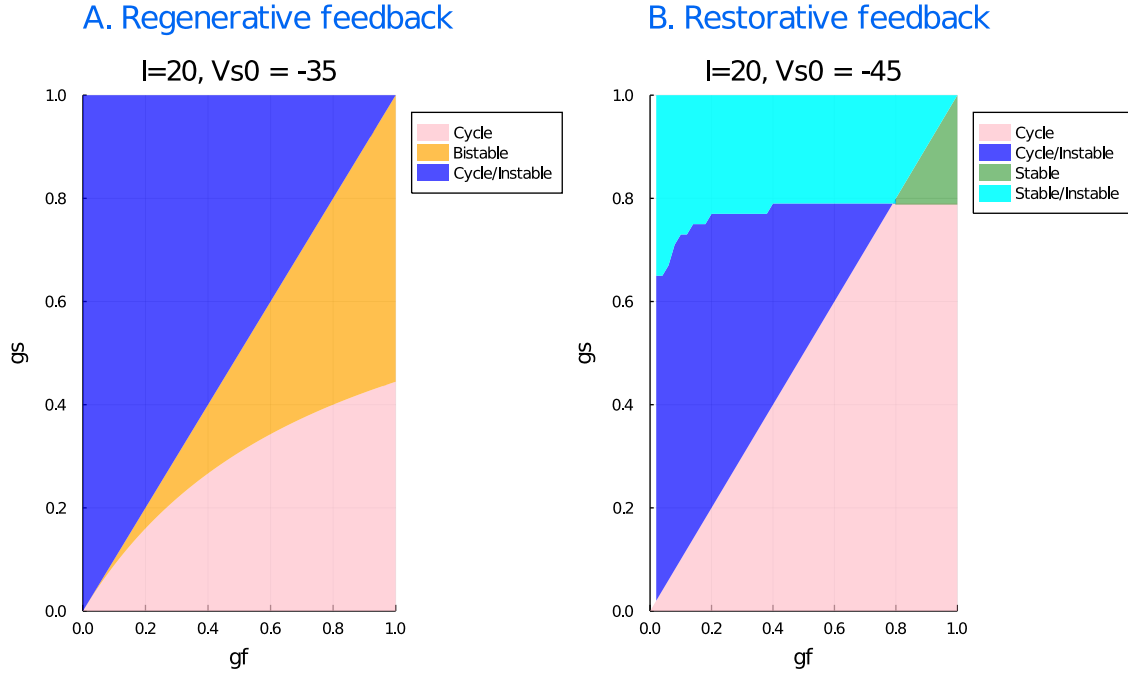
Figure 4.4.8: Approximation of the bifurcation diagram with conductances $\bar{g}_f$ and $\bar{g}_s$ for a regenerative model (A.) and a restorative model (B.) with a high value of current.

4.5 Summary

In this section, we analyzed in-depth the MQIF model with a fast and a slow timescale. It appeared that a slow regenerative feedback is needed to model several properties in DHN firing patterns (bistability, afterdepolarization potential, and spike latency). To understand the impact of each parameter and the dynamic of this model, many bifurcation studies were lead. Finally, we analyzed the impact of the conductances and the reference potentials on the convergence of a perturbed system.

Chapter 5

Burst generation with additional ultra-slow timescale

In this section, we show that bursting can be observed if we add an additional ultra-slow restorative feedback to the 2D slow regenerative MQIF model studied in the previous section.

Contributions   The 3D MQIF model presented allows to model bursting. To understand the mechanisms behind the generation of bursting, we chose to analyze the phase plane of this model and its time responses to a constant current of pulses of current. This section is organized the same way the study of the 2D MQIF model is. First, we take a mathematical approach by computing the nullclines and their intersections to have clues about the phase plane of the 3D model. Next, we present the 3D phase plane and some projections in the space $(V; V_s)$ to show the impact of adding an ultra-slow feedback to the 2D MQIF model. This impact is also discussed based on simulations of the system for a constant applied current and then for several patterns of applied current. Finally, we discuss the impact of the current and a change in the ultra-slow parameters on the 3D MQIF model.

5.1   Model

To add an ultra-slow feedback, we used a supplementary quadratic term in the update equation of the cell potential. This quadratic term has the same shape as the term representing the slow feedback. As for the slow feedback, the strength of the ultra-slow feedback is modulated by the ultra-slow conductance $\bar{g}_{us}$ and the reference potential V_{us}^0. Similarly to the slow potential, we added a third state variable into the new MQIF model, which is the ultra-slow potential V_{us}. The time evolution of this new state variable is scaled by a time constant τ_{us}, equal to 1000 ms. The update of the MQIF model is:

$$
\begin{aligned}
C\dot{V} &= \bar{g}_f(V - V^0)^2 - \bar{g}_s(V_s - V_s^0)^2 - \bar{g}_{us}(V_{us} - V_{us}^0)^2 + I_{\text{app}} && \text{if } V \geq V_{\text{max}}, \text{ then} \\
\tau_s\dot{V}_s &= V - V_s && V \leftarrow V_r, \\
\tau_{us}\dot{V}_{us} &= V - V_{us} && V_s \leftarrow V_{s,r}, \quad (5.1.1) \\
&&& V_{us} \leftarrow V_{us} + \Delta V_{us}.
\end{aligned}
$$

For now, a majority of old parameters are the same as before. However, to keep the same reference potentials chosen in the work of Van Pottelbergh et al., the slow reference potential is fixed at -38.4, which allows to keep a regenerative slow feedback. To ensure the

convergence of this 3D model, the ultra-slow feedback is chosen to be negative. Therefore, the ultra-slow reference potential is set at -50. The associated ultra-slow conductance is set at 0.015. To account for the ultra-slow evolution of V_{us}, its reset value is not fixed. Indeed, each time the cell potential will spike, the ultra-slow potential is increased by ΔV_{us}. In the simulations that will be presented, ΔV_{us} is set to 3.

5.2   Fixed points and nullclines

The nullclines of this new model are computed by setting separately each gradient to 0. The three nullclines equations are:

$$
\begin{aligned}
V \text{ nullcline:} &\quad 0 = \bar{g}_f(V - V^0)^2 - \bar{g}_s(V_s - V_s^0)^2 - \bar{g}_{us}(V_{us} - V_{us}^0)^2 + I_{\text{app}}, \\
V_s \text{ nullcline:} &\quad 0 = V - V_s, \\
V_{us} \text{ nullcline:} &\quad 0 = V - V_{us}.
\end{aligned}
\tag{5.2.1}
$$

Due to the additional dimension, the V nullcline becomes a plane with a particular shape in the 3D space $(V; V_s; V_{us})$. The V_s nullcline also becomes a plane as the straight line $V = V_s$ is projected for each value of V_{us}. Similarly, the V_{us} nullcline is a plane of the same shape.

The ultra-slow feedback has thus an impact on the V nullcline. To understand this impact, it is interesting to rewrite the V nullcline as a function of V and V_{us}, as we did for the analysis of the 2D MQIF model. The V nullcline can therefore be written:

$$
V_s = V_s^0 \pm \sqrt{\frac{\bar{g}_f(V - V^0)^2 + I_t}{\bar{g}_s}} \qquad \text{if } I_t \geq 0,
$$

$$
V = V^0 \pm \sqrt{\frac{\bar{g}_s(V_s - V_s^0)^2 - I_t}{\bar{g}_f}} \qquad \text{if } I_t \leq 0,
$$

$$
\text{with } I_t = I_{\text{app}} - \bar{g}_{us}(V_{us} - V_{us}^0)^2.
$$

Several observations can be made on this set of equations defining the V nullcline in the space $(V; V_s; V_{us})$. In these notations, we use a new variable I_t, that aims to represent the total current in the two dimensional model. In fact, if the ultra-slow potential does not change and is fixed to be equal to its reference potential V_{us}^0, the total current I_t is equal to the applied current I_{app} and the model is similar to a 2D MQIF model. Provided that we want to excite the 3D model, the applied current must be greater than or equal to zero. Indeed, if the applied current is negative, the total current is always negative, making the model to always converge towards a stable equilibrium.

The impact of the additional ultra-slow feedback can be understood as a modulation of the total current in the 2D model. Due to the reset rule, the ultra-slow voltage V_{us} will tend to increase each time the cell potential spikes. If we consider an initial state where the ultra-slow potential is equal to its reference potential, which induces the total current to be equal to its maximum value, the ultra-sow potential will tend to diverge from its reference as long as the cell potential spikes. Therefore, during spiking, the total current in the equivalent 2D model decreases. Eventually, the total current will be equal to or less than 0, preventing the cell potential to spike again. Therefore, quiescent periods can be induced by this ultra-slow restorative feedback. Based on its definition, we see that bursting is thus probably possible with such a model.

The change in the cell potential behavior from spiking to a quiescent period happens when the total current I_t falls below 0. When the total current in the equivalent 2D model is null, the V nullcline is cross-shaped in the space $(V; V_s)$. This happens when the ultra-slow current takes the values:

$$V_{us} = V_{us}^0 \pm \sqrt{\frac{I_{\text{app}}}{\bar{g}_{us}}}.$$

As expected, the reference potential of the ultra-slow potential defines the position where the total current is maximum. The bigger the conductance is, the bigger the impact of the ultra-slow feedback is on the cell potential behavior. The range of values taken by the ultra-slow potential to keep a positive total current will shrink if the conductance $\bar{g}_{us}$ increases. Accordingly, the ultra-slow restorative feedback would much more slow down the cell potential behavior.

The fixed points are found at the intersections of the 3 planes defined by the nullclines equations. As for the 2D MQIF model, we need to solve a second degree equation in V, as the fixed points have the coordinates $(\bar{V}; \bar{V}; \bar{V})$. This equation is:

$$\left(\bar{g}_f - \bar{g}_s - \bar{g}_{us}\right) \bar{V}^2 - 2\left(\bar{g}_f V^0 - \bar{g}_s V_s^0 - \bar{g}_{us} V_{us}^0\right) \bar{V} + \bar{g}_f \left(V^0\right)^2 - \bar{g}_s \left(V_s^0\right)^2 - \bar{g}_{us} \left(V_{us}^0\right)^2 + I_{\text{app}} = 0.$$

Using the discriminant method, we can determine the value of $\bar{V}$. The discriminant can be simplified and we can write the fixed points coordinates as:

$$\bar{V}_{1,2} = \frac{\bar{g}_f V^0 - \bar{g}_s V_s^0 - \bar{g}_{us} V_{us}^0 \pm \sqrt{\Delta}}{\bar{g}_f - \bar{g}_s - \bar{g}_{us}} \text{ with}$$

$$\Delta = \bar{g}_f \bar{g}_s \left(V^0 - V_s^0\right)^2 + \bar{g}_f \bar{g}_{us} \left(V^0 - V_{us}^0\right)^2 - \bar{g}_s \bar{g}_{us} \left(V_s^0 - V_{us}^0\right)^2 - (\bar{g}_f - \bar{g}_s - \bar{g}_{us}) I_{\text{app}}.$$
$$(5.2.2)$$

Similarly to the 2D MQIF, there are at most 2 fixed points, depending on the sign of Δ. As before, if the applied current is very high, there are no fixed points in the phase plane. The stability of these fixed points is determined by the eigenvalues of the Jacobian matrix, calculated based on the 3D model equations:

$$J = \begin{pmatrix} \dfrac{2}{C}\bar{g}_f(V - V^0) & -\dfrac{2}{C}\bar{g}_s(V_s - V_s^0) & -\dfrac{2}{C}\bar{g}_{us}(V_{us} - V_{us}^0) \\ 1 & -1 & 0 \\ 1 & 0 & -1 \end{pmatrix}$$

5.3   Phase plane and reference simulations

5.3.1   Phase plane of the 3D model

The phase plane of the 3D model is represented in Figure 5.3.1. The orange plane is the V nullcline. The pink and blue curves show the intersection between the V nullcline and the V_s or the V_{us} nullclines respectively. This phase plane corresponds to an applied current of 4.

It can be seen that the system is excited as there is no steady-state for this applied current. Also, when V_{us} approaches its reference potential of -50, a well appears in the phase plane. In the range of values of V_{us} associated to this well, the system spikes. Indeed,

as discussed before, V_{us} is close enough to its reference potential to enable the total current in the equivalent 2D model to be positive. In Figure 5.3.2, we show the projections of the V nullcline in the space $(V; V_s)$ for increasing values of V_{us} (left to right). The well is associated to the range of values of V_{us} that induces a positive current in the equivalent 2D model. This well is therefore called excitability well. Therefore, at these locations of the phase plane, the gradient makes the cell potential spike. The trajectory of the system in the excitability well goes from the left (low V) to the right, before being reset on the line $(V_r; V_{us} + \Delta V_{us}; V_{s,r})$.
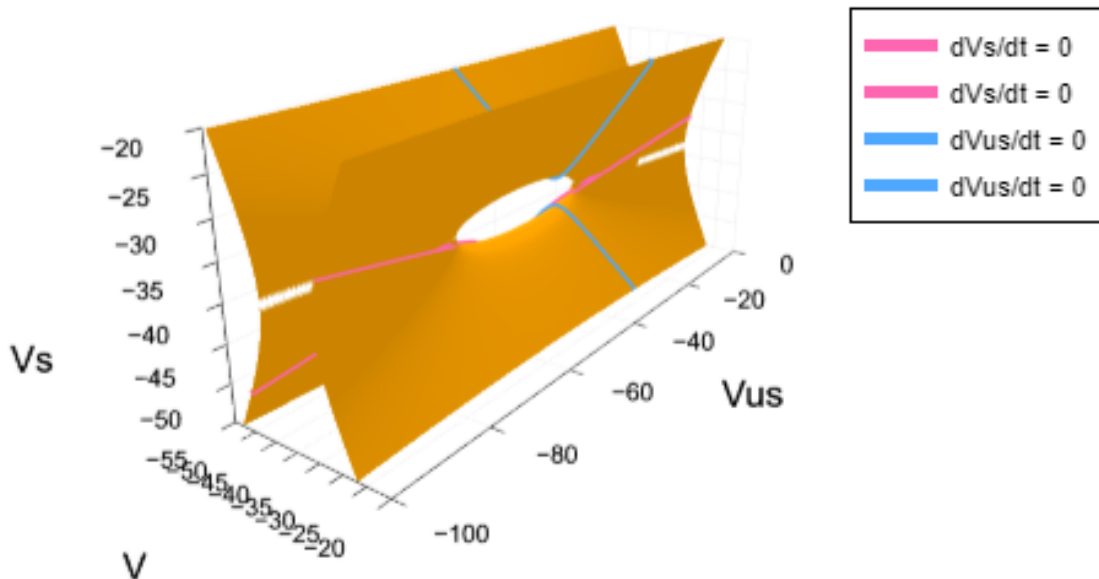

Figure 5.3.1: Phase plane of the 3D model with an added ultra-slow restorative feedback for $I_{app} = 4$. The V nullcline is the plane shown in orange. For the sake of clarity, the V_s and V_{us} nullclines are not shown but rather, we show separately the intersections of these nullclines with the V nullcline. Thus, the pink lines are the curves associated to the intersection between the V and V_s nullclines. The blue lines are the curves associated to the intersection between the V and V_{us} nullclines.

When the applied current is negative, the excitability well disappears as it can be seen in Figure 5.3.3. Thus, each cut $(V; V_s)$ of the 3D phase, obtained for any value of the ultra-slow potential, is similar to Figure 5.3.2, left and right.

5.3.2 Responses to a constant current

For a positive applied current of 4, there are no fixed points in the phase plane. However, the model does not converge towards a classical limit cycle, as the 2D MQIF model did. In fact, due to the added ultra-slow restorative feedback, the model is able to show bursting. In Figure 5.3.4, we show the response of the system submitted to a constant positive current. This figure consists in a time evolution of the cell potential, the slow potential and the ultra-slow potential in the upper part and in a time evolution of the total current I_t. The pink area represents a period of the oscillations described by the model. The zoom on this pink area is provided in Figure 5.3.5.
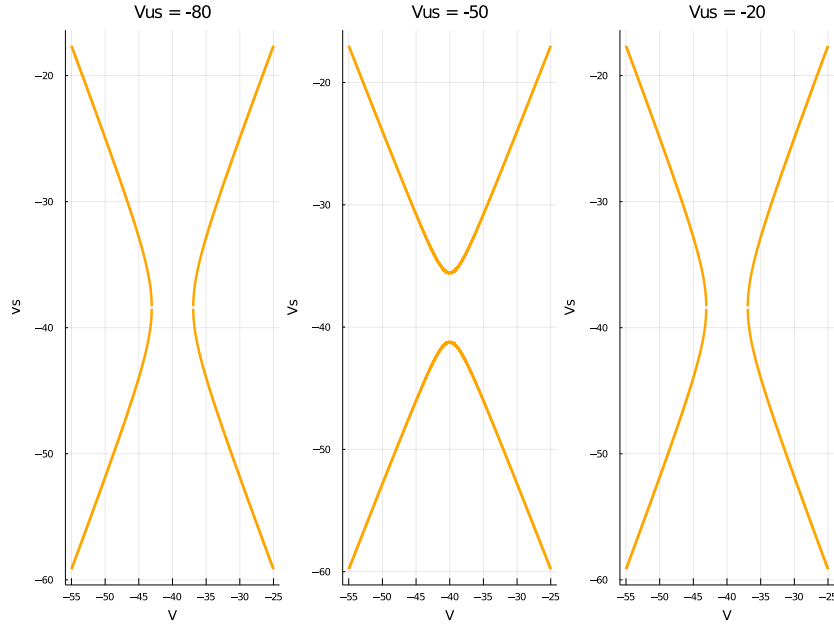
Figure 5.3.2: Projection of the V nullcline in the space $(V; V_s)$ for an increasing V_{us} from left to right. The reference potential of the ultra-slow voltage being equal to -50, the total current associated to the center of this figure is equal to the applied current, which is 4 in this case. The left and the right parts of this figure are the same as the ultra-slow potential chosen are at the same distance of the reference potential.
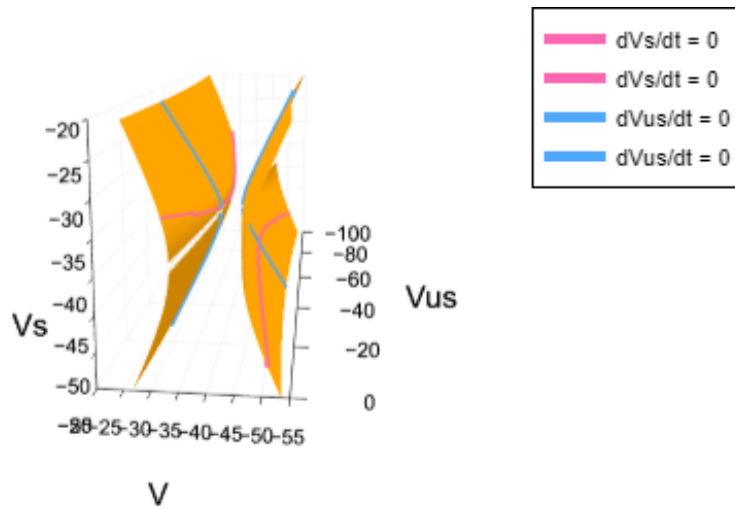

Figure 5.3.3: Phase plane of the 3D model with an added ultra-slow restorative feedback for $I_{\mathrm{app}} = -4$. The V nullcline is the plane shown in orange. For the sake of clarity, the V_s and V_{us} nullclines are not shown but rather, we show separately the intersections of these nullclines with the V nullcline. Thus, the pink lines are the curves associated to the intersection between the V and V_s nullclines. The blue lines are the curves associated to the intersection between the V and V_{us} nullclines.

First, it is clear in Figure 5.3.4 that the period is very much increased due to the ultra-slow restorative feedback. Indeed, without the impact of this timescale, the frequency of the limit cycle was in the order of $100\,\mathrm{Hz}$. Adding the ultra-slow restorative feedback, we
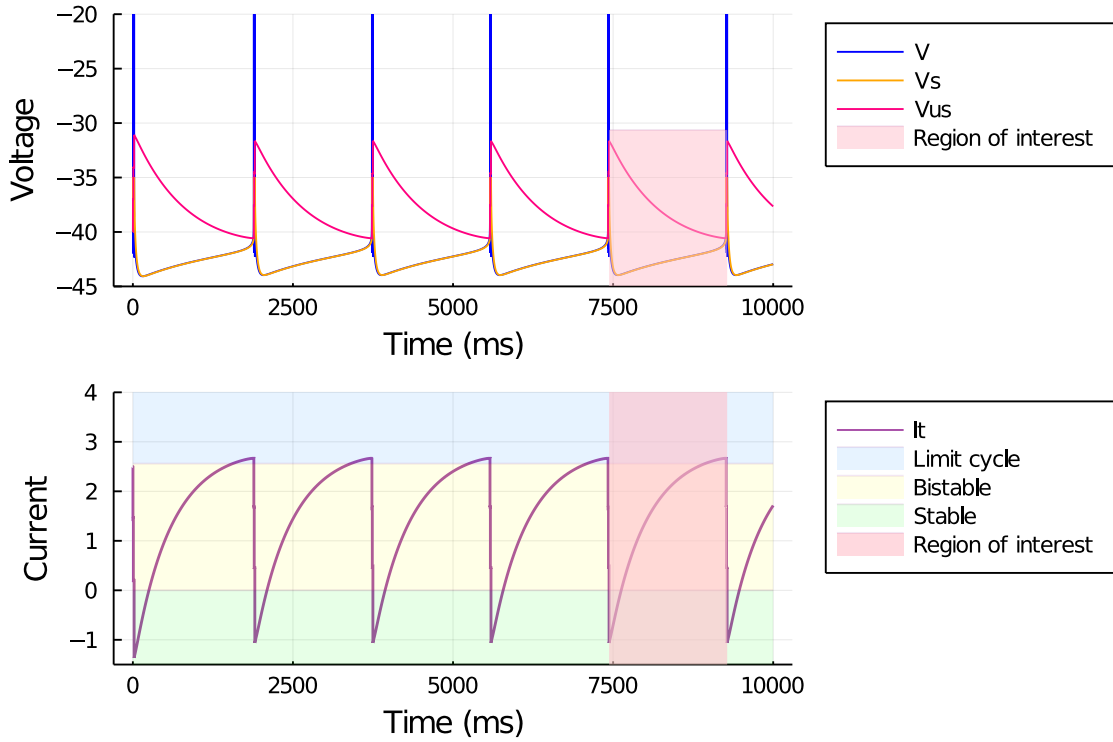
Figure 5.3.4: Response of the system to a constant applied current. The upper plot shows the time evolution of the cell, the slow and the ultra-slow potentials. The lower plot shows the corresponding evolution of the total current I_t, computed based on the ultra-slow potential. To make the parallel with the equivalent 2D model, 3 areas are represented: stable, bistable and limit cycle. These areas actually correspond to the convergence of the equivalent 2D model. In both plots, the pink area is a used to show a zoom in Figure 5.3.5.

see that the frequency of the oscillations is in the order of 1 Hz. During each period, there are a train of spikes and a long quiescent period.

In the zoom provided in Figure 5.3.5, the time window begins at the end of the last spike of the first train of spikes. Due to the reset rule, a train of spikes implies a large increase in the value of V_{us}. This potential being always greater than its reference during the oscillations, an increase in V_{us} involves a decrease in the total current. From there, the equivalent 2D system is attracted to a stable equilibrium, even if the total current slowly increases as the slow feedback is regenerative as explained in the previous section.

At some point, the total current becomes higher than the value at which the saddle-node bifurcation occurs. Thus, the equivalent 2D system spikes after a given spike latency. The light blue marker is positioned at the end of this spike latency. The spike latency ends when the slow voltage is higher that the equivalent V nullcline maximum in the 2D space. Then, the cell potential spikes until the ultra-slow potential implies a bifurcation to a resting state, due to a negative total current, as discussed in the previous subsection. The quiescent period is thus triggered by the ultra-slow potential being too far from its reference potential, making the total current null or negative.
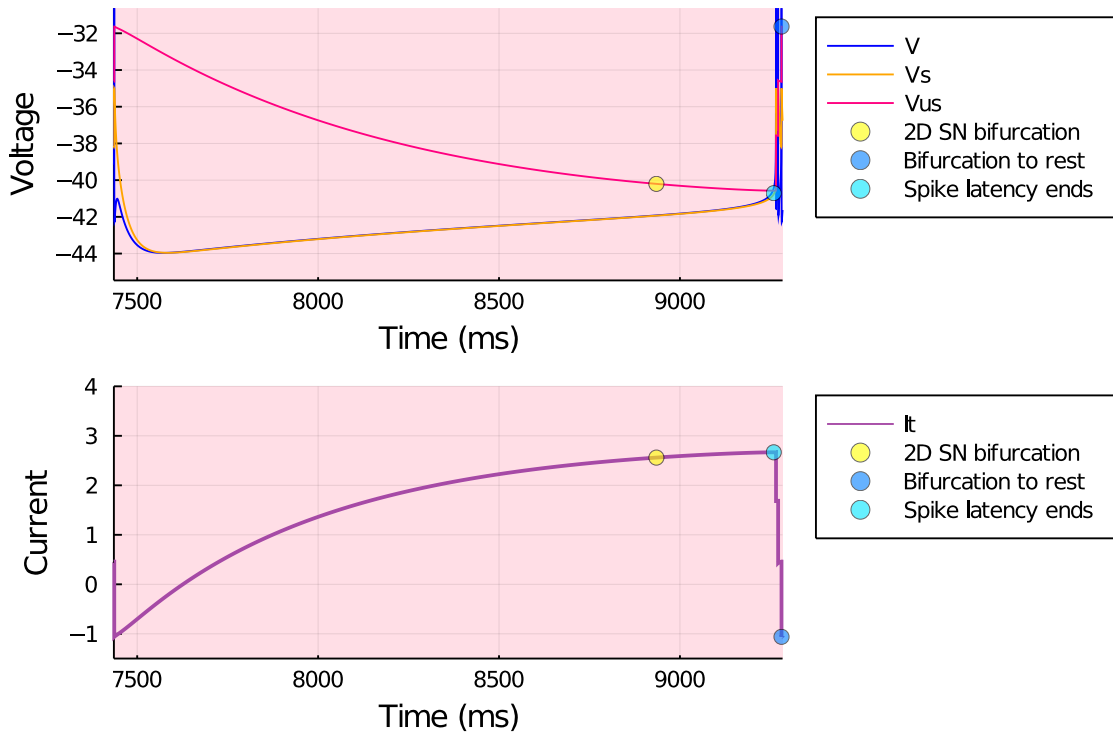
Figure 5.3.5: Zoom on the pink area of the time response shown in Figure 5.3.4. Similarly, the upper plot shows the time evolution of the cell, the slow and the ultra-slow potentials. The lower plot shows the evolution of the total current I_t according to the evolution of the ultra-slow potential. The yellow marker corresponds to the current value at which a saddle-node bifurcation occurs in the equivalent 2D model. The dark blue marker denotes the bifurcation from the bistable behavior to a stable equilibrium when the current becomes negative. The light blue marker is located at the end of the spike latency before the first spike.

The trajectory of the cell potential in the 3D model can be seen as a movement on the bifurcation diagram of the 2D model we presented in the previous section. Indeed, in Figure 5.3.6, we show the bifurcation diagram of the equivalent 2D model. Additionally, we plotted the evolution of the cell potential V as a function of the total current I_t to be consistent with the x-axis of this bifurcation diagram, being usually the current applied to the 2D model. The color gradient on the right of the bifurcation diagram is linked to the trajectory $V(I_t)$ during one period of bursting and represents its time dependency.

During a large majority of the period, the cell potential describes a quiescent period. In fact, the total current being positive, the system is actually in the basin of attraction of the stable equilibrium of the 2D equivalent model. At this stage, the ultra-slow potential is much higher than the cell potential, making the total current very small. Due to its gradient, the ultra-slow potential decreases, meaning that the total current increases. Once the current corresponding to the saddle-node bifurcation is reached, there is a small spike latency. When the spike latency ends, the cell potential spikes, which corresponds to an increase in the ultra-slow potential and a decrease in the corresponding total current. This current decreases until being negative. Then, no more spikes can be generated directly and the system is attracted towards the only attractor left : a steady-state and the cycle
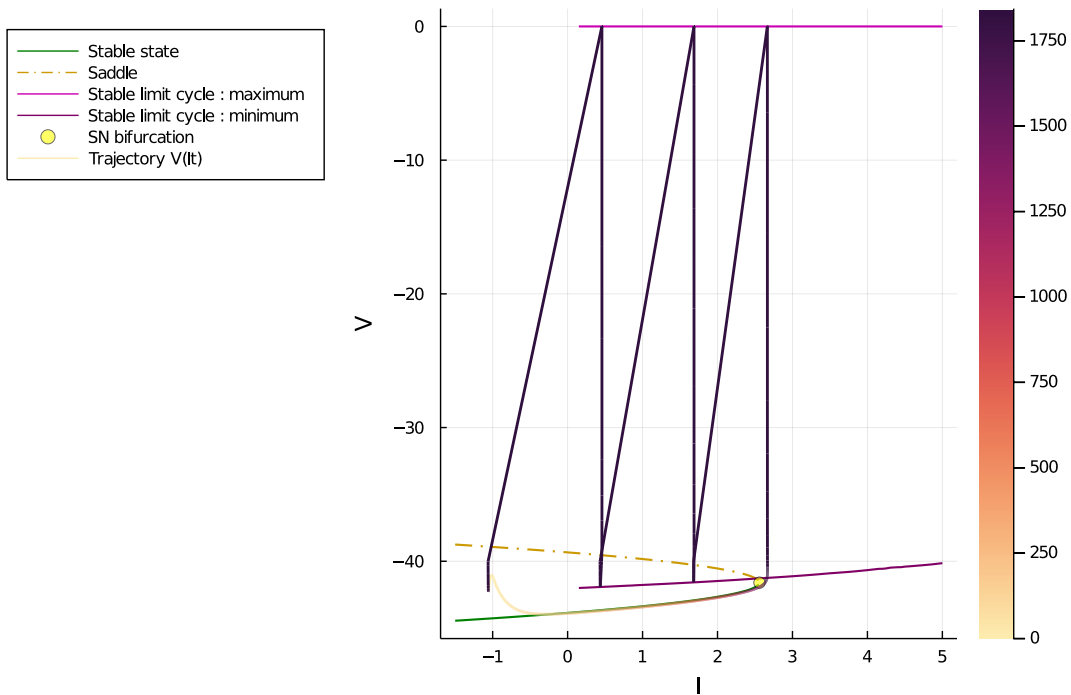
Figure 5.3.6: Trajectory of one period of the cell potential oscillations observed in Figures 5.3.4 and 5.3.5 as a function of the corresponding total current I_t shown in the bifurcation diagram of the equivalent 2D model. On the left, there is a legend associated to the 2D bifurcation diagram only. The V coordinates of the stable and saddle nodes are reported as functions of the total current applied to the equivalent 2D model. As before, if a limit cycle exists, the minimum and maximum of V are also reported. The color gradient on the right of this figure accounts for the time evolution of the cell potential and the total current. The 3 dark triangles correspond to the 3 spikes occurring during the burst of the cell potential trajectory. They have approximately the same color as the duration of the burst is really short compared to the entire period of oscillations. During the quiescent period, the cell potential is located near the stable nodes of the equivalent 2D model.

restarts.

The fact that the slow potential is regenerative is important to generate bursting. Indeed, this slow feedback enables several spikes to generated in a row of short durations. If this feedback was restorative, bistability at the level of the equivalent 2D model would not exist. In this case, the model would spike once, which would make the corresponding total current below the value of the bifurcation. Therefore, the full restorative system would be directly attracted back to the stable equilibrium. The behavior described by the cell potential would be more of a tonic spiking one instead of bursting.

5.3.3 Responses to pulses of current

To further investigate the properties of the 3D system with an ultra-slow feedback, we analyze its response to several pulses of applied current.

Long-time pulse First, in Figure 5.3.7, we see the input applied current in red, which is a pulse. The baseline of the applied current pattern is 0 while its value taken during

the pulse is 20. The cell potential, the slow potential and the ultra-slow potential are shown in blue, green and orange respectively. This current being much higher than before, the interburst frequency is higher, in the order of $10\,\text{Hz}$ approximately. Figure 5.3.7 also contains a zoom on the pulse of applied current and on the associated potentials evolution in the same time interval.
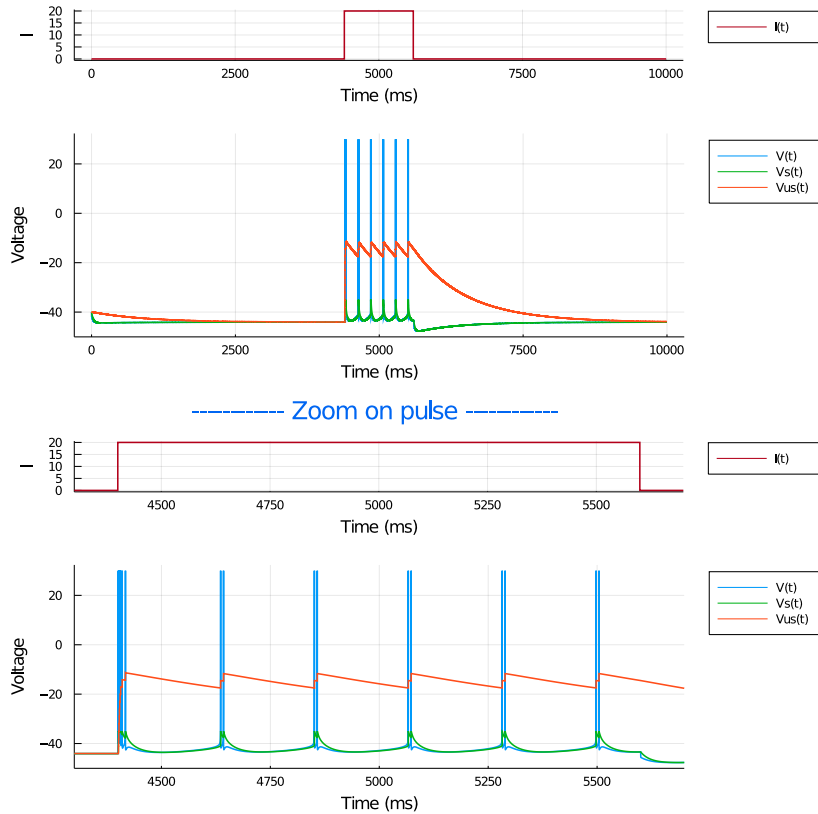

Figure 5.3.7: Time evolution of the 3D model response to a pulse of applied current with a long duration. The two upper plots show respectively the pattern of applied current used in red (with a lowest value of 0 and a highest value of 20) and the corresponding evolution of the cell, the slow and the ultra-slow potentials in blue, green and orange respectively. The two lower plots show a zoom on the center of the pulse of the two upper plots.

During the pulse, the oscillations at equilibrium contain trains of less spikes compared to what we had in Figures 5.3.4 and 5.3.5. At the transition between the baseline value and the highest value of the applied current, the created train of spikes bears more spikes. This is actually due to the fact that the value of the ultra-slow potential at the global equilibrium of the 3D model is close to its reference potential V_{us}^0 when the applied current is null. Therefore, when the applied current is suddenly highly increased, the total current is very close to the applied current. During the oscillations described by the system, the ultra-slow potential is in a range of values so that the total current oscillates in a range of value close to 0. Thus, for a high applied current, V_{us} will oscillate in a range of values much higher to compensate the high applied current. That is the reason why much more spikes are generated by the model at the transition. Moreover, at the transition between high applied current and its baseline, V_{us} is very high and far from its reference potential. Therefore, the total current is highly negative. There is thus a long time interval needed
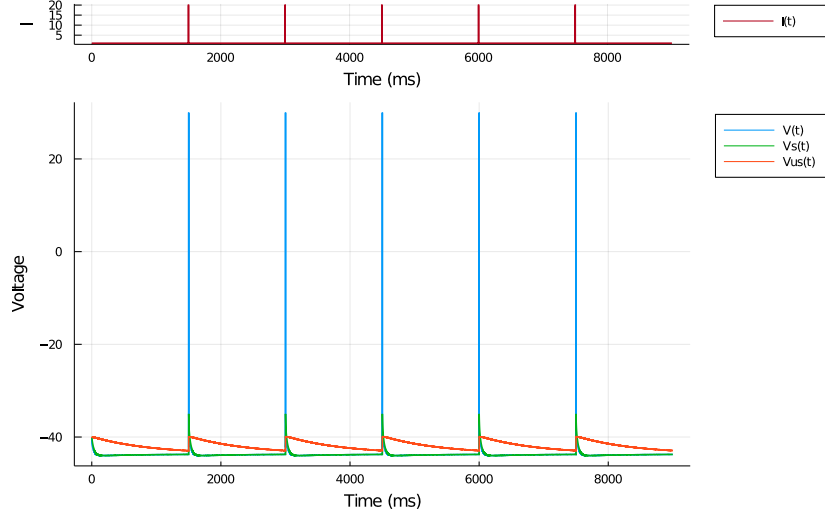
to reach back the final steady-state.

Figure 5.3.8: Time evolution of the 3D model response to several short pulses of applied current. The upper plot shows the pattern of applied current used in red (with a lowest value of 0 and a highest value of 20). The corresponding evolution of the cell, the slow and the ultra-slow potentials are shown in the lower plot in blue, green and orange respectively.

Short-time pulses   In Figure 5.3.8, we simulated 5 short-time pulses of applied current. The highest current of this pattern is of 20, during the pulses. The baseline of the applied current is set at 0. In this simulation, the duration of the pulses is apparently too small to generate several spikes during only one pulse. If the duration of the pulses was longer, we could observe several spikes arranged into a burst, as in Figure 5.3.7. These results seem however similar to what we obtained when we simulated short-time pulses of applied current for a 2D slow restorative system. This is probably due to the fact that the feedback in the last timescale is negative in both cases.

5.4   Bifurcations study

This section aims to further investigate the impact of the parameters I_{app}, $\bar{g}_{us}$ and V_{us}^0 on the new model.

5.4.1   Bifurcation of the full system with current

In figure 5.4.1, we show the influence of the applied current on the 3D MQIF model. The plot that is shown is a bifurcation diagram with the applied current of the full system. For a low applied current, the only attractor in the system is a steady-state. In fact, for a low current, the three planes associated to the nullclines V, V_s and V_{us} intersect into two points. When the current is higher than the bifurcation current at which the saddle-node bifurcation occurs, the system shows an oscillating behavior. Due to the regenerative nature of the slow feedback, these oscillations have the same characteristics as bursting.

We can see that the curve showing the evolution of the minimum value of the cell potential during bursting is not smooth. The non-linearity observed is apparently not a
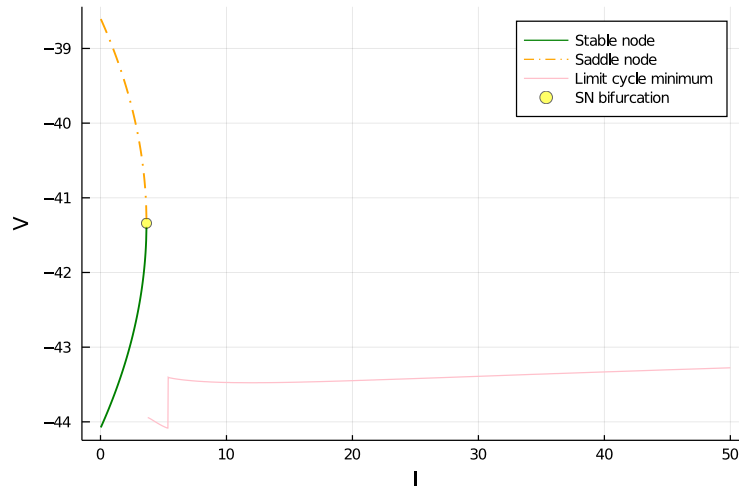
Figure 5.4.1: Bifurcation diagram of the 3D model with the applied current. The V coordinates of the stable and saddle nodes are reported in green and orange respectively. The yellow marker denotes the position of the saddle-node bifurcation, where the stable and saddle nodes collide. The dark yellow line reports the minimum of the oscillations for a given applied current.

numerical error but matches with a change in the number of spikes during the burst. In Figure 5.4.2, we show the evolution of the number of spikes with the applied current of the 3D model (lower part) and the according evolution of the interburst frequency, being the frequency of the oscillations observed, with the applied current. The non-linearity observed in the bifurcation diagram of Figure 5.4.1 appears also in the evolution of the interburst frequency and matches the switch in the number of spikes during each burst from 3 to 2 spikes. We see that the interburst frequency increases with the applied current, which is consistent with what we observed for the response of the system to a pulse of long duration compared to its response to a constant current of 4, in Figures 5.3.7 and 5.3.4 respectively.
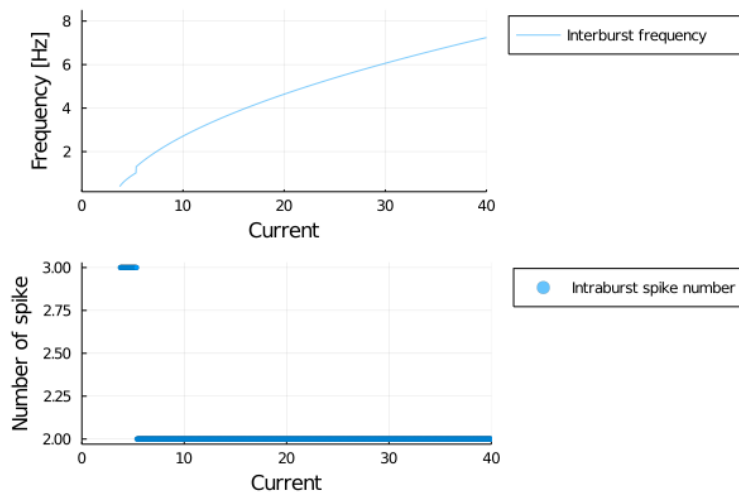

Figure 5.4.2: Evolution of the interburst frequency (upper part), being the frequency of the oscillations in the cell potential, and of the number of spikes in the burst (lower part) with the applied current.

In Figure 5.4.3, we computed the evolution of the averaged instantaneous intraburst frequency, being the instantaneous frequency between each spike in the burst. This frequency globally decreases with the applied current. Before the non-linearity, there are 3 spikes in the burst. Thus, we also reported the maximum and minimum intraburst frequencies, being actually the two frequencies observed for a given current.
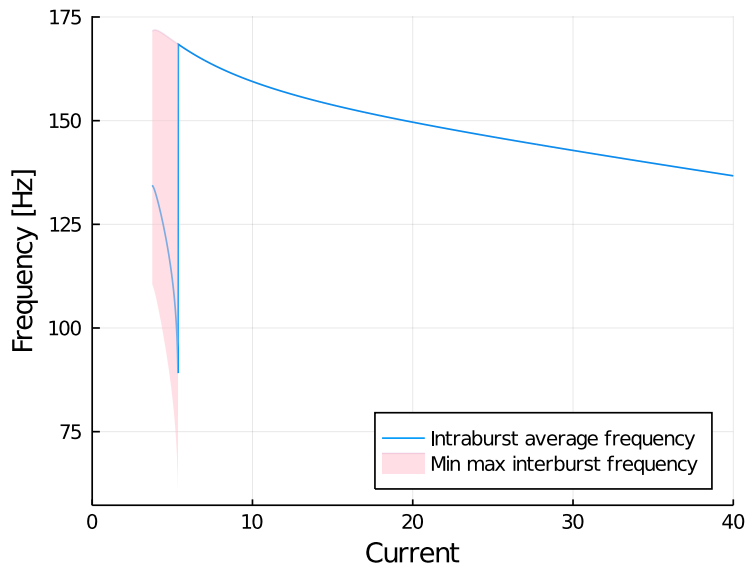

Figure 5.4.3: Evolution of the averaged instantaneous intraburst frequency, being the instantaneous frequency between two spikes in a burst of the cell potential, with the applied current. When there are more than 2 spikes in the burst, the pink area covers the range of values between the minimum and maximum observed instantaneous frequencies for a given applied current.

5.4.2 Impact of the ultra-slow feedback on the 2D equivalent system stability

The impact of the ultra-slow parameters $\bar{g}_{us}$ and V_{us}^0 can be investigated using a simulation of the model for a constant current of 4 as in Figures 5.3.4 and 5.3.5. The figures that will be presented here consist in the time evolution of the potentials V, V_s and V_{us} in the same time interval as in Figure 5.3.4 (upper part) and in a zoom on a period of oscillations on the potentials V, V_s and V_{us} as in Figure 5.3.5. Each figure presented in the following developments results from a change in either $\bar{g}_{us}$ or V_{us}^0.

First, we show in Figure 5.4.4 the response of the system with a conductance of the ultra-slow feedback decreased by a factor 10. The ultra-slow conductance tested is thus equal to 0.0015. In fact, decreasing the conductance of the ultra-slow feedback decreases its strength. Accordingly, we observe that the slow regenerative feedback has a greater impact on the cell potential. Indeed, the interburst frequency is increased and the number of spikes during the burst increases. Mathematically, the increase in the number of spikes is due to the fact that the total current is less sensitive to a change in the ultra-slow potential if $\bar{g}_{us}$ is decreased. Thus, when the cell potential spikes, the corresponding increase in the ultra-slow potential implies a smaller increase in the total current. This allows the cell potential to generate more spikes during each burst. The increase in the interburst

frequency corresponds to the fact that the oscillations in the ultra-slow potential stabilize in a higher range of values than before. Thus, the gradient of V_{us} is higher which implies a faster change in the total current during the quiescent period.
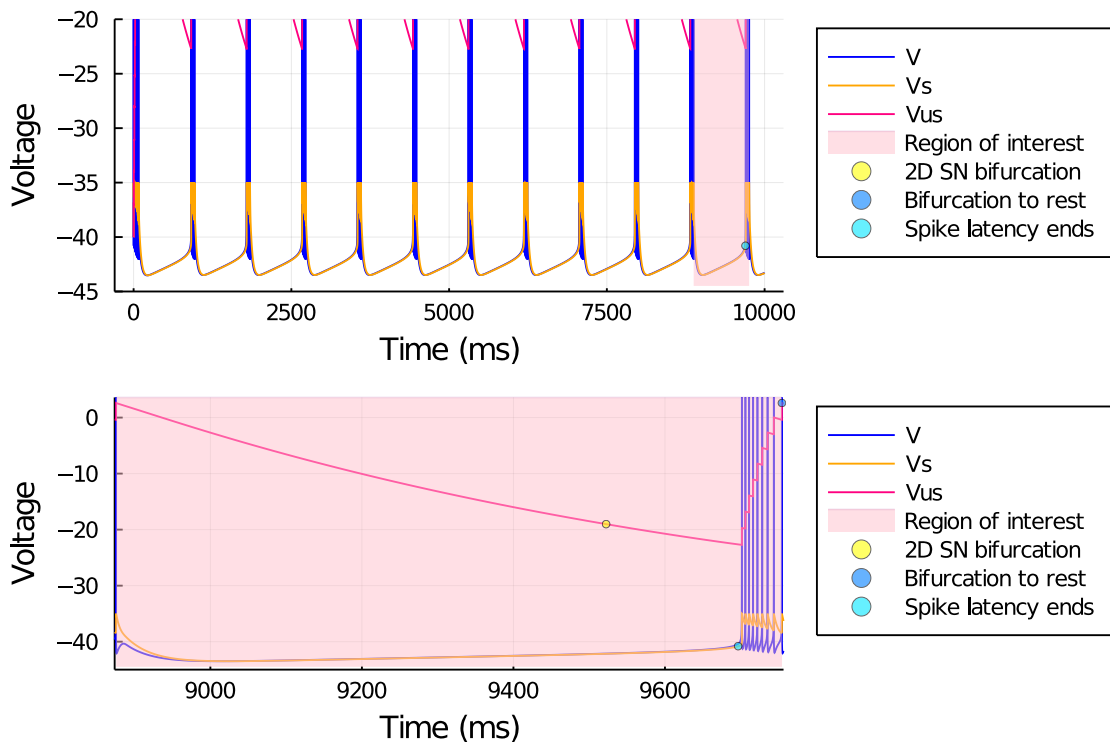

Figure 5.4.4: Evolution of the cell, slow and ultra-slow potentials under a constant applied current of 4 and a decreased ultra-slow conductance from 0.015 to 0.0015 (upper part). A region of interest highlights a single period of bursting and is shown separately (lower part). The yellow marker is positioned at the value of V_{us} that involves a total current I_t at which a saddle-node bifurcation occurs in the equivalent 2D model. The dark blue marker is located where the total current goes below 0. The light blue marker shows where the spike latency ends.

In Figure 5.4.5, we show the evolution of the 3D model potentials for a constant current of 4 with an increased ultra-slow reference potential, set to -45 instead of -50. The interburst frequency increases as a response to this change. Once again, the oscillations in the ultra-slow potentials stabilize in a higher range than before. Consequently, the gradient of the ultra-slow potential is higher, making the interburst frequency higher. However, for a change in the ultra-slow potential, there is apparently no increase nor decrease in the number of spikes per burst. This would actually be due to the fact that a change in the ultra-slow potential corresponds to the same rate of change in the total current. Thus, a change in V_{us}, notably during a train of spikes, has the same effect on I_t, whether the ultra-slow reference potential is set to -50 or -45. However, one should bear in mind that a change in the ultra-slow reference potential or in the ultra-slow conductance has an impact on the position of the saddle-node bifurcation of the 3D model. Thus, for a given applied current, it is possible to stop observing bursting if these parameters are changed.
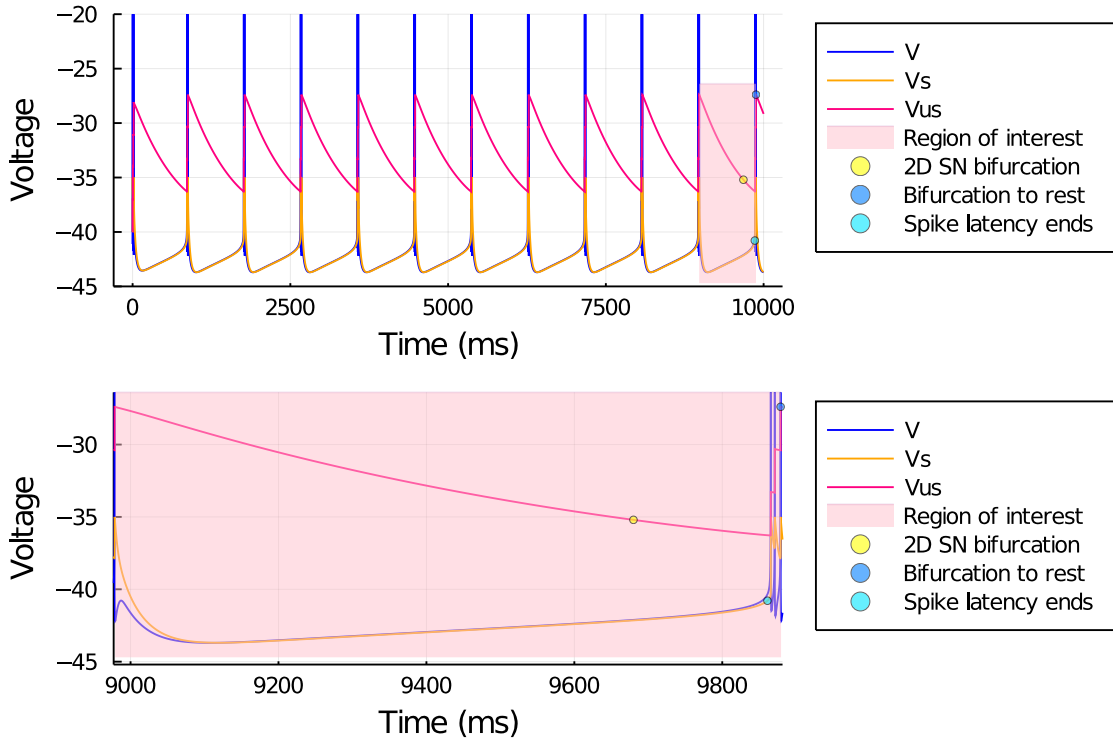
Figure 5.4.5: Evolution of the cell, slow and ultra-slow potentials under a constant applied current of 4 and an increased ultra-slow reference potential from -50 to -45 (upper part). A region of interest highlights a single period of bursting and is shown separately (lower part). The yellow marker is positioned at the value of V_{us} that involves a total current I_t at which a saddle-node bifurcation occurs in the equivalent 2D model. The dark blue marker is located where the total current goes below 0. The light blue marker shows where the spike latency ends.

5.5   Summary

In this section, we showed that the MQIF with a fast, a slow, and an ultra-slow timescale is suited to model bursting. The 3D MQIF model created was analyzed mathematically based on its nullclines expressions and the corresponding fixed points. As in the previous section, the 3D MQIF model shows saddle-node bifurcation with 0, 1, or 2 fixed points. When two fixed points are found, they are always a stable and a saddle nodes in this case.

The ultra-slow feedback impacts the V nullcline. This nullcline was shown in the space (V, V_{us}, V_s) to reinforce that the ultra-slow feedback changes the total current I_t in the equivalent 2D MQIF model. The reference potential of this feedback defines where the impact is the lowest. The conductance of this feedback defines its strength and how much a change in the ultra-slow voltage impacts the total current in the equivalent 2D model. The link with the equivalent 2D MQIF model is also highlighted if we represent the evolution of the cell potential during a period of bursting as a function of the total current I_t (which depends on the ultra-slow voltage) in the bifurcation diagram of the 2D equivalent model for a varying current. The ultra-slow voltage induces a displacement along the stable equilibrium line, which creates the quiescent period in bursting, and a switch to a cyclic behavior, which creates the train of spikes, when the current is larger

than the bifurcation.

Finally, the study of the behavior of this model with the applied current I_{app} showed that the time responses of the new 3D MQIF model to short time pulses was similar to the responses of the 2D slow restorative model. However, due to complex non-linear effects, the bifurcation diagram and the frequencies evolution with the applied current are different. Globally, this is because the slow regenerative feedback interacts with the ultra-slow restorative feedback, notably to create bursting.

Chapter 6

Plateau potentials generation with additional super-slow timescale

In this chapter, we show that plateau potentials and accelerating behaviors can be observed if we add an additional super-slow regenerative feedback to the 3D MQIF model studied in the previous section. The new 4D model consists in 4 feedbacks: a fast one, a slow regenerative one, a super-slow regenerative one, and an ultra-slow restorative one. The super-slow feedback added in this chapter is characterized by a time constant between the one of the slow feedback and the one of the ultra-slow feedback.

Contributions   The development of the 4D MQIF model is essential to model the two resting firing patterns shown by DHNs, being the accelerating behavior and plateau potentials. Indeed, these firing patterns depend on the strength of a super-slow regenerative feedback that is added to the 3D MQIF model presented in the previous chapter. As before, we take a mathematical approach to have clues about how the super-slow feedback impacts the model dynamics. The dynamics of this model are then analyzed based on the model response to a constant applied current. Such simulations support the description of the movement of the V nullcline in the 3D space induced by the additional variation of the super-slow potential. To simulate all DHNs firing patterns (except bursting which is observed for a constant current), we must give an input pulse of applied current. We created a methodology to determine the baseline and the maximum of the applied current for the input pulse, as it is shown that the current has a large impact on the results. The impact of a choice of conductances is also studied, which allows to understand how each firing pattern is created in terms of feedbacks strength. Finally, eight additional firing patterns, distinct from the 4 firing patterns of DHNs, can be obtained for various sets of conductances and values of current and are presented.

6.1   Model

Similarly to the reasoning made to add the ultra-slow feedback, a supplementary quadratic term is used in the update equation of the cell potential of the 3D MQIF model, found in equation (5.1.1). As before, this new term has the same shape as the terms representing the slow or the ultra-slow feedbacks. The strength of the added super-slow feedback is modulated by the super-slow conductance $\bar{g}_{ss}$ and by the corresponding super-slow reference potential V_{ss}^0. Accordingly, a new state variable, the super-slow potential V_{us}, and its

update equation are added to the model, leading to the 4D MQIF model:

$$
\begin{aligned}
C\dot{V} =& \bar{g}_f(V - V^0)^2 - \bar{g}_s(V_s - V_s^0)^2 - \bar{g}_{ss}(V_{ss} - V_{ss}^0)^2 - \bar{g}_{us}(V_{us} - V_{us}^0)^2 + I_{\text{app}} \\
\tau_s\dot{V}_s =& V - V_s \\
\tau_{ss}\dot{V}_{ss} =& V - V_{ss} \\
\tau_{us}\dot{V}_{us} =& V - V_{us} \\
& \text{if } V \geq V_{\max}, \text{ then } V \leftarrow V_r, V_s \leftarrow V_{s,r}, V_{ss} \leftarrow V_{ss} + \Delta V_{ss} \text{ and } V_{us} \leftarrow V_{us} + \Delta V_{us}
\end{aligned}
$$

(6.1.1)

The time constant of the super-slow feedback is supposed to be lower than the ultra-slow time constant of $1000\,\text{ms}$ but greater than the slow time constant of $10\,\text{ms}$. Thus, τ_{ss} is set to $100\,\text{ms}$. As a reminder, the time constant of the fast feedback is set at $1\,\text{ms}$ and the capacity of the membrane is set to 1. The reference potentials are the same as before: the cell reference potential V^0 is set at -40, the slow reference potential V_s^0 is set at -38.4 to have a slow regenerative feedback and the ultra-slow potential V_{us}^0 is set at -50. The reference potential of the super-slow feedback is set to -10. This value is chosen to be far from the other reference potentials so that the super-slow feedback is more regenerative near rest. Intuitively, to model plateau potentials, we need a super-slow feedback, slower than the slow regenerative one, that creates positive feedback near rest so that the increase in spike frequency and the afterdischarge can be observed. A reference potential for the super-slow potential of -10 is thus suited for this purpose.

The reset rule is applied when the cell potential is equal to or greater than $V_{\max}$, which is chosen to be equal to 30. The cell potential is reset at a value V_r of -40, as for the 2D and the 3D MQIF models. The other values needed to apply the reset rule are chosen based on [Pottelbergh et al., 2018]: the reset value $V_{s,r}$ is set at -25 and the increase in the super-slow and ultra-slow potentials, ΔV_{ss} and ΔV_{us} respectively, are both set to 3. Finally, the conductance of the fast feedback $\bar{g}_f$ is set to 1. The other conductances are not fixed in this section to allow us to see that this model is suited to represent each type of firing patterns shown by DHNs.

6.2   Fixed points and nullclines

As for the previous section, the equations of the nullclines are computed by equaling each gradient to 0. This leads us to the following set of 4 nullclines:

$$
\begin{aligned}
V \text{ nullcline:} \quad & 0 = \bar{g}_f(V - V^0)^2 - \bar{g}_s(V_s - V_s^0)^2 - \bar{g}_{ss}(V_{ss} - V_{ss}^0)^2 - \bar{g}_{us}(V_{us} - V_{us}^0)^2 + I_{\text{app}}, \\
V_s \text{ nullcline:} \quad & 0 = V - V_s, \\
V_{ss} \text{ nullcline:} \quad & 0 = V - V_{ss}, \\
V_{us} \text{ nullcline:} \quad & 0 = V - V_{us}.
\end{aligned}
$$

(6.2.1)

As the model counts the 4 dimensions V, V_s, V_{ss} and V_{us}, these nullclines are hyperplanes. The phase plane of this model will thus not be represented here. However, as the added feedback has the same shape as the other ones, its effect on the phase plane must be correlated to the effect of the added ultra-slow feedback on the V nullcline of the equivalent

2D MQIF model. To justify it, we can rewrite the V nullcline equation as:

$$V_s = V_s^0 \pm \sqrt{\frac{\bar{g}_f(V - V^0)^2 + I_t}{\bar{g}_s}} \qquad\qquad \text{if } I_t \geq 0,$$

$$V = V^0 \pm \sqrt{\frac{\bar{g}_s(V_s - V_s^0)^2 - I_t}{\bar{g}_f}} \qquad\qquad \text{if } I_t \leq 0,$$

$$\text{with } I_t = I_{\text{app}} - \bar{g}_{ss}(V_{ss} - V_{ss}^0)^2 - \bar{g}_{us}(V_{us} - V_{us}^0)^2.$$

The total current I_t in the equivalent 2D MQIF model dictates the evolution of the cell potential. This current depends on two states variables, V_{ss} and V_{us}. To contrast, the 3D model presented in the previous section is characterized by a total current that depends only on V_{us}. As we explained, the ultra-slow feedback creates an excitability well in the 3D phase plane for a positive applied current. In the case of the 4D model, the size of the excitability well is modulated across time. Supposing that the super-slow potential does not change and that it is fixed to its reference potential, the 4D model is reduced to the 3D model presented. The total current is equal to 0 when the following equality is verified:

$$V_{ss} = V_{ss}^0 \pm \sqrt{\frac{I_{\text{app}} - \bar{g}_{us}(V_{us} - V_{us}^0)^2}{\bar{g}_{ss}}},$$

provided that $I_{\text{app}} - \bar{g}_{us}(V_{us} - V_{us}^0)^2$ is positive. This happens when the ultra-slow voltage is close enough to its reference potential. However, if the super-slow or the ultra-slow potentials are too far from their respective references, then the total current is negative and a quiescent period is induced. Bursting would thus still be observed in the 4D model response.

The fixed points of the 4D MQIF model are found at the intersection of all hyperplanes, provided that they intersect at the same location(s) of the 4D phase plane. The V_s, V_{ss} and V_{us} nullclines equations imply that each fixed point has the same coordinates across all state variables, noted $\bar{V}$. Using this substitution, the fixed points coordinates can be computed by solving the following equation:

$$(\bar{g}_f - \bar{g}_s - \bar{g}_{ss} - \bar{g}_{us})\,\bar{V}^2 - 2\left(\bar{g}_f V^0 - \bar{g}_s V_s^0 - \bar{g}_{ss}V_{ss}^0 - \bar{g}_{us}V_{us}^0\right)\bar{V} + \bar{g}_f\left(V^0\right)^2 - \bar{g}_s\left(V_s^0\right)^2$$
$$- \bar{g}_{ss}\left(V_{ss}^0\right)^2 - \bar{g}_{us}\left(V_{us}^0\right)^2 + I_{\text{app}} = 0.$$

Using the discriminant method, the mathematical expression of the fixed points coordinates is:

$$\bar{V}_{1,2} = \frac{\bar{g}_f V^0 - \bar{g}_s V_s^0 - \bar{g}_{ss}V_{ss}^0 - \bar{g}_{us}V_{us}^0 \pm \sqrt{\Delta}}{\bar{g}_f - \bar{g}_s - \bar{g}_{ss} - \bar{g}_{us}} \text{ with}$$

$$\Delta = \bar{g}_f\bar{g}_s\left(V^0 - V_s^0\right)^2 + \bar{g}_f\bar{g}_{ss}\left(V^0 - V_{ss}^0\right)^2 + \bar{g}_f\bar{g}_{us}\left(V^0 - V_{us}^0\right)^2 - \bar{g}_s\bar{g}_{ss}\left(V_s^0 - V_{ss}^0\right)^2$$
$$- \bar{g}_s\bar{g}_{us}\left(V_s^0 - V_{us}^0\right)^2 - \bar{g}_{ss}\bar{g}_{us}\left(V_{ss}^0 - V_{us}^0\right)^2 - (\bar{g}_f - \bar{g}_s - \bar{g}_{ss} - \bar{g}_{us})I_{\text{app}}. \qquad (6.2.2)$$

As for the 3D MQIF, there are 0, 1, or 2 fixed points, depending on the sign of Δ. Moreover, a high and negative applied current involves a positive Δ, meaning that there are two fixed points in the 4D phase plane. The stability of the fixed points is defined by the Jacobian

matrix, being:

$$J = \begin{pmatrix} \dfrac{2}{C}\bar{g}_f(V - V^0) & -\dfrac{2}{C}\bar{g}_s(V_s - V_s^0) & -\dfrac{2}{C}\bar{g}_{ss}(V_{ss} - V_{ss}^0) & -\dfrac{2}{C}\bar{g}_{us}(V_{us} - V_{us}^0) \\ 1 & -1 & 0 & 0 \\ 1 & 0 & -1 & 0 \\ 1 & 0 & 0 & -1 \end{pmatrix}$$

6.3 Phase plane and reference simulation

6.3.1 Responses to a constant current

To understand the impact of the super-slow feedback on the time response of the cell potential, we simulated the 4D MQIF model with an applied current of 20. This current is chosen to be slightly higher than the bifurcation current. The conductances chosen for this simulation are found in Table 6.1.

$\bar{g}_f$	$\bar{g}_s$	$\bar{g}_{ss}$	$\bar{g}_{us}$
1	0.5	0.015	0.0015

Table 6.1: Conductances used to simulate Figures 6.3.1 and 6.3.2

The value of the fast and the slow conductances are the same as before. However, the conductance of the ultra-slow feedback is decreased by a factor 10. The conductance of the super-slow feedback is chosen to be 10 times greater than the ultra-slow conductance. The reason behind this choice is that a higher conductance for the super-slow feedback will induce a larger effect of the super-slow feedback compared to the effect of the ultra-slow one.

In Figure 6.3.1, the response of the 4D model across time is represented. The upper part of this plot shows the evolution of the potentials V, V_s, V_{ss} and V_{us} during the simulation. The lower part of this figure shows the corresponding evolution of the total current in the equivalent 2D MQIF model. For the set of conductances chosen, the behavior that is modeled is still bursting. However, compared to the response of the 3D model to a constant current shown in Figure 5.3.4, the shape of the total current is much more different. First, the total current covers a larger range of values when the super-slow feedback is applied. Second, the total current evolution contains sharp spikes.

To understand how the super-slow feedback impacts the 4D MQIF model response, it is helpful to consider a single period of oscillations. In Figure 6.3.2, we show a zoom on a period of Figure 6.3.1. Similarly, the lower plot shows the corresponding evolution of the total current during a period of oscillations. The evolution of the ultra-slow current and the super-slow currents are also represented. In fact, as they both modulate the total current in the equivalent 2D model, considering them separately may help to understand the shape of the total current. As a reminder, the super-slow and ultra-slow currents are expressed respectively as:

$$I_{ss} = -\bar{g}_{ss}(V_{ss} - V_{ss}^0)^2 \text{ and}$$
$$I_{us} = -\bar{g}_{us}(V_{us} - V_{us}^0)^2,$$
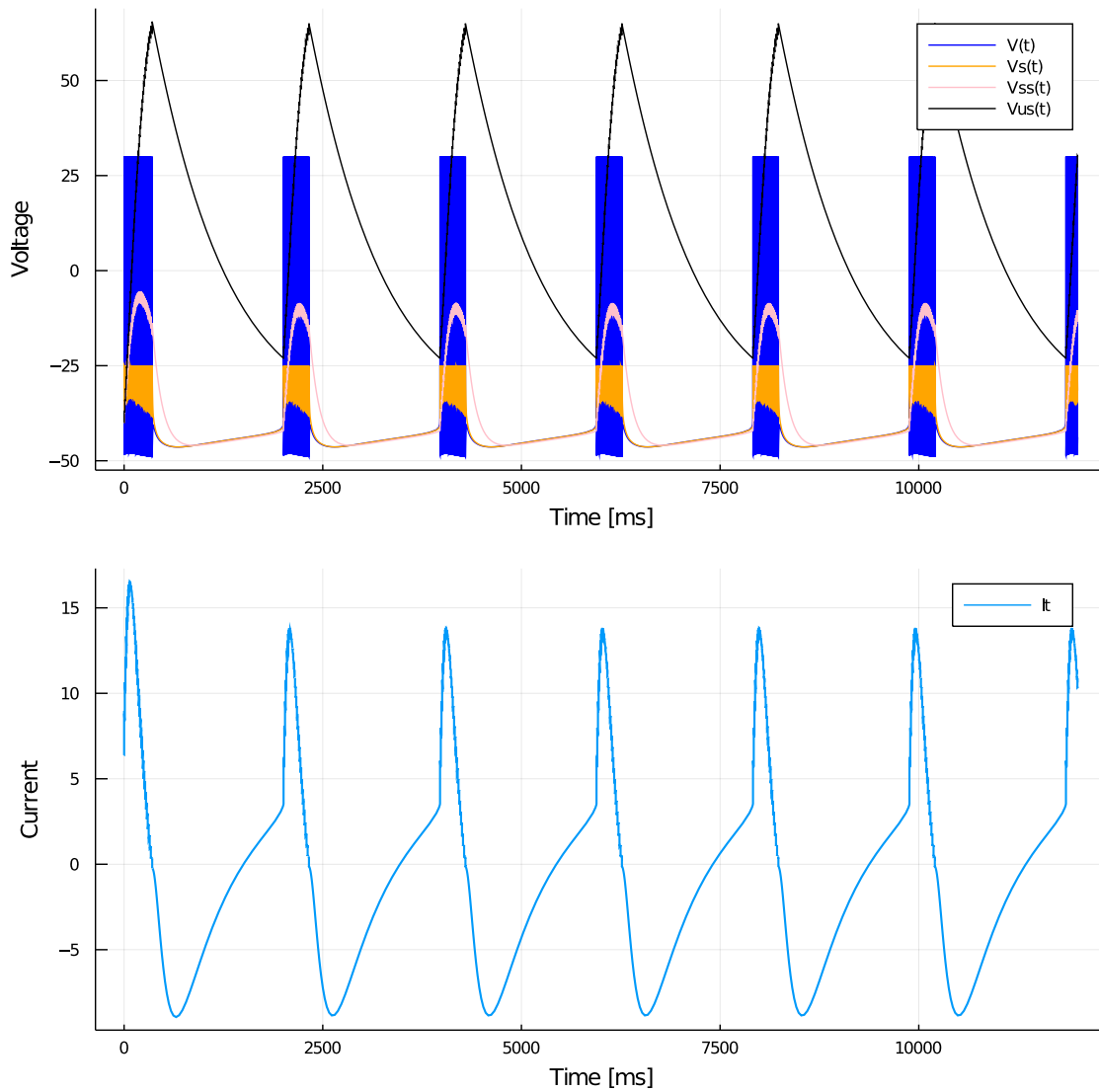$$\text{with } I_t = I_{app} + I_{ss} + I_{us}.$$

Figure 6.3.1: Time response of the 4D MQIF model to a constant current of 20. The set of conductances used for this simulation can be found in Table 3.1. The upper plot shows the evolution of the 4 potentials V, V_s, V_{ss} and V_{us}. The lower plot shows the corresponding evolution of the total current in the equivalent 2D model.

The upper plot shows the evolution of the potentials during the simulation. The reference potentials of the slow, super-slow and ultra-slow feedbacks are also represented. They aim to understand the shape of the super-slow and the ultra-slow currents separately.

At the beginning of this period, the total current is positive. This is mainly due to the super-slow potential that is far from its reference. Indeed, as the ultra-slow potential is relatively low, this potential is at the closest position to its reference potential. In response, the cell potential spikes. Due to the reset rule, the super-slow and ultra-slow potentials increase at each spike of the cell potential. Thus, the super-slow potential is brought closer to its reference while the gap between the ultra-slow potential and its reference increases. Thus, the absolute value of the super-slow current decreases and the absolute value of
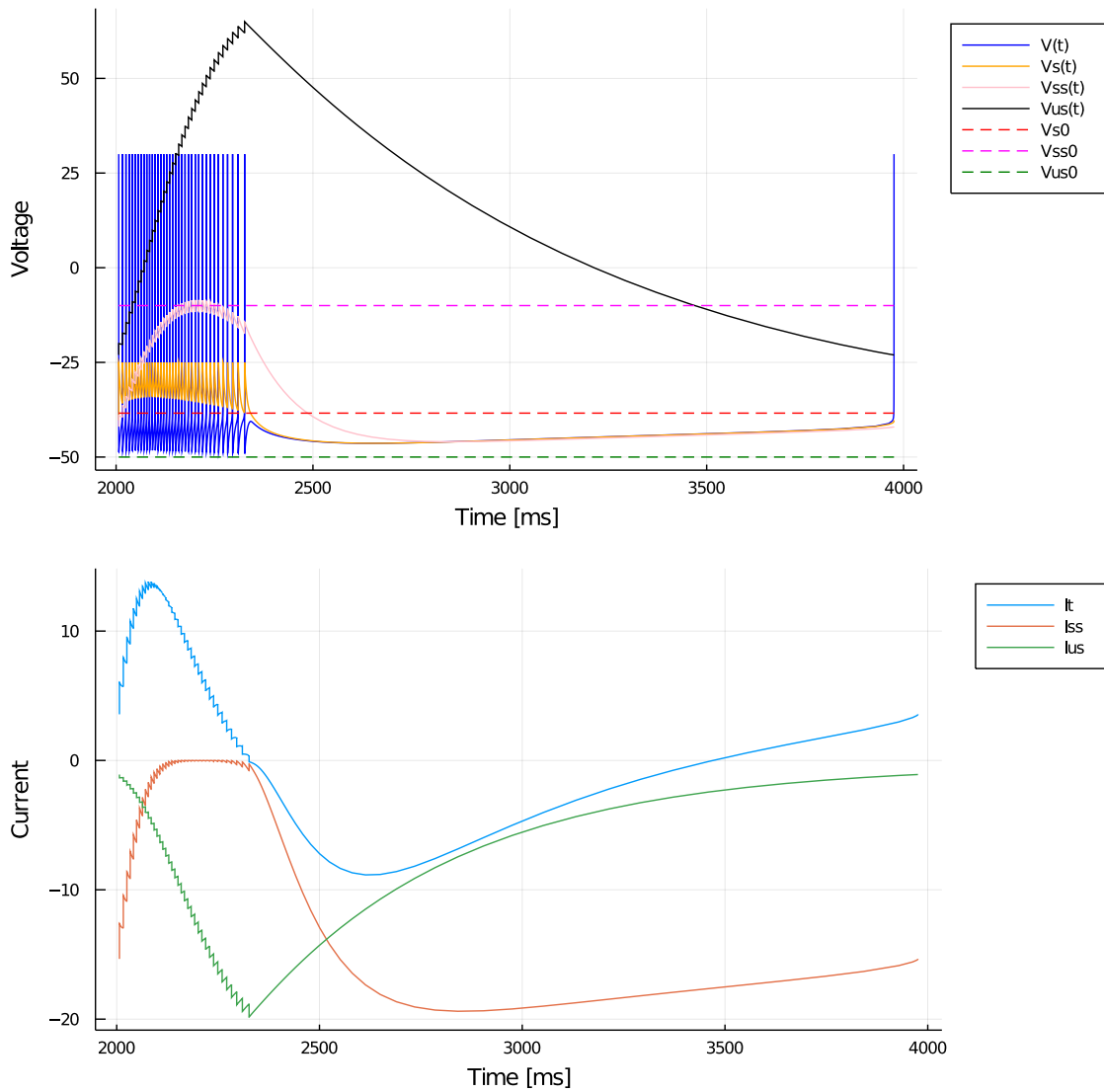
71

Figure 6.3.2: Zoom on a period of oscillations of Figure 6.3.1. The upper plot shows the evolution of the 4 potentials V, V_s, V_{ss} and V_{us} in response to an applied current of 20. The (fixed) values of the slow, super-slow and ultra-slow reference potentials are added as dashed lines. The lower plot shows the corresponding evolution of the total current in the equivalent 2D model. The corresponding super-slow and the ultra-slow currents are also represented to understand the shape of the total current.

the ultra-slow current increases. During this interval, the total current mostly follows the evolution of the super-slow current and increases. The instantaneous frequency increases accordingly.

Since the super-slow potential gets closer to its reference, the absolute value of super-slow current gets closer to 0. Thus, the super-slow current becomes negligible compared to the ultra-slow current. The ultra-slow potential increases as long as the cell potential spikes, which happens as long as the total current is still positive. Therefore, the ultra-slow current decreases. Since the super-slow current becomes negligible compared to the

ultra-slow current, the total current peaks and starts to decrease too. As the total current decreases, the instantaneous frequency of the spikes generated decreases. Accordingly, the evolution of the super-slow potential globally decreases. Indeed, as the time separating two spikes increases, the reset is applied less frequently which lets the gradient of V_{ss} act longer on its time evolution.

As the time constant of the ultra-slow feedback is very large, the decrease in the intraburst frequency does not prevent the ultra-slow potential from still increasing. The corresponding ultra-slow current decreases a lot, so does the total current. At some point, the total current becomes negative, the cell potential cannot spike anymore and the quiescent period begins. Since the reset cannot be applied anymore, all trajectories are driven by their gradient. As the super-slow potential evolution is characterized by a smaller timescale than the timescale of the ultra-slow potential, the super-slow potential moves away from its reference faster than the ultra-slow potential gets closer to its reference. Thus, absolute value of the super-slow current increases rapidly and both this current and the ultra-slow current become comparable. The corresponding evolution of the total current is a mix between these two currents.

The super-slow potential eventually reaches the same value as the cell potential. Indeed, the evolution of the super-slow potential is dictated by its gradient during the quiescent period. Among the 4 potentials, only the ultra-slow current has not reached the same value as the cell potential. Thus, the variation of the total current is mostly dictated by the variation of the ultra-slow current. Therefore, the total current increases, which also modifies the equilibrium of the cell potential in the equivalent 2D model. Additionally, the variation in the ultra-slow current implies an even slower variation in the super-slow current, which tends to move closer to its reference. Finally, the total current becomes positive, which involves a period of spike latency. The ultra-slow current has become negligible as it finally moved close enough to its reference. The total current keeps increasing as the super-slow potential follows the cell potential, which is slowly attracted towards spiking. Therefore, for the rest of the period of oscillations, the total current has approximately the same shape as the super-slow current.

6.3.2 Super-slow feedback impact on phase plane

Based on the analysis of the time response of the 4D MQIF, it is clear that the super-slow feedback has a major effect: for this set of conductances, it creates a sharp peak in the evolution of the total current applied in the equivalent 2D MQIF model during each period of oscillations. This peak allows a specific modulation of the intraburst frequency that was not observed in the 3D model presented in the previous chapter. Indeed, during the first half of the peak, the total current increases a lot. Accordingly, the time between two consecutive spikes in the burst decreases and the instantaneous frequency increases a lot. During the second half of the peak, the cell potential keeps spiking but it slows down: the intantaneous frequency decreases.

The change in the super-slow potential can also be seen as a change in the size of the excitability well in the 3D phase plane, represented in the space $(V; V_{us}; V_s)$. Indeed, as we considered the total current I_t in the equivalent 2D model we can consider a total current $I_{t_{3D}}$ in the equivalent 3D model. Its mathematical expression would be:

$$I_{t_{3D}} = I_{\text{app}} - \bar{g}_{ss}(V_{ss} - V_{ss}^0)^2.$$

73

Therefore, the analysis of the impact of the super-slow feedback on the equivalent 3D model is similar to the analysis of the impact of the ultra-slow feedback on the equivalent 2D model, with an additional dimension. As the super-slow potential is able to change the applied current in the equivalent 3D model, and that this current mostly impacts the size of the excitability well, the super-slow feedback simply modifies the size of the excitability well and is able to make it disappear. Figures 6.3.3 to 6.3.5 show the V nullcline of the equivalent 3D model with a total current $I_{t_{3D}}$ in the space $(V; V_{us}; V_s)$ (left) and the corresponding value of V_{ss} taken from the simulation shown in Figure 6.3.2 (right) at 3 different locations in the time interval associated with a period of bursting. These figures show that the excitability well is modified by the value taken by the super-slow potential. For a more comprehensive view of the evolution of the V nullcline during a period of bursting, please check the video these figures are extracted from. The serrated look of the V nullcline that may appear for positive V_{us} and low V_{ss} is due to approximation errors. In reality, the total current in the equivalent 2D model is negative at these locations and the V nullcline separates into a left and a right part, while it separates into a upper and a lower part when the total current in the 2D model is positive, meaning that the excitability well separates the upper and the lower parts.
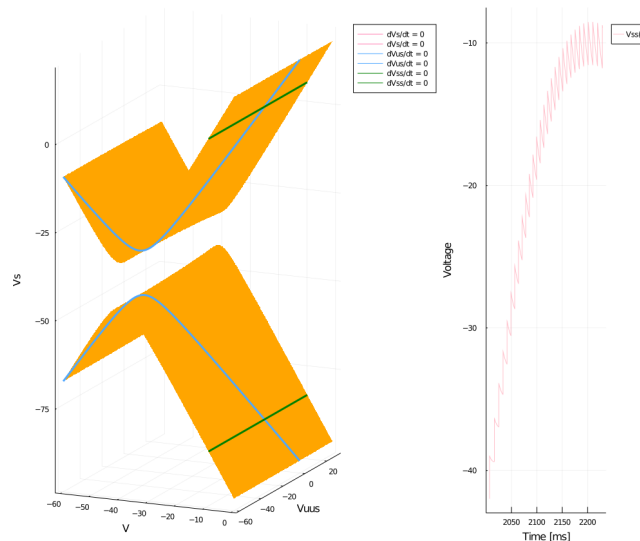

Figure 6.3.3: Screenshot of the video realized to show the evolution of the V nullcline in the space $(V; V_{us}; V_s)$ (left) for a given value of super-slow potential (right), which is taken from the response of the 4D model to a constant applied current shown in Figure 6.3.2. The intersections of the hyperplanes defined by the V_s, V_{ss} and V_{us} nullclines with the V nullclines are shown respectively as pink, green and blue lines. The value taken by the super-slow potential is the last value shown in the right plot. In this case, this value is chosen near its maximum.

To support the reasoning realized on the observed behavior of the 4D model in response to a constant current, it is interesting to consider both the evolution of the equivalent 2D phase plane and the evolution of the size of the excitability well across a period of oscillations. For a clarity purpose, the excitability well is projected into the 2D space $(V_{us}; V_s)$, which is actually a side view of the 3D space presented in Figures 6.3.3 to 6.3.5. Once again, the associated video is much more helpful, compared to the figures extracted from it, to understand how bursting with a modulated instantaneous frequency

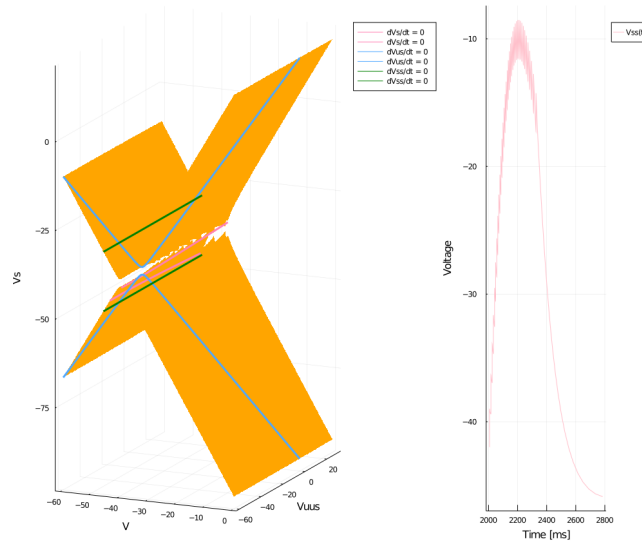Figure 6.3.4: Screenshot of the video realized to show the evolution of the V nullcline in the space $(V; V_{us}; V_s)$ (left) for a given value of super-slow potential (right), which is taken from the response of the 4D model to a constant applied current shown in Figure 6.3.2. The intersections of the hyperplanes defined by the V_s, V_{ss} and V_{us} nullclines with the V nullclines are shown respectively as pink, green and blue lines. The value taken by the super-slow potential is the last value shown in the right plot. In this case, this value is chosen near its minimum.
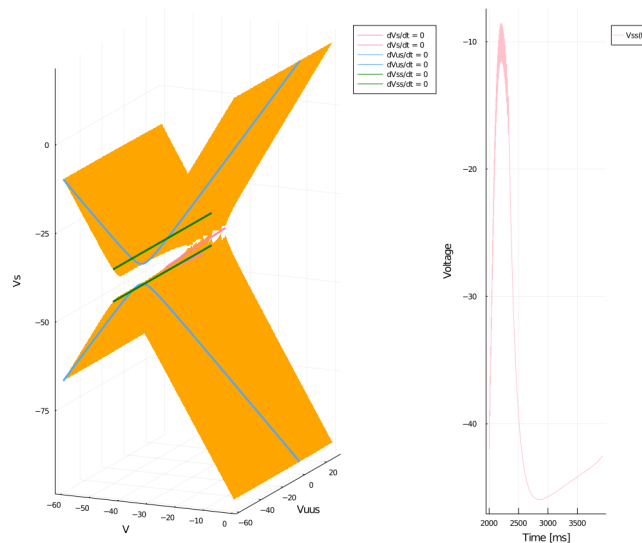

Figure 6.3.5: Screenshot of the video realized to show the evolution of the V nullcline in the space $(V; V_{us}; V_s)$ (left) for a given value of super-slow potential (right), which is taken from the response of the 4D model to a constant applied current shown in Figure 6.3.2. The intersections of the hyperplanes defined by the V_s, V_{ss} and V_{us} nullclines with the V nullclines are shown respectively as pink, green and blue lines. The value taken by the super-slow potential is the last value shown in the right plot. In this case, this value is chosen near the beginning of the next train of spikes.

is generated. The screenshots of this video are found in Figures 6.3.6 to 6.3.8. Each of these figures is separated into 4 plots. Plots B and D are similar to Figure 6.3.2 as they represent respectively the evolution of the 4 potentials and the evolution of the corresponding total current in the equivalent 2D model from the beginning of the period of oscillations to the timestep considered. Plot A represents the phase plane of the equivalent 2D model that is computed based on the last value taken by the total current at the considered timestep in plot D. The trajectory of the 4D model is represented in the space $(V; V_s)$ to see its evolution in this phase plane. To have a better view of the position of the timestep in the period considered, a color gradient is added to characterize the system trajectory in plots A and C. Finally, plot C shows the evolution of the system trajectory (following the same color gradient as plot A) projected in the space $(V_{us}; V_s)$ around the projection of the excitability well.

These figures also support the analysis realized before and combine some observations realized in the study of the 2D model and of the 3D model. The size of the excitability well is clearly modulated by V_{ss}. Also, the side view of the excitability well is helpful to understand how the trajectory evolves in the 3D phase plane. In fact, a spike is generated as soon as the system finds its way back to this well. When the applied current is positive, the system organizes itself around the tip of the excitability well, around a total current in a range of values near 0.
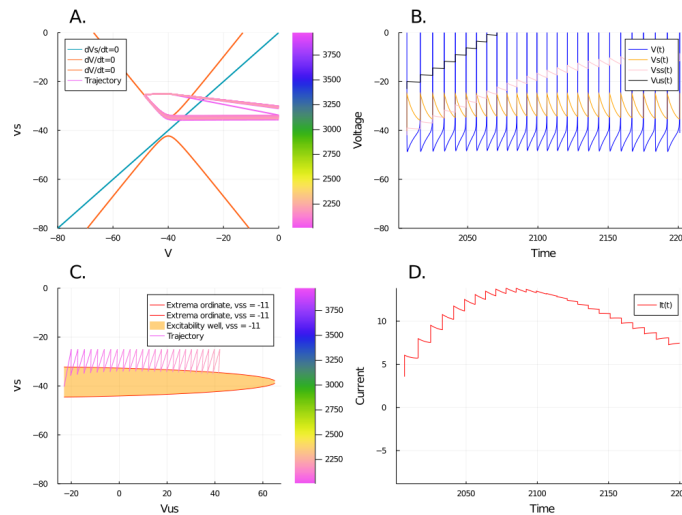

Figure 6.3.6: Screenshot of the video realized to show the evolution of the 4D model response to a constant current in the 2D equivalent phase plane (A.) and around the projection in $(V_{us}; V_s)$ of the excitability well (C.) that is found in the V nullcline in the space $(V; V_{us}; V_s)$. The evolution of the 4 potentials V, V_s, V_{ss} and V_{us} between the beginning of the period and the considered timestep are represented in B., while the corresponding evolution of the total current is represented in D. In parts A. and C., each projected trajectory is associated to a color gradient defined on the full duration of the period of oscillations. The value of V_{ss} that corresponds to the timestep considered can be found in the legend of C.
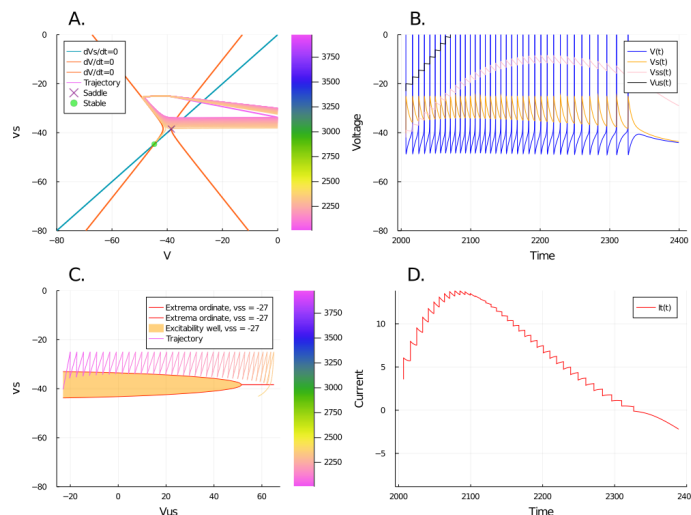
Figure 6.3.7: Screenshot of the video realized to show the evolution of the 4D model response to a constant current in the 2D equivalent phase plane (A.) and around the projection in $(V_{us}; V_s)$ of the excitability well (C.) that is found in the V nullcline in the space $(V; V_{us}; V_s)$. The evolution of the 4 potentials V, V_s, V_{ss} and V_{us} between the beginning of the period and the considered timestep are represented in B., while the corresponding evolution of the total current is represented in D. In parts A. and C., each projected trajectory is associated to a color gradient defined on the full duration of the period of oscillations. The value of V_{ss} that corresponds to the timestep considered can be found in the legend of C.

6.4 Bifurcation study

6.4.1 Bifurcation of the full system with constant current

Similarly to the previous models, the 4D MQIF model shows a saddle-node bifurcation, as represented in Figure 6.4.1. The maximum value of the cell potential during the oscillations is not represented as it is simply defined by the reset. Therefore, it is constant with a change in applied current. The shape of the bifurcation diagram is close to what was observed for the 3D model. Even if this bifurcation diagram supports the value chosen for the constant applied current in the presented simulations, the detailed shape of this bifurcation diagram may depend on the conductances values. However, based on the previous results and on the mathematical developments realized, we assume that the saddle-node bifurcation is observed for any set of conductances.

Due to the modulation of the total current during the burst realized by the super-slow feedback, the intraburst frequency is modified. Figure 6.4.2 shows that the instantaneous frequency during the burst clearly follows the variation in total current.

Finally, we can analyze the evolution of the interburst frequency for a change in applied current. Above the value at which the saddle-node bifurcation occurs, the interburst frequency slightly increases. Moreover, the number of spikes in each burst seems to decrease with an increasing applied current. These two results are consistent with what was observed for the 3D model.
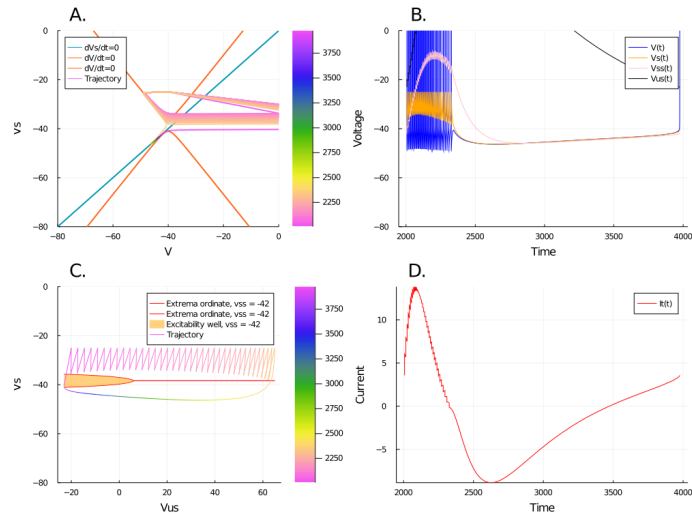
Figure 6.3.8: Screenshot of the video realized to show the evolution of the 4D model response to a constant current in the 2D equivalent phase plane (A.) and around the projection in $(V_{us}; V_s)$ of the excitability well (C.) that is found in the V nullcline in the space $(V; V_{us}; V_s)$. The evolution of the 4 potentials V, V_s, V_{ss} and V_{us} between the beginning of the period and the considered timestep are represented in B., while the corresponding evolution of the total current is represented in D. In parts A. and C., each projected trajectory is associated to a color gradient defined on the full duration of the period of oscillations. The value of V_{ss} that corresponds to the timestep considered can be found in the legend of C.
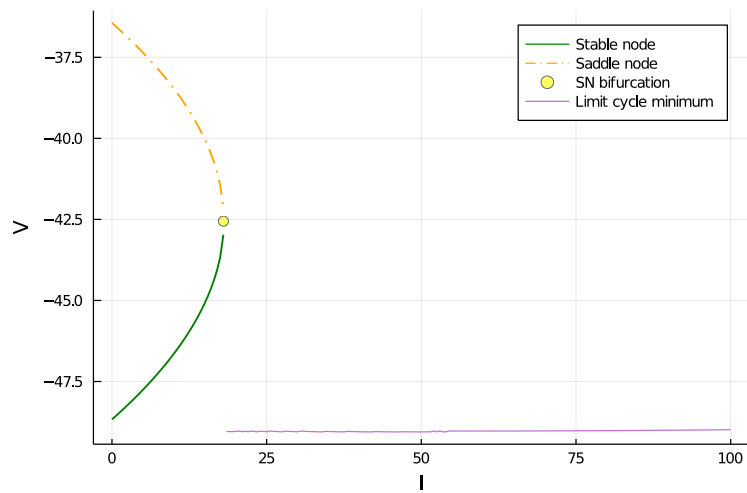

Figure 6.4.1: Bifurcation diagram of the 4D model with the applied current. The location of the saddle-node bifurcation is highlighted by the yellow marker. The V coordinates of the stable and the saddle nodes are reported in this diagram. The minimum value of the cell potential during the oscillations is also represented.

6.4.2 Impact of a change in conductances

The set of conductances chosen for the simulations has a large impact of the behavior of the model. In fact, conductances allow to scale the impact of each feedback, notably on the total current in the equivalent 2D model, which in term impacts the entire pattern.
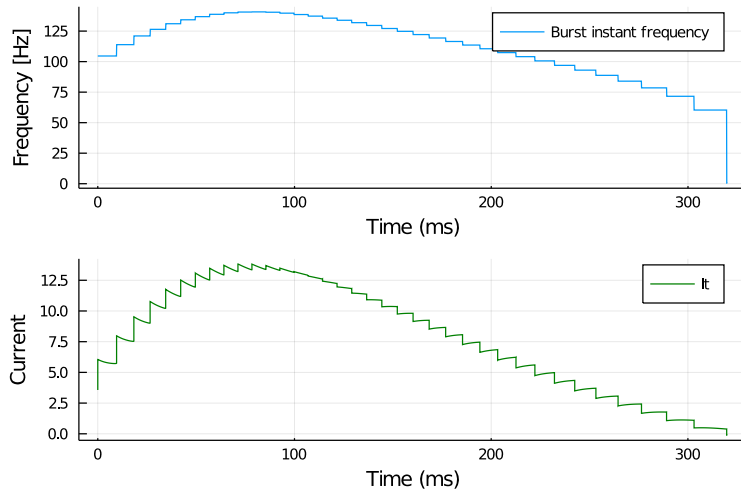
78

Figure 6.4.2: Evolution of the instantaneous frequency during the burst shown in Figure 6.3.2 (up) and the corresponding evolution of total current (down).
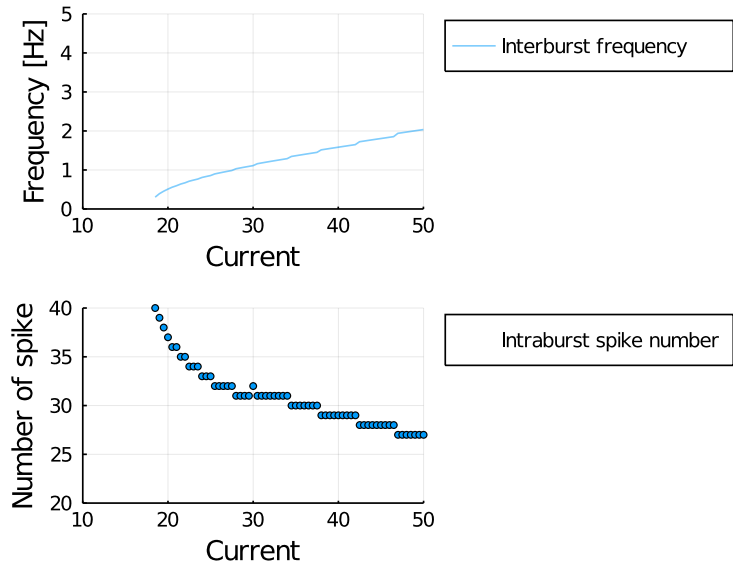

Figure 6.4.3: Evolution of the average frequency of oscillations (interburst frequency) during a period of oscillations with the applied current (up) and the corresponding evolution of the number of spikes during each burst (down).

Thus, other patterns than bursting can be observed. For example, we further reduced the ultra-slow conductance by a factor 10 and observed a limit cycle that does not contain any quiescent period. This behavior of the model is represented in Figure 6.4.4 and the associated set of conductances can be found in Table 6.2. The applied current used for this simulation is still 20, as the change in ultra-slow conductance compared to its value in the previous simulation has barely no impact on the bifurcation current of this model.

The disappearance of the quiescent periods in Figure 6.4.4 is consistent with the set of conductances used. Indeed, the conductance of the ultra-slow feedback being much smaller than the other conductances, the ultra-slow feedback has barely no impact on the model
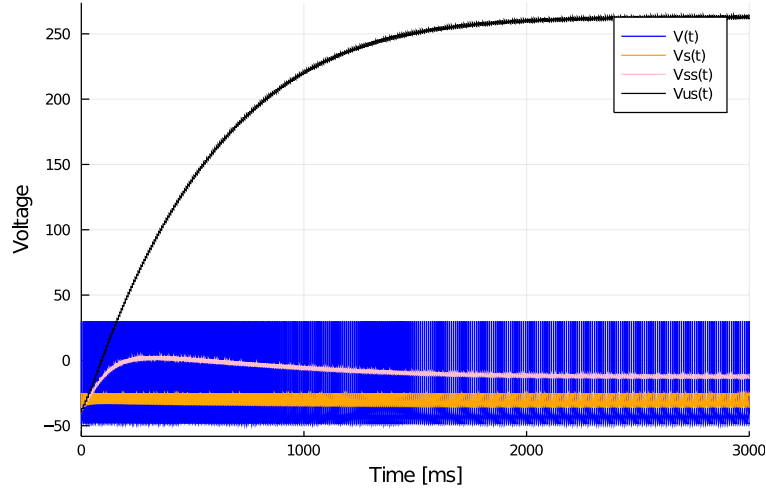
Figure 6.4.4: Time responses of the 4D MQIF model to a constant current of 20. The set of conductances used for this simulation can be found in Table 6.2. The upper plot shows the evolution of the 4 potentials V, V_s, V_{ss} and V_{us}. The lower plot shows the corresponding evolution of the total current in the equivalent 2D model.

$\bar{g}_f$	$\bar{g}_s$	$\bar{g}_{ss}$	$\bar{g}_{us}$
1	0.5	0.015	0.00015

.

Table 6.2: Conductances used to simulate Figure 6.4.4

response. Thus, the super slow regenerative feedback dominates in the model response.

Since the 4D MQIF model shows already two very distinct behaviors for a constant current, it is expected that the model response to a pulse of current may be very different depending on the set of conductances chosen. Indeed, a change in the set of conductances may have a big impact on the bifurcation current. To simulate the response of the model to a pulse of applied current, the baseline (I_l) and the value taken by the current during the pulse (I_h) must be chosen based on the set of conductances considered. In Figure 6.4.5, we can observe the impact of a variation in each conductance on the value at which the saddle-node bifurcation occurs in the 4D model phase plane. The applied current needed to overcome this bifurcation and to observe another behavior than a convergence towards a stable state increases as each conductance increases. A non-linearity occurs in the left part of this figure as the slow conductance gets too close to the fast conductance. Indeed, based on equation (6.2.2), the value of applied current at which the stable and the saddle nodes collide is:

$$I_{\text{bif}} = \frac{\bar{g}_f \bar{g}_s \left(V^0 - V_s^0\right)^2 + \bar{g}_f \bar{g}_{ss} \left(V^0 - V_{ss}^0\right)^2 + \bar{g}_f \bar{g}_{us} \left(V^0 - V_{us}^0\right)^2}{\bar{g}_f - \bar{g}_s - \bar{g}_{ss} - \bar{g}_{us}}$$

$$- \frac{\bar{g}_s \bar{g}_{ss} \left(V_s^0 - V_{ss}^0\right)^2 + \bar{g}_s \bar{g}_{us} \left(V_s^0 - V_{us}^0\right)^2 + \bar{g}_{ss} \bar{g}_{us} \left(V_{ss}^0 - V_{us}^0\right)^2}{\bar{g}_f - \bar{g}_s - \bar{g}_{ss} - \bar{g}_{us}}$$

6.4.3 Types of firing patterns

According to the definition of the DHNs firing pattern (observed in Figure 3.3.2 and modeled by Le Franc et al. in Figures 3.5.3 and 3.5.4), we must simulate either a pulse of
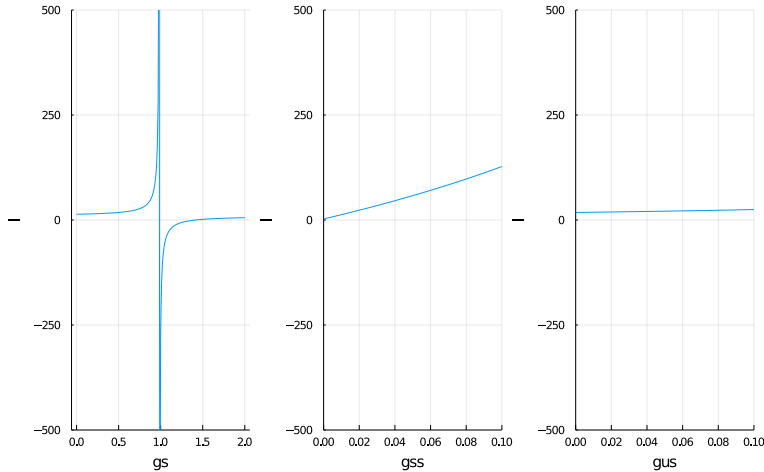
Figure 6.4.5: Evolution of the bifurcation current with the conductances $\bar{g}_s$ (left), $\bar{g}_{ss}$ (center) and $\bar{g}_{us}$ (right). As only one conductance varies per plot, the set of conductances from which the fixed conductances are extracted is given in Table 6.1.

applied current to observe tonic firing, plateau potentials and the accelerating behavior.

To account for the change in conductances when choosing the value of applied current, we simulate the evolution of the maximum and the minimum of the total current for a given range of applied current. Based on the behavior of the 2D equivalent MQIF model for the corresponding range of total current, we can find the values of applied current under which the total current is negative and above which the range of total current is higher than the value of the saddle-node bifurcation in the equivalent 2D model. Using this method, we ensure that the baseline and the highest current associated to the pulse of applied current are located at the beginning and the end of the bistable area associated to the 2D equivalent model. For the set of conductance in Table 6.2, Figure 6.4.6 shows the position of the two values of applied current I_l and I_h that are optimal to stay around the limit of the 2D bistable regime, shown in yellow. The green and the blue areas represent respectively the ranges where the applied current chosen induces a total current at equilibrium that corresponds to a stable state or to a limit cycle in the equivalent 2D model.

Consistently with the evolution of the bifurcation current of the 4D model with a change in conductances, Figure 6.4.7 shows that the current I_l and I_h, at the limits of the area in which bistability is observed in the equivalent 2D model, increase with an increasing ultra-slow conductance (left) or an increasing super-slow conductance (right).

Based on the methodology explained to choose the value of the baseline of the applied current and its value during the pulse, we achieved to simulate both plateau potentials and tonic firing. The set of conductances used to simulate these patterns are found in Tables 6.3 and 6.4 respectively. Consistently with the previous discussions, tonic firing is observed when the impact of the super-slow and the ultra-slow feedback is very weak and plateau potentials are observed when the super-slow regenerative feedback has a greater impact than the ultra-slow feedback.

Plateau potentials and tonic firing are represented in Figures 6.4.8 and 6.4.9 respectively. In each figure, the three lower plots are a zoom of the three upper plots around the pulse
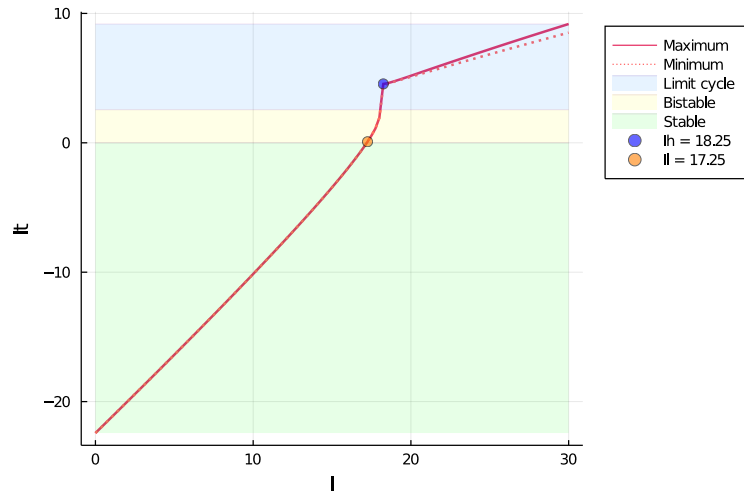
Figure 6.4.6: Methodology used to define the currents I_l, associated with the baseline of the pulse of current at first, and I_h, the maximum value of the pulse. The applied current is varied to compute the total current in the equivalent 2D model and its associated behavior. The currents I_l and I_h are the values of applied current that correspond respectively to the end of the stable regime and the beginning of the cyclic regime.
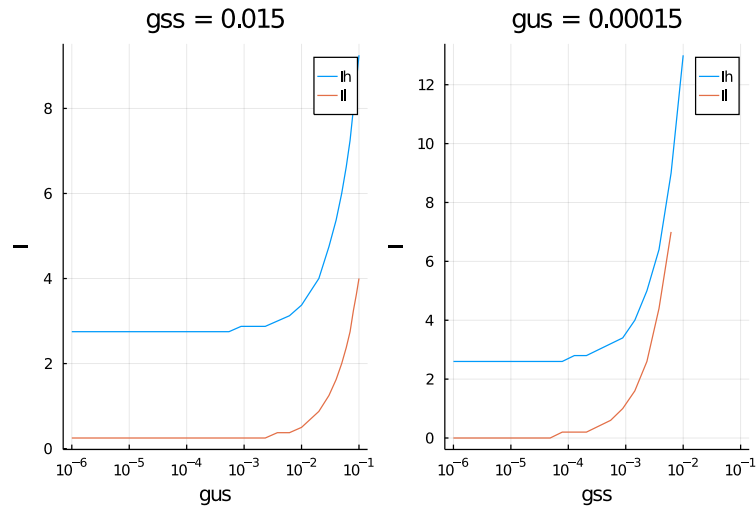

Figure 6.4.7: Evolution of the currents I_h and I_l used to define the pulse of current with a change in the ultra-slow conductance for a fixed $\bar{g}_{ss}$ (left) or in the super-slow conductance or a fixed $\bar{g}_{us}$.

of applied current. Starting from the top of each figure, the first and fourth plots show the evolution of the applied current across time and the evolution of the total current in the 2D model, which is computed from the voltage traces. In dotted line, the current at which the saddle-node bifurcation occurs in the 2D model is represented. This value only depends on the fast and slow parameters as explained during the mathematical analysis of the 2D MQIF equations. The second and the fifth plots show the evolution of the potentials V, V_s, V_{ss} and V_{us}. Finally, the third and sixth plots show the evolution of the instantaneous frequency, as long as spikes are generated.
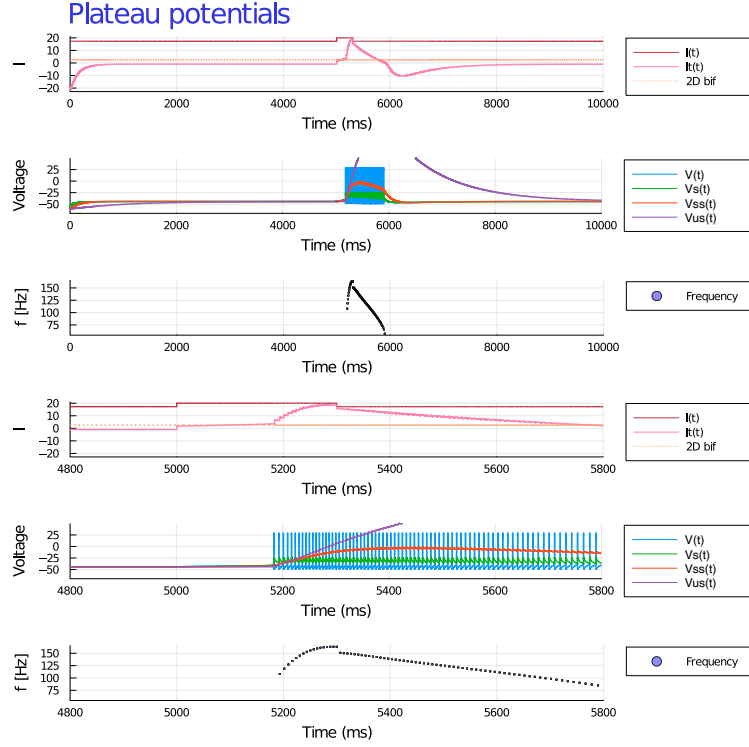
Figure 6.4.8: Simulation of plateau potentials. The three lower plots are a zoom on the three upper plots respectively around the time interval where the pulse is applied. Starting from the top, the first and fourth plots show the evolution of the applied current (red), the total current computed based V_{ss} and V_{us} (pink) and the value of the bifurcation current in the equivalent 2D model (dotted line). The second and fifth plots show the evolution of the potentials. The third and sixth plots represent the evolution of the instantaneous frequency. The currents chosen for the baseline and the maximum value for the pulse of applied current are chosen based on the methodology shown in Figure 6.4.6. The duration of the pulse is 300 ms. The parameters used for this simulation can be found in Table 6.3.

$\bar{g}_f$	$\bar{g}_s$	$\bar{g}_{ss}$	$\bar{g}_{us}$
1	0.5	0.0155	0.0005

.

Table 6.3: Conductances used to simulate Figure 6.4.8

$\bar{g}_f$	$\bar{g}_s$	$\bar{g}_{ss}$	$\bar{g}_{us}$
1	0.5	0.0001	0.00001

.

Table 6.4: Conductances used to simulate Figure 6.4.9

The duration of each pulse of applied current is 300 ms. This arbitrary value is chosen so that plateau potentials are easily observed in the model response to a pulse of current. The baseline of the current is set to the floor value of I_l while the value of the current during the pulse is set to the ceil value of I_h plus one for each set of conductances. Once again, the choice to approximate up and down the upper and the lower boundary of the bistable area helped to see easily plateau potentials in the model response.
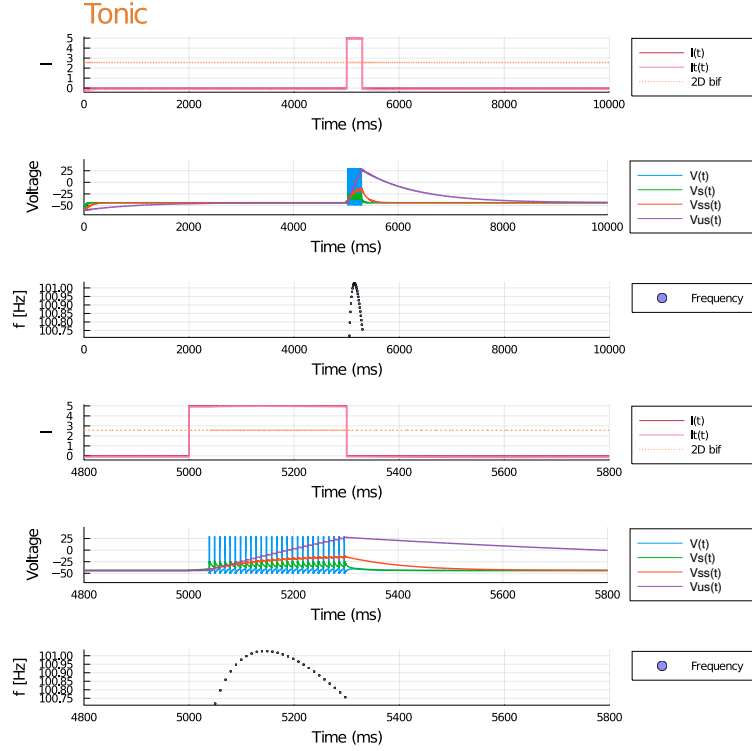
83

Figure 6.4.9: Simulation of tonic firing. The three lower plots are a zoom on the three upper plots respectively around the time interval where the pulse is applied. Starting from the top, the first and fourth plots show the evolution of the applied current (red), the total current computed based V_{ss} and V_{us} (pink) and the value of the bifurcation current in the equivalent 2D model (dotted line). The second and fifth plots show the evolution of the potentials. The third and sixth plots represent the evolution of the instantaneous frequency. The currents chosen for the baseline and the maximum value for the pulse of applied current are chosen based on the methodology shown in Figure 6.4.6. The duration of the pulse is 300 ms. The parameters used for this simulation can be found in Table 6.4

However, the accelerating behavior is hard to observe with this methodology. In fact, it is the baseline of the applied current that raises this issue. Indeed, the switch in the applied current value at the end of the pulse must be close enough to 0 to prevent the model from generating spikes after the pulse. If it is not the case, the system might oscillate forever, leading to an unstable behavior. Thus, to observe the accelerating firing, we simulated a fixed value for the baseline of applied current of 0.5. The maximum of the current is kept near the upper boundary of the bistable area. Figure 6.4.10 shows the accelerating behavior, following the same organization as Figures 6.4.8 and 6.4.9.

$\bar{g}_f$	$\bar{g}_s$	$\bar{g}_{ss}$	$\bar{g}_{us}$
1	0.5	0.008	0.00015

.

Table 6.5: Conductances used to simulate Figure 6.4.10

The three behaviors represented in Figures 6.4.8 to 6.4.10 in response to a pulse of applied current emanate from the same behavior of the model with a constant current, shown in Figure 6.4.4. This behavior tends to a limit cycle with no quiescent period.
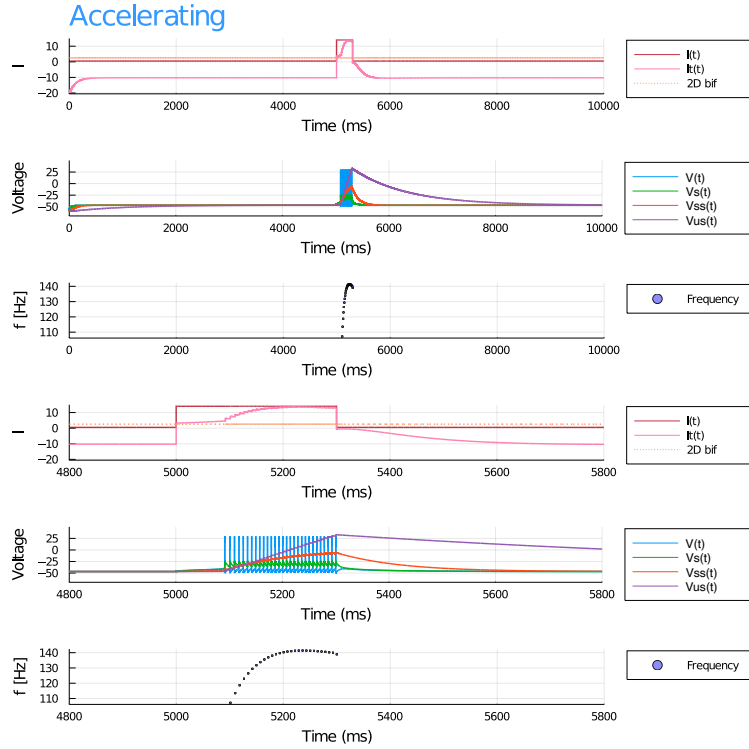
84

Figure 6.4.10: Simulation of accelerating firing. The three lower plots are a zoom on the three upper plots respectively around the time interval where the pulse is applied. Starting from the top, the first and fourth plots show the evolution of the applied current (red), the total current computed based V_{ss} and V_{us} (pink) and the value of the bifurcation current in the equivalent 2D model (dotted line). The second and fifth plots show the evolution of the potentials. The third and sixth plots represent the evolution of the instantaneous frequency. The currents chosen for the baseline and the maximum value for the pulse of applied current are chosen based on the methodology shown in Figure 6.4.6. The duration of the pulse is 300 ms. The parameters used for this simulation can be found in Table 6.5.

However, the instantaneous frequency at which each spike is generated varies a lot at the beginning of the simulation. This modulation of the frequency matches the variation in instantaneous frequency observed during the pulse. In figure 6.4.4, it can be seen that the instantaneous frequency shows a maximum at the beginning of the simulation. Indeed, the time separation between two spikes decreases during the first hundred of milliseconds and increases afterwards. The strength of the super-slow and the ultra-slow feedbacks modulate the amplitude and the sharpness of this peak of instantaneous frequency. This allows a flat variation in frequency during the pulse for tonic spiking and a globally increasing instantaneous frequency for plateau potentials during the burst. Finally, it is interesting to note that an increasing strength of the super-slow regenerative feedback increases the spike latency observed in the model response during the burst.

As explained, it is rare to observe the accelerating behavior in the model response when the baseline of the applied current is high. The choice of currents for the pattern of applied current has a large impact on the model response actually. Indeed, in Figure 6.4.11, we represented a scatter plot in which the color of the dots corresponds to a defined behavior observed in the model response to a pulse of current for the values $(I_l; I_h)$ chosen for the

baseline and the highest value of current during the pulse. The set of conductances chosen is the same as in Table 6.2.
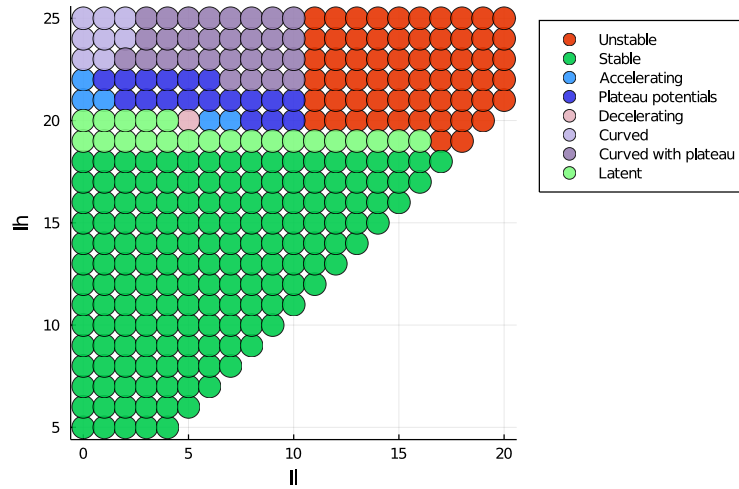

Figure 6.4.11: Mapping of the firing pattern observed for the set of currents chosen for the baseline and the maximum of the pulse of applied current. Each color corresponds to one type of firing pattern. These patterns are simulated for a pulse duration of 300 ms. The set of conductances used is given in Table 6.2.
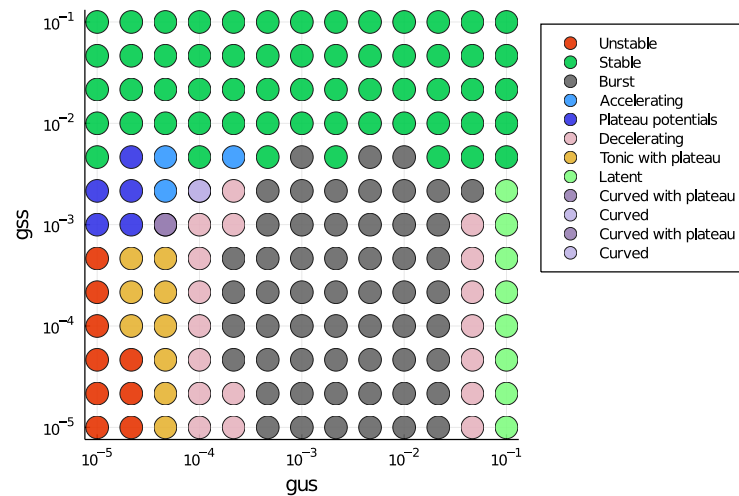

Figure 6.4.12: Mapping of the firing pattern observed for the set of conductances $(g_{ss}; g_{us})$ chosen. Each color corresponds to one type of firing pattern. These patterns are simulated for a pulse duration of 300 ms. The baseline of the applied current is set to 0.5 while its value during the pulse is not fixed and follow the methodology explained to find I_h related to Figure 6.4.6. The slow conductance is set to 0.5.

In this figure, we can clearly see that not only bursting, tonic firing, plateau potentials and the accelerating behavior can be observed. To see all types of patterns in response to a pulse of current that can be generated with the 4D MQIF model, we can change the slow, the super-slow and the ultra-slow conductances. In Figures 6.4.12 and 6.4.13, we
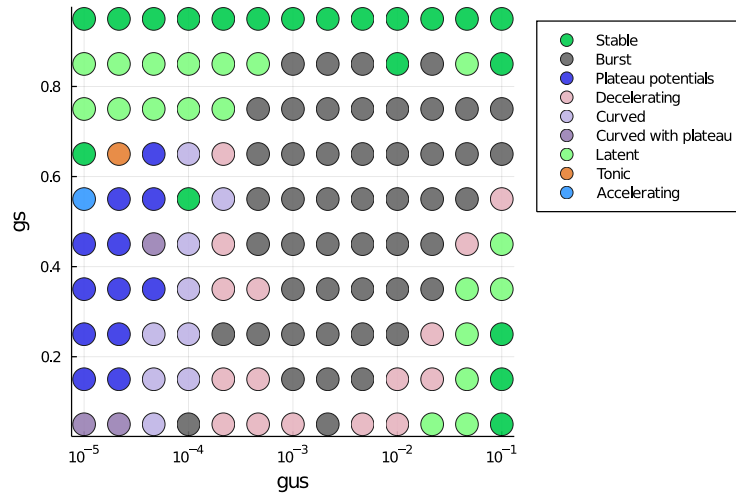
Figure 6.4.13: Mapping of the firing pattern observed for the set of conductances $(g_s; g_{us})$ chosen. Each color corresponds to one type of firing pattern. These patterns are simulated for a pulse duration of $300\,\text{ms}$. The baseline of the applied current is set to 0.5 while its value during the pulse is not fixed and follow the methodology explained to find I_h related to Figure 6.4.6. The super-slow conductance is set to 0.002.

present a mapping of the behaviors of the model in response to a pulse of current with a maximum value I_h and a baseline of 0.5 for a given set of $(\bar{g}_{ss}; \bar{g}_{us})$ with a fixed $\bar{g}_s$ or a set of $(\bar{g}_s; \bar{g}_{us})$ with a fixed $\bar{g}_{ss}$ respectively. Besides the firing patterns of the DHNs described in the literature, 8 others behaviors can be observed:

- "Stable": As the range of applied current used to find the limits of the bistable area for a corresponding total current in the equivalent 2D model has its limits, the maximum value of the current during the pulse may stay under the bifurcation current of the 4D model associated to the set of conductance chosen. Thus, the total current during the simulation is always negative and no spike is generated by the model. A simulation of this firing pattern can be observed in Figure A.2.1 in the Appendix.

- "Latent": The duration of the pulse of applied current is fixed. Therefore, for high values of conductances, the maximum of the applied current may be too low to overcome the spike latency induced by the model. Thus, the behavior observed in response to a pulse of current seems at equilibrium and no spike is generated by the model.

- "Unstable": As explained to justify the change in the value of the baseline of applied current, the model may sometimes keep on spiking after the end of the pulse and may not stop. This behavior is the "unstable" behavior. A simulation of this firing pattern can be observed in Figure A.1.1 in the Appendix.

- "Tonic with plateau": This type of behavior is similar to tonic spiking during the pulse. Indeed, the variation in instantaneous frequency is lower than 2% of the maximum instantaneous frequency during the pulse. However, the cell potential at the end of the pulse contrasts with tonic spiking. Indeed, this behavior shows an afterdischarge. A simulation of this firing pattern can be observed in Figure A.3.1 in the Appendix.

87

- "Decelerating": As the frequency increases for the accelerating behavior, for some sets of conductances we were able to observe a globally decreasing frequency during the pulse that is not associated to bursting for a simulation of a constant current. This type of behavior is associated to a change in instantaneous frequency of more than 2% of the maximum frequency during the pulse. Moreover, another condition set to define this behavior is that the maximum instantaneous frequency during the pulse must be reached in the first third of the time interval in which the model spikes during the pulse. This criterion is set so that we do not take into account a possible spike latency to classify the pattern observed. A simulation of this firing pattern can be observed in Figure A.4.1 in the Appendix.

- "Decelerating with plateau": A pattern is classified as plateau potentials or as an accelerating behavior depending on the presence of spikes after the pulse. This distinction is similar to the distinction between "decelerating" and "decelerating with plateau". Indeed, the latter has the same characteristics as the "decelerating" behavior during the pulse but it shows an additional afterdischarge.

- "Curved": The criterion on the position of the maximum instantaneous frequency during the burst is also applied to the accelerating behavior. Indeed, a pattern is classified as accelerating if the maximum frequency during the pulse is located after the second third of the time interval where spiking is observed during the pulse. By continuity, the pattern is classified as "curved" when the location of the maximum frequency is around the middle of the time interval where the cell potential spikes during the pulse. The period during which the frequency increases has almost the same duration as the period during which the frequency decreases. A simulation of this firing pattern can be observed in Figure A.5.1 in the Appendix.

- "Curved with plateau": In parallel to the distinction between plateau potentials and the accelerating behavior or between the "decelerating with plateau" and "decelerating" behaviors, the behavior "curved with plateau" has a maximum frequency around the middle of the time interval where the cell potential spikes during the pulse but also shows an afterdischarge after the pulse.

Now that all types of firing patterns observed are defined, we can further analyze Figure 6.4.11. Two features of the model can be observed. First, for an fixed low baseline of the current and an increasing value of current during the pulse, provided that the latter is greater than the bifurcation current, the firing pattern switches from accelerating/plateau potentials to "curved"/"curved with plateau". In fact, if we choose a higher maximum for the applied current, the total current at the transition between the baseline and this maximum is much higher. Indeed, as the system is at equilibrium before the pulse, the super-slow and ultra-slow potentials are very far from their reference. Thus, the peak in instantaneous frequency is higher and occurs sooner if the maximum value of the applied current is increased. Second, we can see in Figure 6.4.11 that when the baseline of the applied current is too high, the only firing pattern observed is an unstable behavior, provided that the maximum of the applied current during the pulse is high enough to observe another behavior than a stable or a "latent" one. This effect is observed for various sets of conductances. This further supports that a low value of the baseline is suited to observe all firing patterns.

Finally, Figures 6.4.12 and 6.4.13 further support that the relative strengths of the slow, super-slow and ultra-slow feedback set the behavior of the model in response to a pulse

of current. Using the definition of all types of firing patterns observed, we can see that the firing pattern tends to slow down when the conductance of the ultra-slow restorative feedback increases. Indeed, in each line of these scatter plots, the behaviors from low to high $\bar{g}_u$s are characterized respectively by increasing or maintained instantaneous frequency during the pulse to decreasing instantaneous frequency during the pulse. Also, it can be seen that an increase in the super-slow regenerative conductance tends to accelerate the instantaneous frequency during the pulse. However, increasing this conductance induces an increase in the bifurcation current and this may give rise to "latent" or "stable" behaviors if the maximum value of the applied current cannot follow this increase. Indeed, an applied current greater but too close to the bifurcation implies a long spike latency, which can be longer than the pulse duration. In Figure 6.4.13, an increase in the slow conductance seems to slow down the system during the pulse. This may seem counter-intuitive since this feedback is regenerative, just as the super-slow feedback. However, the slow conductance has a large impact on the bifurcation current. We assume that the decrease in frequency may be mainly due to the large impact of the slow conductance on the bifurcation current. Indeed, this slow down reminds us of the behaviors of the 2D model observed for a varying $\bar{g}_s$ that are shown in Figure 4.4.8.

6.5   Summary

In this chapter, we showed that all DHNs firing patterns can be modeled using a slow regenerative, a super-slow regenerative, and an ultra-slow restorative feedback. We also showed that each firing pattern is obtained for different strengths of feedbacks. Tonic firing is obtained when the super-slow and the ultra-slow feedbacks have a reduced impact on the system. Bursting is obtained when the ultra-slow feedback is non-negligible. However, an additional weak super-slow regenerative feedback is able to modulate the intraburst frequency. Finally, plateau potentials and the accelerating behavior need a non-negligible super-slow feedback and a negligible ultra-slow conductance.

As much as the conductances impact the behavior of the model, the current seems to play an important role in the responses observed. Indeed, even if the 4D model's fixed points and the frequency evolution with the current are consistent with what is observed in the analysis of the 3D model, the fact that the current used, in particular to simulate a pulse, has a large impact on the firing patterns complexifies their analysis. A methodology in which the maximum applied current is chosen near the boundary between the bistable and the limit cycle regime is presented. The baseline of the current is also very important and impacts a lot the firing patterns observed.

Finally, we showed that the 4D MQIF model is able to show other firing patterns that are a continuity of the 4 DHNs firing patterns. Each of them is presented and the criteria used to classify them are also explained.

Chapter 7

Conclusion and Perspectives

Previous work realized by Le Franc et al. gave order of magnitude of the timescales of the mechanisms involved in the DHNs excitability. These mechanisms were split into 4 groups: fast, slow, super-slow and ultra-slow feedbacks. This motivated the incremental approach used to study the 4D MQIF model. First, we studied the behavior of the 2D model and analyzed the impact of the feedback nature on the phase plane and on the time responses. This study showed that specific properties such as bistability, spike latency and afterdepolarization potential, involved in neurons that are well represented by a calcium dynamic, can be modeled by a slow regenerative feedback. The nature of the slow feedback was shown to determine the excitability of the model. A restorative slow feedback does not induce particular properties such as bistability, among others, but allows to always come back to a stable equilibrium when there is no more input perturbation. We therefore chose the slowest feedback to be restorative in the final model, so that it could always converge back to a resting state.

The study of the 2D model and its behavior was the basis of the analysis of the behavior of the 3D model. This model showed the importance and the impact of the ultra-slow restorative feedback to generate bursting. Having a slow regenerative and an ultra-slow restorative feedbacks, the response to input pulses of applied current and the bifurcation diagram of the 3D model did not show specific properties such as bistability but were not similar to the results obtained with a slow restorative feedback neither. The slow regenerative feedback in the 3D model modulates the generation of a train of spikes that is also called burst. The ultra-slow potential, added to the model to create the ultra-slow feedback, modulates the total current applied in the equivalent 2D model. Indeed, bursting was shown to be a displacement in the bifurcation diagram of the 2D model with the current. The nullcline of the cell potential moves during a perturbation according to the value taken by the ultra-slow potential, which allows to modify the regime shown by the equivalent 2D model across time (stable regime or cyclic regime).

Following the incremental procedure, the analysis of the 2D and 3D models led to the analysis of the 4D model. For a constant current, this model is still able to show bursting. In contrast with the 3D model, the 4D model showed a more important modulation of the instantaneous frequency during the burst due to the additional super-slow regenerative feedback. Moreover, when the strength of the ultra-slow feedback is too low, the quiescent periods disappear and the model converges towards a limit cycle. By mapping the behavior of this model in response to an input pulse of current, we showed that the 4D model is suited to simulate each firing pattern generated by DHNs. Additionally, it was

shown that this model is able to represent other firing patterns, that are actually found by the continuous investigations of the impact of the super-slow regenerative and ultra-slow restorative feedbacks with different strengths.

In conclusion, the 4D multiple integrate-and-fire model we developed allows to reproduce the four firing patterns of DHNs. This model and its study allow to have a better understanding of the functional mechanisms of the excitability changes behind the switch in DHNs firing patterns.

Pain generating mechanisms are still unclear nowadays, they are thus many directions to explore in order to bring light on these phenomena. In the context of this work, we would like to go back to the use of conductance-based models. The objective is to show that we can generate the DHNs firing patterns. Additionally, we would like to verify that the corresponding dynamic input conductances (according to [Drion et al., 2015]) needed to generate each type of firing pattern match the types of feedbacks highlighted in this work. Another prospect is to develop a model that would represent the network of neurons involved in pain processing at the level of the spinal cord. Indeed, such a model would help to understand the mechanisms of neuronal plasticity of pain. In this manner, we could have a better understanding of the modifications made on this network after nerve injuries, giving rise to maladaptive pain processing. Based on a deep understanding of the mechanisms involved in pain processing these two prospects would provide, we would then be in a good position to design new treatment strategies, either by targetting cellular mechanisms with drugs or by designing closed-loop neurostimulation systems.

Bibliography

P. Aguiar, M. Sousa, and D. Lima. NMDA channels together with l-type calcium currents and calcium-activated nonspecific cationic currents are sufficient to generate windup in WDR neurons. *Journal of Neurophysiology*, 104(2):1155–1166, Aug. 2010. doi: 10.1152/ jn.00834.2009. URL `https://doi.org/10.1152/jn.00834.2009`.

C. Bear. *Neuroscience: Exploring the brain, (3rd ed.)*. Lippincott Williams & Wilkins, 2007.

D. Derjean, S. Bertrand, G. L. Masson, M. Landry, V. Morisset, and F. Nagy. Dynamic balance of metabotropic inputs causes dorsal horn neurons to switch functional states. *Nature Neuroscience*, 6(3):274–281, Feb. 2003. doi: 10.1038/nn1016. URL `https:// doi.org/10.1038/nn1016`.

G. Drion, A. Franci, V. Seutin, and R. Sepulchre. A novel phase portrait for neuronal excitability. *PLoS ONE*, 7(8):e41806, Aug. 2012. doi: 10.1371/journal.pone.0041806. URL `https://doi.org/10.1371/journal.pone.0041806`.

G. Drion, A. Franci, J. Dethier, and R. Sepulchre. Dynamic input conductances shape neuronal spiking. *eneuro*, 2(1):ENEURO.0031–14.2015, Jan. 2015. doi: 10.1523/eneuro. 0031-14.2015. URL `https://doi.org/10.1523/eneuro.0031-14.2015`.

Y. L. Franc and G. L. Masson. Multiple firing patterns in deep dorsal horn neurons of the spinal cord: Computational analysis of mechanisms and functional implications. *Journal of Neurophysiology*, 104(4):1978–1996, Oct. 2010. doi: 10.1152/jn.00919.2009. URL `https://doi.org/10.1152/jn.00919.2009`.

A. Franci, G. Drion, and R. Sepulchre. An organizing center in a planar model of neuronal excitability. *SIAM Journal on Applied Dynamical Systems*, 11(4):1698–1722, Jan. 2012. doi: 10.1137/120875016. URL `https://doi.org/10.1137/120875016`.

A. Franci, G. Drion, V. Seutin, and R. Sepulchre. A balance equation determines a switch in neuronal excitability. *PLoS Computational Biology*, 9(5):e1003040, May 2013. doi: 10. 1371/journal.pcbi.1003040. URL `https://doi.org/10.1371/journal.pcbi.1003040`.

Y. Guan. Spinal cord stimulation: Neurophysiological and neurochemical mechanisms of action. *Current Pain and Headache Reports*, 16(3):217–225, Mar. 2012. doi: 10.1007/ s11916-012-0260-4. URL `https://doi.org/10.1007/s11916-012-0260-4`.

A. L. Hodgkin and A. F. Huxley. A quantitative description of membrane current and its application to conduction and excitation in nerve. *The Journal of Physiology*, 117(4): 500–544, Aug. 1952. doi: 10.1113/jphysiol.1952.sp004764. URL `https://doi.org/10. 1113/jphysiol.1952.sp004764`.

E. M. Izhikevich. Hybrid spiking models. *Philosophical Transactions of the Royal Society A: Mathematical, Physical and Engineering Sciences*, 368(1930):5061–5070, Nov. 2010a. doi: 10.1098/rsta.2010.0130. URL `https://doi.org/10.1098/rsta.2010.0130`.

E. M. Izhikevich. *Dynamical systems in neuroscience: The geometry of excitability and bursting.* MIT Press, 2010b.

E. Marder. Plateau properties in pain pathways. *Nature neuroscience*, 6(3):210 – 212, 2003. ISSN 1097-6256.

T. V. Pottelbergh, G. Drion, and R. Sepulchre. Robust modulation of integrate-and-fire models. *Neural Computation*, 30(4):987–1011, Apr. 2018. doi: 10.1162/neco_a_01065. URL `https://doi.org/10.1162/neco_a_01065`.

T. V. Pottelbergh, G. Drion, and R. Sepulchre. From biophysical to integrate-and-fire modeling. *Neural Computation*, 33(3):563–589, Mar. 2021. doi: 10.1162/neco_a_01353. URL `https://doi.org/10.1162/neco_a_01353`.

C. J. Woolf. What is this thing called pain? *Journal of Clinical Investigation*, 120(11):3742–3744, Nov. 2010. doi: 10.1172/jci45178. URL `https://doi.org/10.1172/jci45178`.

T. C. Zhang, J. J. Janik, and W. M. Grill. Modeling effects of spinal cord stimulation on wide-dynamic range dorsal horn neurons: influence of stimulation frequency and GABAergic inhibition. *Journal of Neurophysiology*, 112(3):552–567, Aug. 2014. doi: 10.1152/jn.00254.2014. URL `https://doi.org/10.1152/jn.00254.2014`.

Appendices

Appendix A

Additional firing patterns
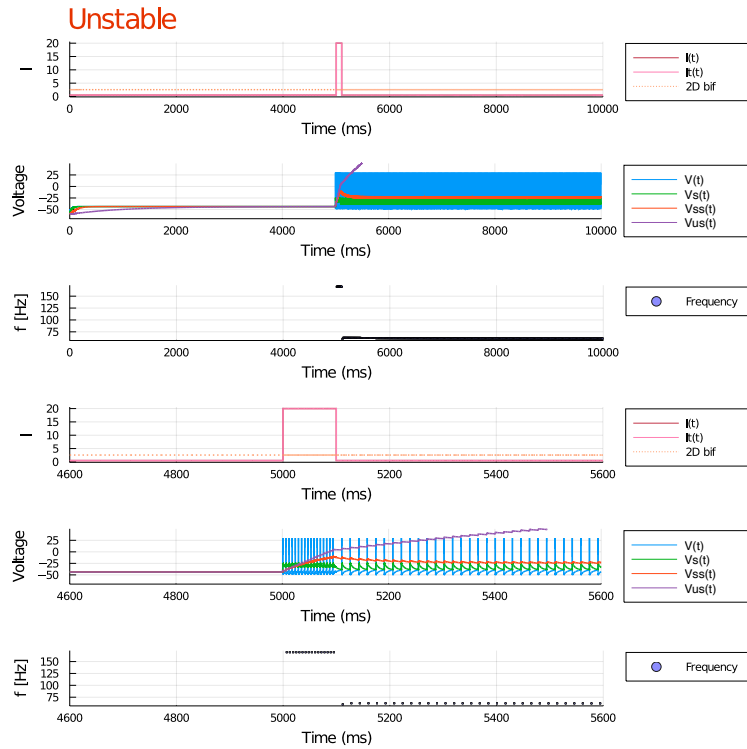
A.1 "Unstable" behavior

Figure A.1.1: Simulation of the "unstable" behavior. The three lower plots are a zoom on the three upper plots respectively around the time interval where the pulse is applied. Starting from the top, the first and fourth plots show the evolution of the applied current (red), the total current computed based V_{ss} and V_{us} (pink) and the value of the bifurcation current in the equivalent 2D model (dotted line). The second and fifth plots show the evolution of the potentials. The third and sixth plots represent the evolution of the instantaneous frequency. The currents chosen for the baseline and the maximum value for the pulse of applied current are chosen based on the methodology shown in Figure 6.4.6. The duration of the pulse is $100\,\mathrm{ms}$. The parameters used for this simulation are: $I_h{=}20$, $I_l = 0.5$, $\bar{g}_s = 0.5$, $\bar{g}_{ss} = 10^{-5}$ and $\bar{g_{us}} = 2 \cdot 10^{-6}$.
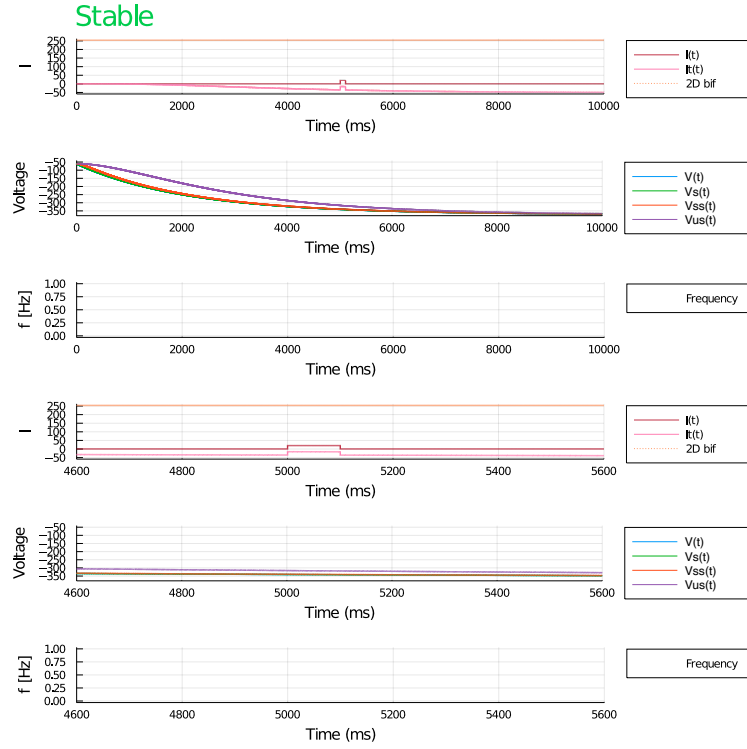
A.2   "Stable" behavior

Figure A.2.1: Simulation of the "stable" behavior. The three lower plots are a zoom on the three upper plots respectively around the time interval where the pulse is applied. Starting from the top, the first and fourth plots show the evolution of the applied current (red), the total current computed based V_{ss} and V_{us} (pink) and the value of the bifurcation current in the equivalent 2D model (dotted line). The second and fifth plots show the evolution of the potentials. The third and sixth plots represent the evolution of the instantaneous frequency. The currents chosen for the baseline and the maximum value for the pulse of applied current are chosen based on the methodology shown in Figure 6.4.6. The duration of the pulse is $100\,\mathrm{ms}$. The parameters used for this simulation are: $I_h{=}20$, $I_l = 0.5$, $\bar{g}_s = 0.5$, $\bar{g}_{ss} = 10^{-1}$ and $\bar{g}_{us} = 10^{-4}$.
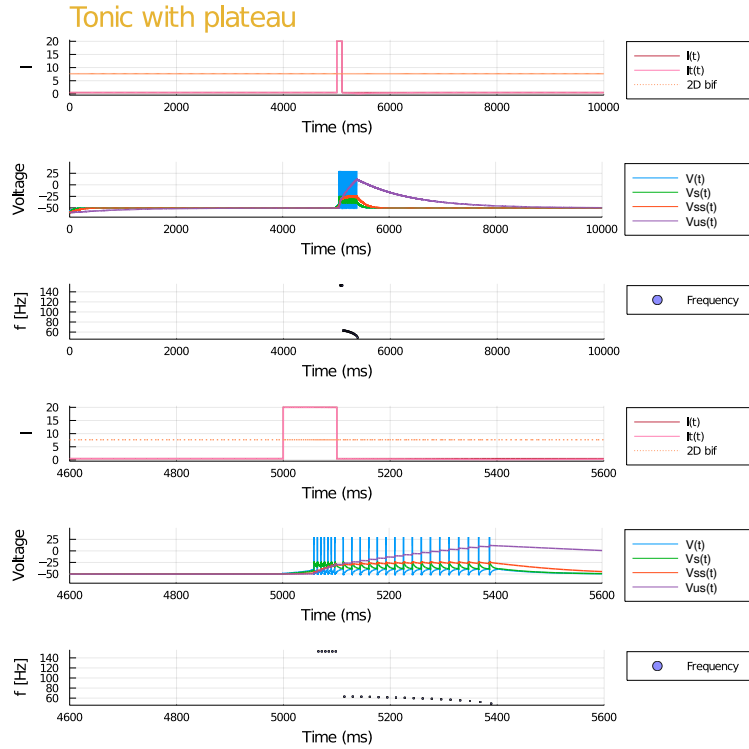
A.3 "Tonic with plateau" behavior

Figure A.3.1: Simulation of the "tonic with plateau" behavior. The three lower plots are a zoom on the three upper plots respectively around the time interval where the pulse is applied. Starting from the top, the first and fourth plots show the evolution of the applied current (red), the total current computed based V_{ss} and V_{us} (pink) and the value of the bifurcation current in the equivalent 2D model (dotted line). The second and fifth plots show the evolution of the potentials. The third and sixth plots represent the evolution of the instantaneous frequency. The currents chosen for the baseline and the maximum value for the pulse of applied current are chosen based on the methodology shown in Figure 6.4.6. The duration of the pulse is $100 \, \text{ms}$. The parameters used for this simulation are: $I_h{=}20$, $I_l = 0.5$, $\bar{g}_s = 0.5$, $\bar{g}_{ss} = 10^{-4}$ and $\bar{g_{us}} = 8 \cdot 10^{-5}$.
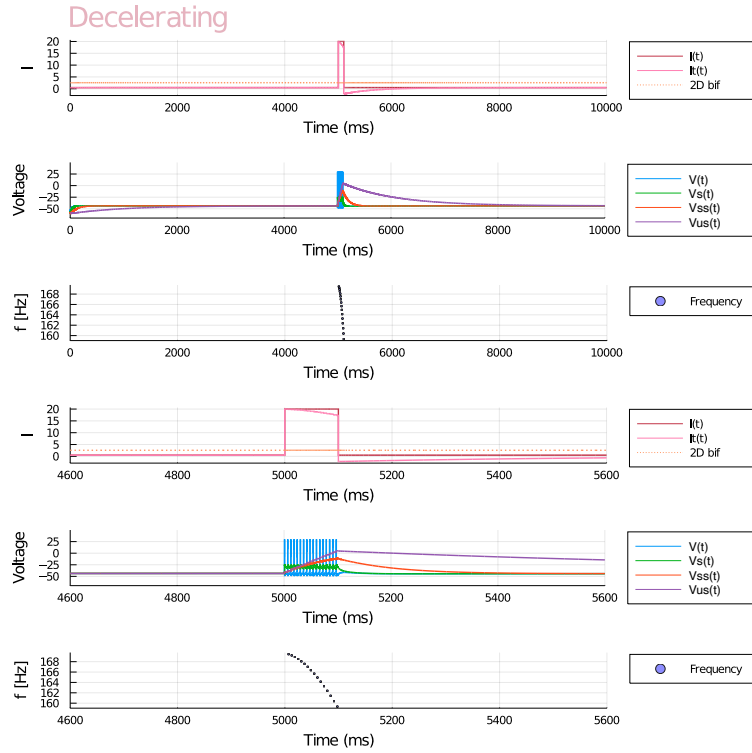
A.4 "Decelerating" behavior

Figure A.4.1: Simulation of the "decelerating" behavior. The three lower plots are a zoom on the three upper plots respectively around the time interval where the pulse is applied. Starting from the top, the first and fourth plots show the evolution of the applied current (red), the total current computed based V_{ss} and V_{us} (pink) and the value of the bifurcation current in the equivalent 2D model (dotted line). The second and fifth plots show the evolution of the potentials. The third and sixth plots represent the evolution of the instantaneous frequency. The currents chosen for the baseline and the maximum value for the pulse of applied current are chosen based on the methodology shown in Figure 6.4.6. The duration of the pulse is 100 ms. The parameters used for this simulation are: I_h=20, $I_l = 0.5$, $\bar{g}_s = 0.5$, $\bar{g}_{ss} = 10^{-6}$ and $\bar{g}_{us} = 9 \cdot 10^{-4}$.
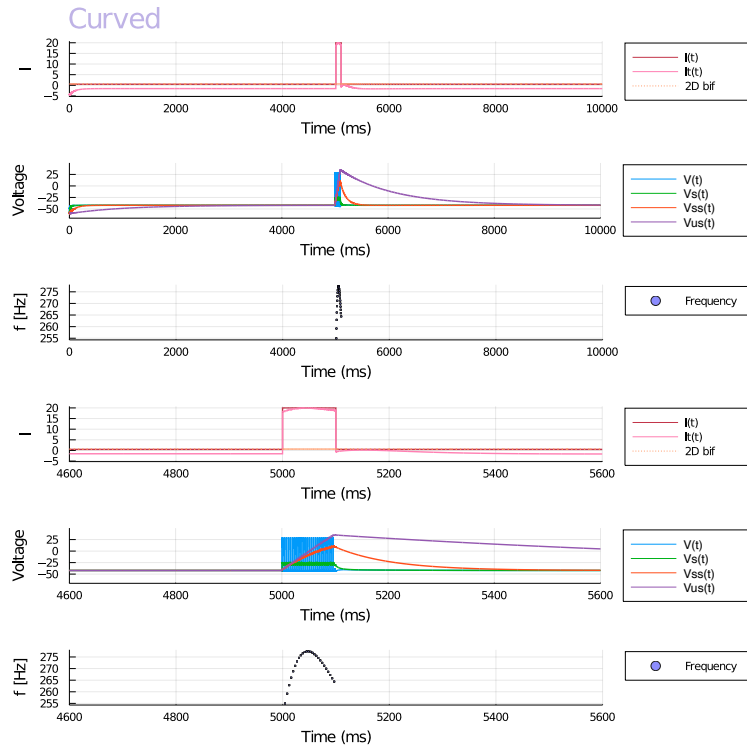
98

A.5 "Curved" behavior

Figure A.5.1: Simulation of the "curved" behavior. The three lower plots are a zoom on the three upper plots respectively around the time interval where the pulse is applied. Starting from the top, the first and fourth plots show the evolution of the applied current (red), the total current computed based V_{ss} and V_{us} (pink) and the value of the bifurcation current in the equivalent 2D model (dotted line). The second and fifth plots show the evolution of the potentials. The third and sixth plots represent the evolution of the instantaneous frequency. The currents chosen for the baseline and the maximum value for the pulse of applied current are chosen based on the methodology shown in Figure 6.4.6. The duration of the pulse is 100 ms. The parameters used for this simulation are: I_h=20, $I_l = 0.5$, $\bar{g}_s = 0.2$, $\bar{g}_{ss} = 0.002$ and $\bar{g_{us}} = 5 \cdot 10^{-5}$.